

Resistive Switching in Cu:TCNQ Thin Films

Von der Fakultät für Elektrotechnik und Informationstechnik der
Rheinisch-Westfälischen Technischen Hochschule Aachen zur
Erlangung des akademischen Grades eines Doktors der
Ingenieurwissenschaften genehmigte Dissertation

vorgelegt von

Diplom-Ingenieur Elektrotechnik

Thorsten Kever

aus Erkelenz

Berichter: Univ.-Prof. Dr.-Ing. Rainer Waser
Juniorprofessor Dr. rer. nat. Dirk Uwe Sauer

Tag der mündlichen Prüfung: 30.01.2009

Preface

This thesis was written during my Ph.D. studies at the Institut für Werkstoffe der Elektrotechnik of the Rheinisch-Westfälische Technische Hochschule (RWTH) Aachen, Germany.

I would like to express my gratitude to Prof. Waser for giving me the opportunity to do research in the exciting field of resistive switching memories and for providing an excellent working and learning environment.

I am also indebted to Prof. Sauer who kindly agreed to be the co-examiner in the jury.

Many thanks also to: Dr. Böttger for his support and stimulating discussions; Eike Linn and Ann-Christin Dippel for fruitful discussions, careful proof-reading and being great office mates; Bart Klopstra, Christian Nauenheim, Carsten Giesen and Torsten Jaspert for their dedicated work during their diploma thesis; Gisela Wasse for taking SEM pictures; Christina Schindler for fruitful discussions and the preparation of comparison samples.

Last but not least, I would like to thank all colleagues and all students at the Institut für Werkstoffe der Elektrotechnik of the Rheinisch-Westfälische Technische Hochschule (RWTH) Aachen and at the Research Center Jülich for their valuable support and many memorable moments spent together.

Contents

1	Introduction	1
1.1	Motivation	1
1.2	State of the art	2
1.3	Objectives	3
2	Non-Volatile Memory	7
2.1	Overview	7
2.1.1	Electrically Addressed Solid-State Memory Systems	8
2.2	Concepts Based on Metal-Insulator-Metal Setups	16
2.2.1	Switching Mechanisms in MIM Structures	19
2.2.2	MIM Structures Based on Organic Materials	21
2.3	The Charge Transfer Complex Cu:TCNQ	23
2.3.1	The Organic Ligand TCNQ	24
2.3.2	Formation of Cu:TCNQ	25
2.3.3	Conductivity of Cu:TCNQ and CT complexes in General	28
2.3.4	Resistive Switching in Cu:TCNQ	29
3	Device Preparation	33
3.1	Choice of the Deposition Method	33
3.1.1	Basic Principles of Vacuum Evaporation	34
3.2	Design and Construction of the Evaporation Chamber	36
3.2.1	Setup of the Vacuum Chamber	37
3.2.2	Generation of the Vacuum Pressure	37
3.2.3	Tooling of the Evaporation Chamber	42
3.2.4	Control and Regulation of the System	45
3.3	Development of the Deposition Processes	48
3.3.1	Successive Evaporation Route	50
3.3.2	The Annealing Process	53
3.3.3	Simultaneous Evaporation Route	57
3.3.4	Device Setup	62
3.4	Summary	68
4	Characterization	69
4.1	Physical Characterization	69
4.1.1	UV-Vis Spectroscopy	69
4.1.2	IR Spectroscopy	71
4.1.3	XRD Measurements	72

4.2	Electrical Characterization.....	74
4.2.1	Quasi Static Current–Voltage Measurements	74
4.2.2	Impedance Spectroscopy.....	82
4.2.3	Pulse Measurements	85
4.2.4	Temperature Dependence.....	92
4.3	Summary	94
5	Switching Mechanisms	97
5.1	Use of Different Electrode Materials	98
5.1.1	Devices with Al Top Electrodes	99
5.1.2	Devices with Pt Top Electrodes	100
5.1.3	Equivalent Circuits	102
5.1.4	TOF–SIMS Measurements	106
5.2	Control Experiments	108
5.3	Summary	109
6	Conclusions	111
6.1	Summary	111
6.2	Outlook.....	113
	Appendices	115

Used Symbols and Abbreviations

δ	Degree of Charge Transfer
C	Electrical Capacitance
E	Electrical Field
P	Polarization
Q	Electrical Charge
R	Electrical Resistance
V	Voltage
BNC	Bayonette Neil Concelman
CMOS	Complementary Metal Oxide Semiconductor
CSD	Chemical Solution Deposition
CT	Charge Transfer
DRAM	Dynamic Random Access Memory
EPROM	Erasable Programmable Read-Only Memory
FeFET	Ferroelectric Field Effect Transistor
FeRAM	Ferroelectric Random Access Memory
FET	Field Effect Transistor
FTIR	Fourier Transform InfraRed
HV	High Vacuum
ICT	Information and Communication Technology
IMT	Insulator-Metal Transition
IR	InfraRed
ITRS	The International Technology Roadmap for Semiconductors
MIM	Metal- Insulator- Metal
MIM	Metal-Insulator-Metal
MOS	Metal Oxide Semiconductor
MRAM	Magnetoresistive Random Access Memory
MV	Manipulated Variable
NAND	Not AND
NFGM	Nano-Floating Gate Memory
NMOS	n-type MOS
NOR	Not OR
NP	NanoParticles
NVM	Non-Volatile Memory
NVRAM	Non Volatile Random Access Memory
PC	Personal Computer
PCM	Phase Change Memory
PID	Proportional Integral Derivative
PMC	Programmable Metallization Cell

PV	P rocess V ariable
PVD	P hysical V apor D eposition
QCM	Q uartz C rystal M icrobalance
RAM	R andom A ccess M emory
RIE	R eactive I on E tching
RRAM	R esistive R andom A ccess M emory
SEM	S canning E lectron M icroscope
SIMS	S econdary I on M ass S pectrometry
SOI	S ilicon O n I nsulator
SONOS	S emiconductor O xide N itride O xide S emiconductor
SRAM	S tatic R andom A ccess M emory
STM	S canning T unneling M icroscope
TCNQ	T etracyanoquinodimethane
TOF	T ime O f F light
UHV	U ltra H igh V acuum
UV-Vis	U ltra V iolet- V isible
VARIOT	V ariable O xide T hickness floating gate memory
XRD	X - R ay D iffraction
Z-RAM	Z ero C apacitance R andom A ccess M emory

1 Introduction

1.1 Motivation

The demand for information storage has increased rapidly in recent years. New applications and concepts in the information and communication technology (ICT), like high-definition video, on-demand TV, multimedia entertainment, and data/information services are entering the consumer market every year. Most, if not all of these new applications, require the handling and storage of large amounts of data. Therefore, the market will expect the semiconductor industry to maintain the exponential growths predicted by Moore's law [1] for the next several years by successfully continuing the scaling of CMOS beyond the 22 nm generation [2].

The focus of ICT products has shifted toward portable and hand held devices in recent years. Small portable systems enable communication, web browsing, image and video capturing, and data/information services as well as multimedia entertainment from any place and at any time. The expected further evolution of these application and services indicate an ever increasing need for larger capacity of data storage memories up to even the Terabyte range. The strong gain in importance of portable devices emphasis some key parameters of the different technologies stronger than others. Obviously size matters for hand held devices as well as robustness against mechanical stress. Therefore, mass storage technologies based on solid-state memory systems are strongly favored, even when taking higher costs in terms of pure cost/bit compared to hard disk mass storage devices into account [3].

Considering the portable character of the applications, energy efficiency (dictated by limited battery capacity) is another key parameter while assessing different technologies. Non-volatile memory (NVM) meets the requirement for low (zero) power storage. Only the growing demand of portable consumer products like mobile phones, digital camera's, and MP3 players in recent years, rendered the tremendous success story of Flash memories on a grand scale possible. Flash technology is based on a MOSFET transistor with a floating gate where charges can be stored in order to modulate the threshold voltage [4]. The NVRAM market today is dominated by NOR and NAND

Contents

1.1	Motivation.....	1
1.2	State of the art.....	2
1.3	Objectives	3

Flash concepts. An important technological factor in the continuing growth of the solid-state Flash share of the memory market is its strong scaling ability, that has enabled the continuous decrease of cost per bit. Therefore, larger and larger memories become affordable at very reasonable costs. However, it is expected that existing physical limitations reduce the margins for cell size reduction of floating-gate Flash concepts, unless substantial progress is made in critical areas. Therefore, the Flash memory concept will face severe scaling problems beyond the 45 nm and 32 nm technology nodes [5].

Considering these limitations, there is a growing interest in alternative non-volatile memory technology concepts for massive data storage which have the potential to eventually replace NOR and later NAND Flash in 32 nm technologies and below. Emerging NVRAM concepts can try to enter the actual Flash centric memory market by exploiting the performance weaknesses of Flash like slow write/erase times, high operating voltages, and low cycling endurance. However, like past experiences demonstrated the most important factor is cost efficiency. This means, better scaling capabilities than Flash are imperative in order to eventually become the leading NVRAM technology. A lot of money, know-how and scientific effort has been and will be invested in this search for alternative non-volatile memory concepts, which are expected to become a key part of the technology and value chain of the integrated hand held devices of the future.

1.2 State of the art

As mentioned in section 1.1, the Flash technology is fully compatible to the CMOS technology due to the MOS-like architecture of the combined select/storage element and the utilized materials. This compatibility, in connection with the small cell size, has made Flash the cheapest solution for solid state stand alone and embedded memory applications. However, scaling problems are expected to severely slow down the progress in Flash technology in the near future [5].

A possible starting point to circumvent scaling issues in standard CMOS and Flash technology is a different memory architecture where the selecting element (today a transistor in the future possibly a diode within a passive array [6]) is decoupled from the storage element. In this case, the processing of the memory cell can be moved to the back-end part of the integration line, thereby increasing the embeddability [7]. In addition, no further restrictions will be introduced into the CMOS processing due to the memory material selection. Better performance values will also help the chances of a new technology to successfully enter the market. As a matter of fact, a NVRAM technology with considerable better performance in the areas where Flash shows weaknesses (power and voltage levels, speed of read/erase operations, and endurance) would increase the liberties of system designers considerable.

Currently, a lot of different NVRAM technologies/materials are under investigation by companies, research facilities, and universities. Among them are very different concepts basing on, for example, ferroelectric (FeRAM [8], FeFET [9]) or magnetic (MRAM [10]) effects. Furthermore, some new concepts are under investigation which are basing on the proven Flash technology (e.g. nano-floating gate memory (NFGM) [11]). A more detailed overview about the different NVRAM technologies is

given in section 2.1.

One large group of these emerging technologies can be summarized under the label resistive switching memories. It includes the memory concepts, which are based on a resistor as a memory element. This element can be electrically programmed in a high and a low (or ideally in more than two) resistive state(s). Even within this group, there are several different concepts and numerous potential materials. Some of these concepts can be set to the different states using an unipolar voltage and enable therefore theoretically an use in a passive diode array, while others need bipolar voltages to switch the resistances. Well known technologies belonging to this group are, for example, phase change memories (PCM) [12] or programmable metallization cells (PMC) [13]. There is a wide range of resistive memory materials proposed in these concepts. The materials span from organics (rotaxanes, polyphenyleneethylenes, Cu:TCNQ etc.) to inorganics (chalcogenide metal alloys, perovskite-type oxides, manganites, binary transition metal oxides etc.). In combination with these materials, a wide range of electrode materials (various metals as well as electronically conducting oxides and nitrides) are proposed and demonstrated. A more detailed introduction and comparison of those concepts and materials is shown in section 2. Despite the increased research efforts, there is still a lot of speculation and discussion in the scientific community about the exact physical switching mechanisms in many of those concepts. One important point, independent of concept and material, is certainly the more or less pronounced influence of the electrode materials and the subsequently formed interfaces.

One of the many proposed materials is the metal–organic charge transfer complex Cu:TCNQ. Thin films consisting of copper as metal donor and tetracyanoquinodimethane (TCNQ) as organic acceptor exhibit a bistable resistive switching phenomena. Potember et al. first reported electrical field induced switching effects in Cu:TCNQ thin films sandwiched between copper and aluminum electrodes [14]. Cu:TCNQ is especially interesting due to the reported low switching currents, the compatibility with standard electrode materials such as Cu and Al, and the possibility of a selective growth of thin films on Cu (explained in more detail in chapter 3). While different physical mechanisms have been proposed (details shown in section 2.3) to be responsible for this resistive switching effect, no consensus has been found yet.

1.3 Objectives

The main aim of this thesis is to improve the physical understanding of the resistive switching effect in Cu:TCNQ thin films. An established and widely accepted theory to the switching mechanisms in Cu:TCNQ is still missing, despite published work of several groups on this topic. Besides a detailed introduction to non-volatile technologies in general and the state of the art concerning Cu:TCNQ in special (chapter 2), this task is carried out as displayed in the flow-chart shown in Fig. 1.1. Therefore, the activities carried out in the scope of this thesis can be summarized by the following items:

- Design and construction of a high vacuum chamber with the following capabilities (details are explained in section 3.2):
 - Two independent evaporation sources, one for Cu and other electrode metals and one for the organic material (TCNQ), which can be used simultaneously

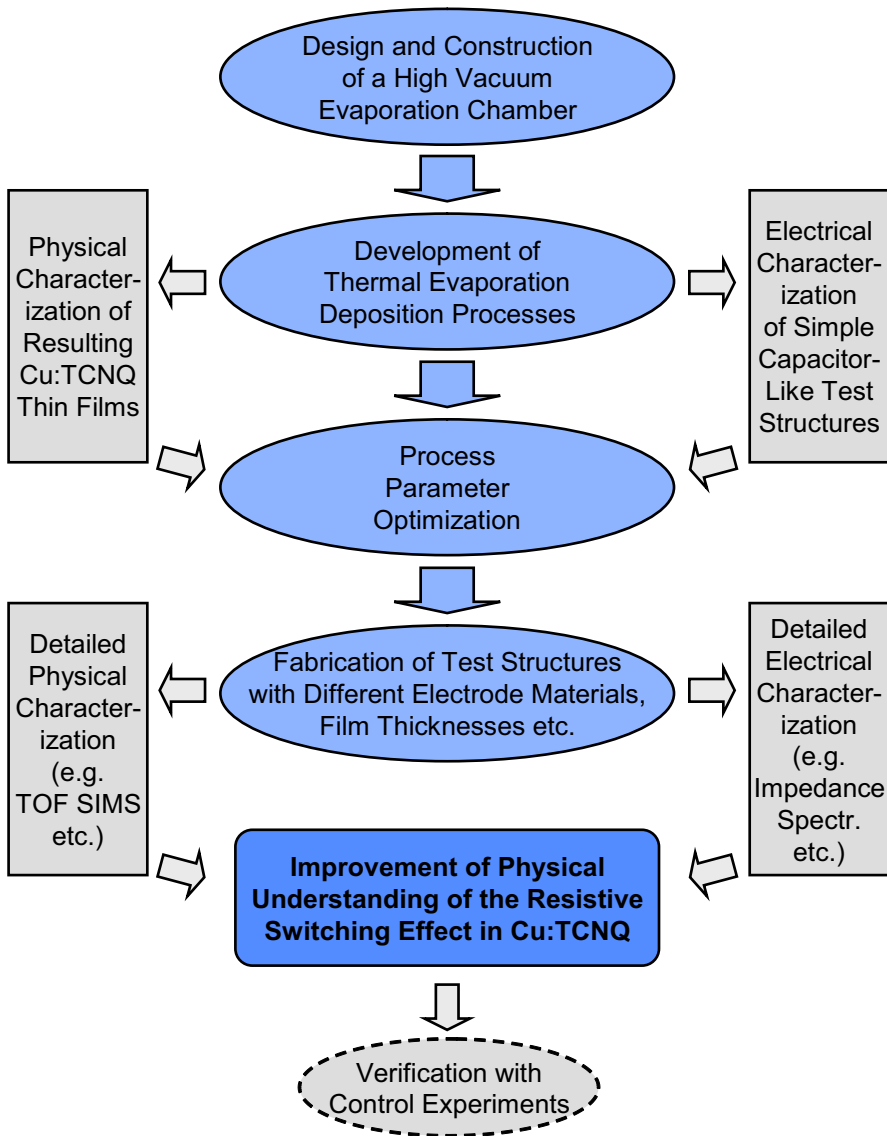


Figure 1.1: Flow-chart displaying the thesis overview. Starting from the design of the evaporation chamber, over process development and optimization, to fabrication of different test structures. Physical and electrical characterizations provide feedback and information for a better understanding of the switching effects.

- Control of the evaporation rates
 - Heating/Cooling of the substrate holder possible
- Development of two different thermal evaporation processes for the deposition of Cu:TCNQ thin films (details are explained in section 3.3):
 - Successive evaporation route (Deposition of TCNQ on top of a Cu layer with subsequent thermally activated redox reaction \Rightarrow formation of Cu:TCNQ)
 - Co-evaporation route (Cu and TCNQ are evaporated together at a ratio of $\approx 1 : 1 \Rightarrow$ direct formation of Cu:TCNQ)
- Physical and electrical characterizations of the resulting thin films to assist the process development and parameter optimization (details are explained in chapter 4)
- Fabrication of different test structures after the development of optimized deposition processes (details are explained in chapter 5):
 - Use of different combinations of various electrode metals
- Use of sophisticated characterization methods (details are explained in chapter 5):
 - Detailed physical characterization (e.g. TOF SIMS, etc.)
 - Detailed electrical characterization (e.g. impedance spectroscopy, etc.)
- Interpretation of the results in order to improve the physical understanding of the resistive switching effect in Cu:TCNQ thin films (details are explained in chapter 5)
- Verification with control experiments (details are explained in section 5.2)

2 Non-Volatile Memory

2.1 Overview

Information storages can be divided into two categories, volatile and non-volatile memories. Volatile memories include all concepts, which require a continuous power supply in order to maintain the stored informations. The two main technologies in this area are DRAM, which is based on charge storage in a capacitor [15], and SRAM, which is based on flip-flop latches [16]. DRAM is widely used as a primary storage, however its volatile nature means that when shutting the computer down or worse in case of a computer crash any data in the RAM is lost. Recently, a new concept called Zero capacitor RAM (Z-RAM) has been demonstrated as a simple 1T-DRAM cell [17]. It is based on the body charging of SOI devices to store the information and integrates a single MOSFET.

Non-volatile memory is a collective term for all kind of information storage which can retain the stored data without power supply. This kind of memory is widely used as a secondary, or long-term persistent storage. Up to now, no form of non-volatile technologies has replaced the volatile DRAM as primary storage in computers due to performance or cost limitations.

Using the nomenclature of the *International Technology Roadmap for Semiconductors* (ITRS), the different memory technologies can be classified into categories based on their maturity and their position on the market.

Contents

2.1	Overview	7
2.1.1	Electrically Addressed Solid-State Memory Systems.....	8
2.2	Concepts Based on Metal-Insulator-Metal Setups	16
2.2.1	Switching Mechanisms in MIM Structures.....	19
2.2.2	MIM Structures Based on Organic Materials.....	21
2.3	The Charge Transfer Complex Cu:TCNQ.....	23
2.3.1	The Organic Ligand TCNQ	24
2.3.2	Formation of Cu:TCNQ	25
2.3.3	Conductivity of Cu:TCNQ and CT complexes in General .	28
2.3.4	Resistive Switching in Cu:TCNQ.....	29

The so-called baseline technologies category describes technologies which are well established on the market and produce some high volume products. This group includes DRAM, SRAM, hard disk drives, optical disks, magnet tapes, floppy disks, and NAND and NOR Flash.

The so-called prototypical technologies category describes technologies which either have demonstrated prototype devices, or already have some low volume, niche products on the market. This group includes FeRAM [8], MRAM [10], SONOS [18] and PCM [12].

The last group, called emerging research memory devices category, consists of all other technologies which have not yet reached the maturity and production status to belong to one of the other groups. This group includes among others nano-floating gate memory (NFGM) [11], engineered tunnel barrier memory (VARIOT) [19], FeFET [9], insulator resistance change memory (MIM) [20], PMC [13], polymer memory [21], and molecular memory [22].

The mentioned different memory technologies are shown in overview in Fig. 2.1. Their affiliation to the above-described categories is shown in the style of the print. **Bold** for baseline technologies, normal for prototypical technologies, and *italic* for emerging research memory devices. In addition, they are arranged due to their principal design and storage mechanism.

As shown in Fig. 2.1, the non-volatile branch itself can be divided into two main categories, electrically addressed solid-state memory systems and mechanically addressed systems. Examples for technologies belonging to the latter category are hard disks, floppy disk drives, magnetic tape, optical disks, holographic memory, etc., and early computer storage methods such as paper tape and punch cards. Mechanically addressed systems have the price advantage regarding cost per bit, but are also slower compared to electrically addressed solid state systems.

2.1.1 Electrically Addressed Solid-State Memory Systems

The electrically addressed solid-state memory systems themselves can be divided into subcategories. Some main subcategories are shown in Fig. 2.1 with the respective most important examples. The projected future properties of some of the different competing technologies extracted from the ITRS roadmap 2007 are summarized in Table 2.1 and compared with the projected DRAM features. These properties are described in more detail for the different concepts in the following subsections.

Magnetic Concepts

In magnetic concepts the information is stored in magnetic cells. The most important example is the MRAM technology, in which the storage elements are formed from two ferromagnetic layers separated by a thin insulating film [10]. In addition to the storage cell, a transistor is necessary making this concept a 1T1R technology. One of the layers of the storage cell is a permanent magnet with a defined polarity. The field of the other ferromagnet is changed to match that of an external field. Due to the magnetic tunnel effect, the electrical resistance of the cell changes depending on the orientation of the fields in the two layers. Therefore, the readout is carried out by a simple measurement

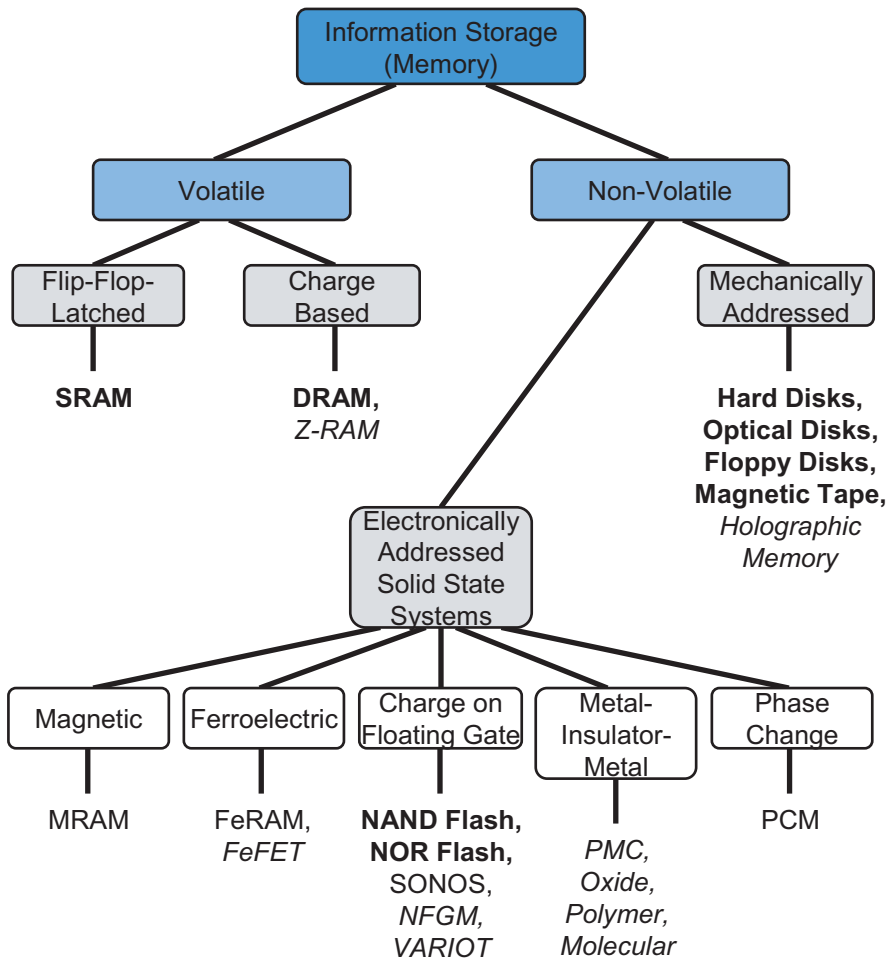


Figure 2.1: Overview over the different memory technologies. Baseline technologies are printed in bold, Prototypical technologies are printed in normal, and emerging research technologies are printed in italic.

Concept	Baseline Technologies		Prototypical Technologies		
	DRAM	NAND Flash	FeRAM	MRAM	PCM
Storage Mechanism	charge on capacitor	charge on floating gate	remanent polarization on FeCap	magnetization of ferromagnetic contacts	reversible changing amorphous-crystalline
Cell Elements	1T1C	1T	1T1C	1T1R	1T1R
Feature Size (nm)	12	18	65	22	18
Cell Area	6F ²	5F ²	12F ²	16F ²	4.7F ²
Read Time	< 10 ns	10 ns	< 20 ns	< 0.5 ns	< 60 ns
W/E Time	< 10 ns	100 ns	1 ns	< 0.5 ns	< 50 ns
Retention Time	64 ms	> 10 y	> 10 y	> 10 y	> 10 y
Write Cycles	> 3 E ¹⁶	> 1 E ⁵	> 1 E ¹⁶	> 1 E ¹⁶	1 E ¹⁵
Operating Voltage	1.5 V	15 V	< 1 V	< 1.8 V	< 3 V
Write Energy (J/bit)	2 E ⁻¹⁵	> 1 E ⁻¹⁵	5 E ⁻¹⁵	5 E ⁻¹⁵	< 1 E ⁻¹³

Table 2.1: *Projected properties for the year 2022 for some competing memory device technologies (Data extracted from ITRS roadmap 2007) [23].*

of the resulting current while applying a defined voltage. If the two ferromagnetic layers have the same polarity, the cell is in the low resistance state, otherwise with opposite polarities, it is in the high resistance state.

The principal writing scheme is similar to that of early magnetic core memories, which were used commonly in the 1960s. The information is written to the cells via an induced magnetic field created at the junction of the lines. However, this simple approach requires a quite high write current to generate the field. Therefore, some different solution have been proposed and demonstrated like the use of a modified multi-layer cell with thin coupling layers [24] or the spin-torque-transfer (STT), which uses spin-aligned (‘polarized’) electrons to directly torque the domains [25].

Using data from the ITRS roadmap, advantages and disadvantages of MRAM compared to Flash are:

- + Faster write/erase operation
- + Prospective faster readout

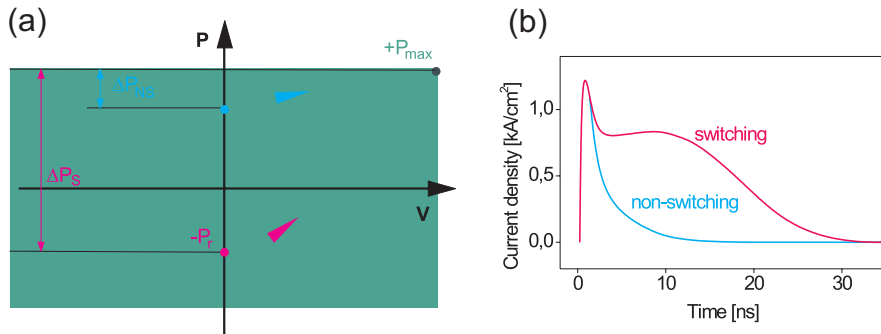


Figure 2.2: Principle behavior of a ferroelectric capacitor [3]. (a) Non-switching and switching of the polarization of a ferroelectric capacitor. (b) Current response of non-switching and switching case of the ferroelectric polarization.

- + Much better cycle endurance
- + Lower operating voltages
- Higher write/erase currents
- Larger cell area

In conclusion, MRAM is currently a good example for a mature technology with an overall very good performance, which is still not widely adopted in the market due to a large cell area and scaling issues. Therefore, this technology is not competitive regarding cost/bit at the moment.

Ferroelectric Concepts

Ferroelectric concepts for non-volatile memory can be divided into two major technologies. The more advanced and mature is the FeRAM concept. The cell configuration is in principal similar to DRAM whereas the dielectric capacitor is replaced by a ferroelectric one. The information is therefore stored in the ferroelectric film [8]. The ferroelectric layer has the characteristic of a remanent polarization, which can be reversed by an applied electric field. This behavior is observable in the hysteretic loop of the polarization P plot over the electrical field E , respectively the applied voltage V as shown in Fig. 2.2 (a). The FeRAM concept uses this $P(E)$ characteristic in order to store data non-volatile. The two different state are the positive ($+P_r$) and negative ($-P_r$) remanent polarization.

In order to write/erase and read the memory cell, voltage pulses are applied. No switching occurs, if the applied voltage is in the direction as the remanent polarization. In this case, the change of polarization ΔP_{NS} is due to the dielectric response of the ferroelectric material. Switching occurs, if the applied voltage is in the opposite direction of the applied field. In this case, the polarization reverses giving rise to an increased switching polarization change ΔP_S as shown in Fig. 2.2 (a).

Therefore, the different states of the remanent polarization cause different current

responses to applied voltage pulses. The difference between the switching and the non-switching case in the transient current behavior is shown in Fig. 2.2 (b). Due to this, the two memory states can be determined by integration of the current responses. The switched charge ΔQ_S is distinctively larger than the non-switched one ΔQ_{NS} .

Using data from the ITRS roadmap advantages and disadvantages of FeRAM compared to Flash are:

- + Faster write/erase operation
- + Much better cycle endurance
- + Lower operating voltages
- Slower read time
- Larger cell area

In conclusion, FeRAM is currently also like MRAM a good example for a mature technology with an overall very good performance which is still not widely adopted in the market due to a large cell area and scaling issues. Therefore, this technology is not competitive regarding cost/bit and limited to niche markets (e.g. smartcards) at the moment.

A different and more immature concept based on ferroelectric materials is the FeFET. In contrast to FeRAM, no capacitor cell is needed. Instead, the ferroelectric material is used as the gate dielectric in a field effect transistor as shown in Fig. 2.3. This means, that the ferroelectric layer is integrated into the transistor and therefore the FeFET is a single element device.

The principle functionality of a FeFET can be explained on the basis of a single operation cycle of a p-type FeFET shown in Fig. 2.3. For an applied positive voltage pulse the polarization P in the ferroelectric layer is switched towards the direction of the Si-channel (Fig. 2.3 (a)). Therefore, a negative charge is taking effect on the interface to the p-type semiconductor channel due to the ferroelectric polarization. An inversion and an accumulation of electrons (in the semiconductor) near the interface is occurring as the result. Therefore, the source-drain channel is in the on-state and will remain stable (as long as the remanent polarization P_r stays sufficiently large), even if the applied voltage is removed.

By application of a negative voltage pulse, the polarization is switched to the opposite direction. Therefore, electrons are depleted within the semiconductor channel at the interface and the FeFET is in the off-state. This situation is schematically shown in Fig. 2.3 (b).

A non-destructive readout is possible due to the fact, that only the source-drain channel resistance has to be determined by a peripheral sense amplifier. Thereby, the status of the ferroelectric polarization is undisturbed. In contrast, a polarization reversal and reprogramming is necessary in the readout process of a 1T1C FeRAM cell.

The interesting properties of ferroelectric field-effect transistors (FeFETs) are the non-volatile data storage with a non-destructive readout, and the compact cell design (1T-cell). However, up to now some problems remain (complex fabrication issues, short retention of the ferroelectric polarization, and interface charge traps), which prevent the production of commercial products [3].

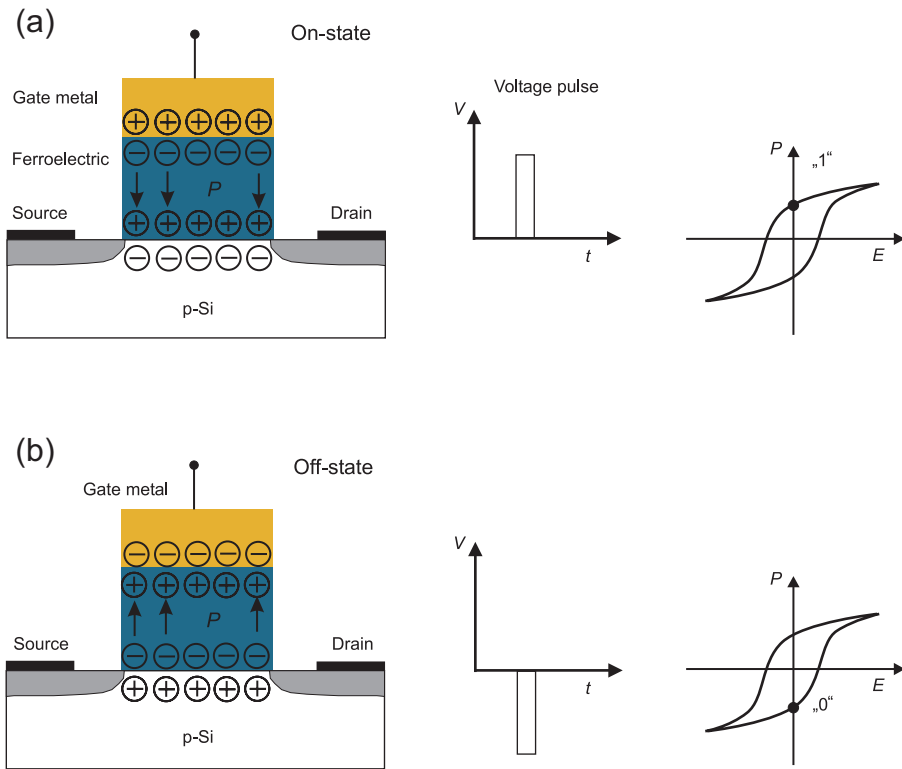


Figure 2.3: Schematic mode of operation of a FeFET [3]. Charge diagram for the on– (a) and off–state (b) of a FeFET after application of a positive (a) and a negative (b) voltage pulse. The right figures show the corresponding polarization states.

Charge on Floating Gate

Flash memory based on the floating gate concept is currently market leader in the non-volatile, solid-state memory branch as mentioned in section 1.1. Flash technology is based on a MOSFET transistor with an additional floating gate [4]. The data is stored as charge on the floating gate and modulates the threshold voltage of the transistor. In order to prevent the stored charge from draining off, the floating gate is electrically isolated. A change in the amount of charge on the floating gate is therefore ideally only possible due to quantum tunneling. In traditional single-level cell devices, each cell stores only one bit of information. Newer flash memory concepts, known as multi-level cell devices, can store more than one bit per cell. This is realized by the application of multiple levels of electrical charge to the floating gates of the cells.

Two different kinds of Flash architectures are common today, NAND and NOR. They differ in the internal design and wiring of the individual cells in the memory matrix. Depending on this, the memory density and the access time varies. NAND-Flash is based on a series connection of larger memory cell blocks. This implies, that write/erase and read operations are not possible on single cells but only sequential on

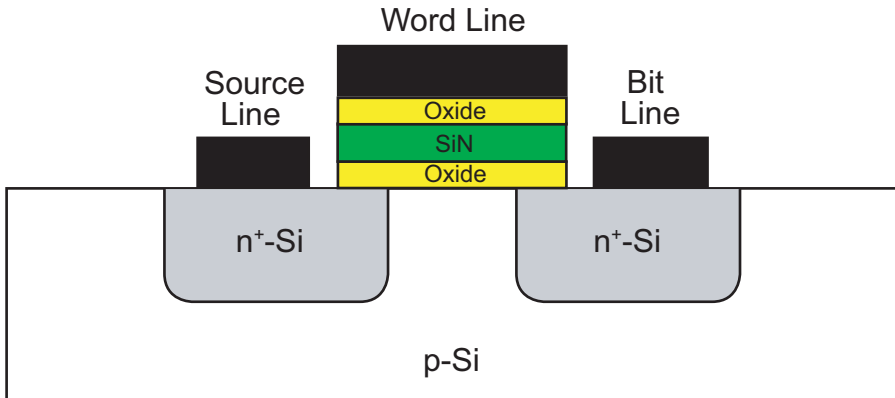


Figure 2.4: Schematic of a SONOS memory cell. The cell is based on a *n*-type MOSFET in whose oxide a silicon nitride (SiN) layer is buried, which acts as the floating gate.

whole blocks. In addition, the access times are slower than in the NOR architecture due to longer *RC* times. However, higher memory densities can be achieved by this architecture. NAND-Flash therefore aims at the mass storage market where higher densities are more important than fast access times.

NOR-Flash on the other hand is based on a parallel connection of single memory cells. This implies random access to all cells and faster access times than NAND-Flash. However, only lower memory densities compared to NAND can be achieved in this architecture. In addition, newer designs implement a block erase scheme instead of a single cell erase. NOR-Flash therefore aims at markets where access time is more important than density. It has replaced traditional EPROM devices and is dominating the programmable memory for micro controller market.

The concept of Flash memories has still some limitations despite the recent enormous success:

- Only block access in NAND-Flash and block erase in both, NOR and NAND architecture
- Low cycle endurance due to oxide degeneration
- High operating voltages
- Slow write/erase operations
- Access time (NAND)
- Density (NOR)

Due to this limitations and expected scaling problems in future generations [5], a number of potential Flash replacements are currently under development. One of the most mature of these concepts is the 'Semiconductor Oxide Nitride Oxide Semiconductor' (SONOS) technology. It potentially offers lower power usage and a somewhat longer lifetime than Flash [18]. The SONOS memory cells consist of a standard NMOS transistor with a more complex, layered oxide structure under the gate as shown in Fig. 2.4. The layering consists of an oxide thin film, which is approximately 2 nm thin, a silicon nitride layer (about 5 nm thin), and a second oxide

layer with a thickness between 5 and 10 nm. By application of a positive voltage to the gate, electrons from the source–drain channel tunnel through the thin oxide layer and get trapped in the silicon nitride. Like in standard Flash cells, this trapped charge influences the threshold voltage of the transistor. In order to erase the cell, the trapped electrons are removed by application of a negative voltage to the gate. In addition to the SONOS technology, other floating gate concepts (e.g. NFGM (charge trapping in nanodots) [11] and VARIOT (variable oxide thickness) [19]) are under development.

In conclusion, the floating gate concept with Flash memory is the leading solid state non-volatile technology today. It can be expected to remain in this position for some time in the future by further developments and adaptations in future CMOS technology generations. Other designs will be hard pressed to capture main portions of the Flash dominated market.

Phase Change

Phase-change memory (PCM, also known as PRAM, PCRAM, Ovonic Unified Memory and Chalcogenide RAM (C-RAM)) is another type of a solid state non-volatile memory [26]. PCM exploits a material behavior of some alloys based on group VI elements, which are called chalcogenides. These glassy materials are stable in both the crystalline and the amorphous state at room temperature. The change between the two states can be controlled by the application of heat. This behavior of chalcogenide materials is already widely used in optical re-writable CD/DVD disks [27]. In the optical disk application, a laser beam with different intensities is used to heat a small volume in order to switch the material between its crystalline and amorphous state. The memory state is determined by the reflectivity of the memory layer.

The same behavior can be used in a silicon based device as shown schematically in Fig. 2.5. In this case, electric currents of different magnitudes are passed from a heater element through the chalcogenide material. The subsequent local joule heating changes the programmable volume around the contact region. High current and fast quenching freezes the material to an amorphous state (Fig. 2.5 (b)), which is the high resistance state. The application of a medium current for a longer pulse duration leads to a re-crystallization of the region (crystalline state) (Fig. 2.5 (a)), which has a lower resistance [26]. The state of the memory cell is read out at low currents, which produce no significant joule heating.

Using data from the ITRS roadmap advantages and disadvantages of PCM compared to Flash are:

- + Faster write/erase operation
- + Much better cycle endurance
- + Lower operating voltages
- Higher write/erase currents and energies

In conclusion, PCM is another promising technology to potentially replace Flash because of the above-mentioned advantages. However, one main issue for phase change based devices is its susceptibility to a fundamental trade off of unintended vs. intended phase-change. This is mainly due to the fact that phase-change is a thermally driven process. This means, that an optimization of the material properties towards faster switching and lower energy consumption also influences data retention.

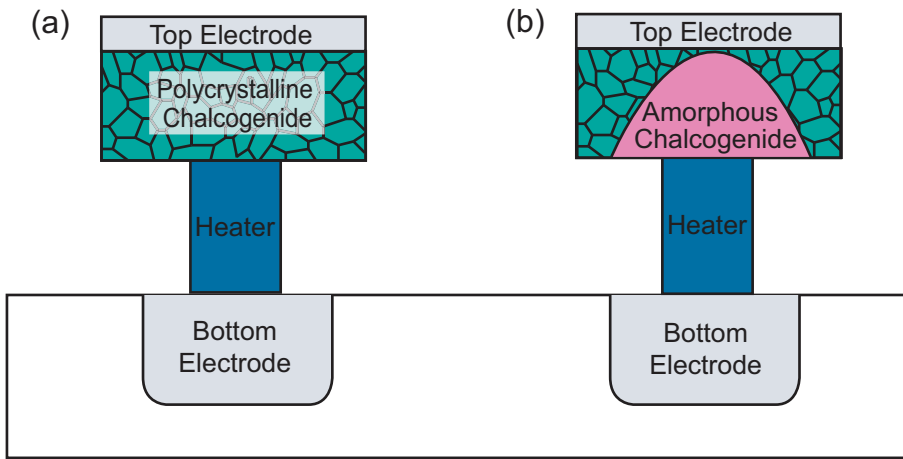


Figure 2.5: *Schematic of a phase change memory cell. Polycrystalline (low resistance) state of the chalcogenide material (a) and local amorphous area above the heater element (high resistance state) after high current pulse (b)*

2.2 Concepts Based on Metal–Insulator–Metal Setups

Another subcategory of the non-volatile, electronically addressed solid state systems is based on a metal–insulator–metal memory (MIM) cell. Many of these MIM structures exhibit an electrically induced resistive switching behavior. Devices based on a MIM cell are usually called resistance switching RAM, or RRAM. The letter ‘M’ in the abbreviation MIM is not restricted to metals, but refers to any reasonably good electron conductor, and is often different for the two sides. The ‘insulator’ in these structures is often an ion-conducting material. MIM memory cells, like the other mentioned non-volatile concepts in section 2.1, are interesting due to their potential performance advantages over Flash and DRAM, and they might be highly scalable.

Due to the wide range of different materials (binary and multinary oxides, higher chalcogenides, organic compounds and molecules, etc.) numerous devices have been presented and different resistive switching mechanisms proposed. First reports on this effect were published as early as 1962 by Hickmott on oxide materials [28]. This period of high research activity continued until the mid-1980s and during its course many MIM structures were presented [29]. Due to the increasing interest in resistive switching devices for memory applications, a new period of intense research activities started in the late 1990s and still continues today [30–32].

The ITRS roadmap divides the MIM structures class into several subcategories. A choice of the most important ones is given in Table 2.2 with the best projected and the already demonstrated properties. The potential of these technologies can be seen by a comparison of the parameters with the ones of the baseline technologies shown in Table 2.1.

Prior to a more detailed look on the different devices and proposed mechanisms, it is important to introduce two different basic switching schemes in MIM structures.

Concept	Emerging Research Memory Devices				
	Fuse/Antifuse Memory	Ionic Memory	Electronic Effects Memory	Macromolecular Memory	Molecular Memories
Storage Mechanism	multiple mechanisms	ion transport and redox reaction	multiple mechanisms	multiple mechanisms	not known
Cell Elements	1T1R or 1D1R	1T1R or 1D1R	1T1R or 1D1R	1T1R or 1D1R	1T1R or 1D1R
Feature Size (nm)	5-10 (180)	5-10 (90)	5-10 (1000)	5-10 (250)	5 (30)
Cell Area	$5F^2$	$5F^2$ ($8F^2$)	$5F^2$	$5F^2$	$5F^2$
Read Time	< 10 ns	< 10 ns (< 50 ns)	< 10 ns	< 10 ns (10 ns)	< 10 ns
W/E Time	< 10 ns (10 ns/5 μ s)	< 20 ns (< 50 ns)	< 20 ns (100 ns)	< 10 ns (10 ns)	< 40 ns (0.2 s)
Retention Time	> 10 y (> 8 months)	> 10 y (> 10 y)	> 10 y (1 y)	not known (6 months)	not known (6 months)
Write Cycles	> 3×10^{16} (> 1×10^6)	> 3×10^{16} (> 1×10^6)	> 3×10^{16} (> 1×10^3)	> 3×10^{16} (> 1×10^6)	> 3×10^{16} (> 2×10^3)
Operating Voltage	0.5/1 V (0.5/1 V)	< 0.5 V (0.6 V)	< 3 V (3-5 V)	< 1 V (2 V)	< 0.3 V (1.5 V)
Write Energy (J/bit)	not known (1×10^{-12})	1×10^{-15} (5×10^{-14})	< 1×10^{-10} (1×10^{-9})	not known (1×10^{-13})	< 2×10^{-19}

Table 2.2: *Best Projected properties for some emerging memory device technologies. Demonstrated values, if available, in parentheses. (Data extracted from ITRS roadmap 2007) [23].*

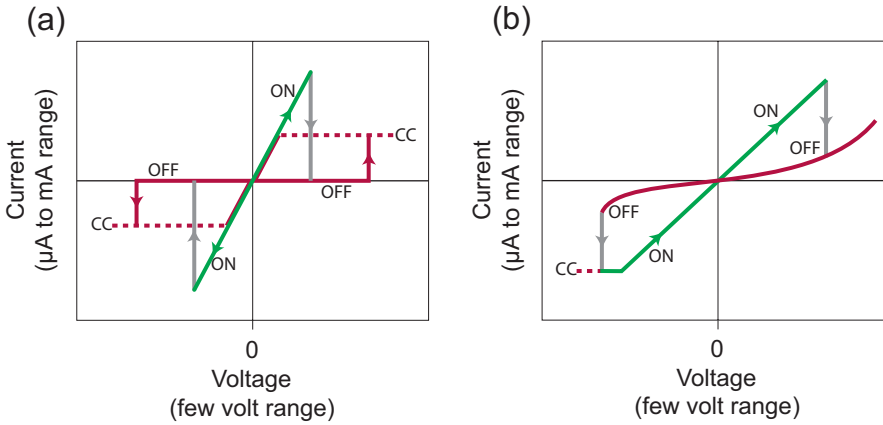


Figure 2.6: *Classification of switching characteristics [33]. The shown curves are exemplary and can vary considerably depending on the MIM structure. The dashed lines indicate that the current is limited to the compliance current (CC) value. Therefore, the voltage differs from the control voltage. (a) Unipolar switching: Set and reset operations are independent of the polarity. The set operation takes place at higher voltage and lower (CC) current levels than the reset operation. (b) Bipolar switching: Set and reset operations occur at opposite polarities.*

Depending on the electrical polarity, it can be distinguished between unipolar and bipolar resistive switching. Resistive switching independent of the polarity of the applied voltage and current signal is called unipolar (or symmetric), while switching dependent on the polarity is called bipolar (or asymmetric).

Unipolar devices are switched 'set' from the high-resistance (OFF) state to the low-resistance (ON) state by application of a threshold voltage as shown in Fig. 2.6 (a). The electrical current must be limited to a compliance current (CC) during the set process in order to prevent the device from instantly returning to the off-state, or even worse the possible memory cell destruction. This is due to the fact, that the 'reset' into the OFF state can take place at the same polarity. The reset operation occurs at a higher current and a lower voltage than the set threshold voltage.

Bipolar devices are switched (set operation) from the high-resistance (OFF) state to the low-resistance (ON) state by application of a threshold voltage at one polarity as shown in Fig. 2.6 (b). The current is often limited by a current compliance during the on-switching operation in order to prevent a possible memory cell destruction. The reset operation takes place at the opposite polarity by application of a different threshold voltage. The MIM structure of the system must have some asymmetry (different electrode materials, electroforming step, etc.) in order to show bipolar switching behavior.

In many of the MIM structures, especially the binary and multinary oxides, and the higher chalcogenides an initial electroforming step, such as a current-limited electric breakdown, is induced in the virgin sample. This step provides a necessary preconditioning of those systems, which afterwards can be switched between the ON and the OFF state.

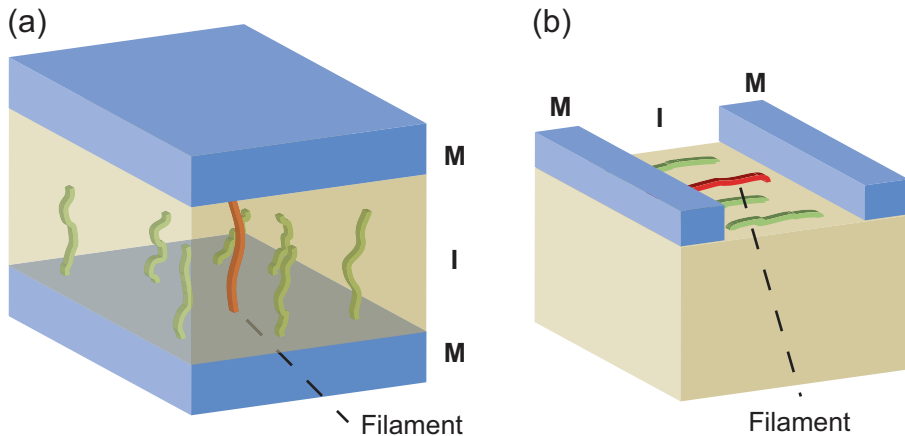


Figure 2.7: *Filamentary conduction in MIM structures. (a) Vertical MIM structure and (b) lateral (planar) MIM structure. The red (dark) filament in these cases connects the two electrodes and is therefore responsible for the ON state.*

2.2.1 Switching Mechanisms in MIM Structures

One important aspect, considering the physical mechanisms responsible for the observed resistive switching effect in MIM devices, is the actual geometric location of the switching event in the structure. In most publications, the switching to the low resistance state is reported as a locally limited process. In this case, the effect is therefore not homogeneously distributed in the material but has rather a confined, filamentary nature, which leads to a pad size independent ON state resistance. In Fig. 2.7 such a filamentary conduction is shown exemplary for a vertical (a) and a lateral (b) MIM structure. In addition, evidence for an interfacial nature of the reproducible switching are described more frequently in the literature than bulk switching effects [33]. These interface effects occur at a thin area close to the electrodes.

The actual underlying physical switching mechanism is still unclear for many of the reported MIM structures. Proposed explanations are often based on little experimental and theoretical evidence. In addition, many publications are short on detailed experimental information, on device fabrication, and measurement parameters. Therefore, it is difficult to obtain a clear overview and classification of the numerous material combinations. Either way, the conceivable proposed mechanisms in MIM systems are based on a combination of physical and/or chemical effects.

Waser et al. recently proposed a coarse-grained classification of the MIM structures into three main categories, according to whether the dominant contribution comes from a thermal, an electronic, or an ionic effect [33]. The first category includes all devices, whose switching mechanisms are primarily based on thermal effects. The second is comprised of all concepts, whose switching mechanisms are primarily based on electrical effects. The third includes all devices, whose switching mechanisms are primarily based on ion-migration effects and is subdivided into cation-migration cells and anion-migration cells.

MIM structures, whose switching is primarily based on thermal effects typically

display unipolar characteristics with current–voltage characteristics comparable to Fig. 2.6 (a). The switching process of this thermally based effect is similar to the mode of operation of a traditional household fuse. The essential component of a traditional fuse is a metal wire or strip that melts due to Joule heating, if too much current flows through it. If the metal strip melts, it opens the circuit. MIM devices based on thermal effects show a similar behavior on the nanoscale as a traditional fuse on a macroscopic level. Such a MIM structure is initiated by a voltage–induced partial dielectric breakdown. During this breakdown a discharge filament is formed, which can be composed of either electrode material transported into the insulator or decomposed insulator material such as sub-oxides [34]. The MIM cell is in the ON state if both electrodes are connected through a filament (see Fig. 2.7). In order to reset the device to the OFF state, a high current is driven through the cell. This results in a Joule heating of the filament until it is thermally disrupted. Recently, Samsung presented the successful integration of Pt/NiO/Pt MIM cells into CMOS technology and demonstrated non-volatile memory operation based on the described ‘fuse–antifuse’ mechanism [35].

There are some different proposed models/theories trying to explain the resistive switching in MIM devices based on electrical effects. Electronic charge injection and/or charge displacement is seen as one origin of the switching. As early as 1967, Simmons and Verderber proposed a charge–trap model which can explain the different resistance states of a MIM cell by the modification of the electrostatic barriers due to trapped charges [36]. According to this model, charges are injected by Fowler–Nordheim tunneling at high electric fields and subsequently trapped at sites such as defects or metal nanoparticles in the insulator. This model was later modified in order to incorporate charge trapping at interface states, which is thought to affect the adjacent Schottky barrier at various metal/semiconducting perovskite interfaces [37]. Another proposed explanation for perovskite–type oxides is based on the insulator–metal transition (IMT) [38]. In this model, the electronic charge injection acts like doping, which induces an IMT [39, 40].

The third category contains all MIM systems in which the resistive switching is primarily based on ionic transport and electrochemical redox reactions. This is a research field where nanoelectronics [3] intersects with nanoionics [41]. MIM devices based on these mechanisms display bipolar current–voltage characteristics qualitatively comparable to Fig. 2.6 (b). This category can be divided into two subcategories, one based on cation migration and one based on anion migration.

The resistive switching of MIM devices based on cation migration can be described exemplary on the basis of a PMC [13]. The setup of such a simple PMC is shown in Fig. 2.8. A solid electrolyte layer is sandwiched between the two electrodes, of which one is made of silver. During the set process (Fig. 2.8 (a)), a positive bias voltage is applied to the silver electrode and causes the oxidation of the electrochemically active electrode metal (Ag). The resulting Ag^+ -ions are mobile in the solid electrolyte and drift due to the electrical field towards the cathode. These cations discharge at the negative charged (inert) counterelectrode leading to the growth of Ag dendrites. The dendrite forms a highly conductive filament when reaching the anode. The PMC is then in the low resistance ON state. The reset process occurs by application of a reversed voltage. If a negative bias voltage is applied to the silver electrode, an electrochemical dissolution of the conductive bridges takes place, resetting the system into the OFF state (Fig. 2.8 (b)). Copper is also often used as electrode material, due to

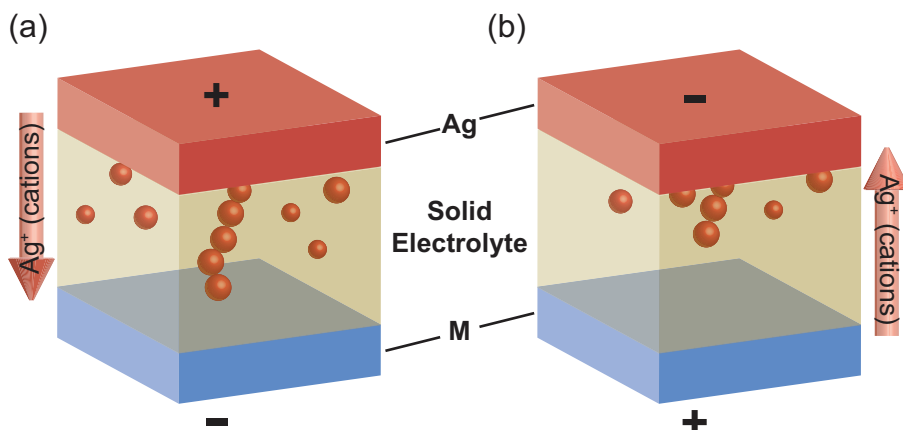


Figure 2.8: Schematics of the cation movement in a PMC. (a) Electrodeposition of Ag^+ –ions during the set process (positive bias voltage applied to the Ag). (b) Removal of Ag^+ –ions during the reset process (negative bias voltage applied to the Ag).

its comparable electrochemical potential and mobility. Another example for a cation driven MIM device is the so called atomic switch proposed by Aono et al. where the insulating layer is a thin vacuum area (≈ 1 nm) which is bridged by a Ag dendrite in the ON state [42].

The second subcategory operates through the migration of anions, typically oxygen ions. This is feasible due to the fact, that in many oxides, in particular in transition metal oxides, oxygen ion defects are much more mobile than cations. The oxygen ions are migrating under the influence of the electrical field towards the anode. However, the process can be better understood with a description based on oxygen vacancies instead of oxygen ions. These vacancies migrate the other way around, namely towards the cathode. This results in a change of the stoichiometry and a valence change of the cation sublattice, which is associated with a modified electronic conductivity [43].

2.2.2 MIM Structures Based on Organic Materials

In addition to the previously presented MIM systems, a vast number of organic devices have been reported to show resistive switching. In these MIM systems, the 'I' layer is represented by a thin film (typical thicknesses of 20 nm to >1 μm) of organic molecules or polymers. Scott et al. categorized the organic devices proposed for RRAM into six groups in a recent review [44]:

Category 1: Homogeneous–Polymer–Based Structures

These MIM systems with a homogeneous polymer as 'I' are the simplest structures and the earliest reported. Some examples for the homogeneous polymers are e.g. poly(divinylbenzene) [45], styrene [46], acrylates [47], thiophene derivatives [48], etc.

Category 2: Small-Molecule–Based Structures

Many small-molecule organic semiconductors have been used as 'I' in MIM devices, for example anthracene [49], pentacene [50], Alq3 [51], etc. Recently also monomolecular films (e.g. rose-bengal [52]) or even single molecules (e.g. catenane based switches [53]) have been presented in MIM structures.

Category 3: Donor–Acceptor Complexes

Electron donor–acceptor complexes have been explored as resistive switching materials due to the conductive properties of these charge transfer (CT) complexes. Both organic–organic (e.g. biscyanovinyl–pyridine and decacyclene [54], etc.) and metal–organic (e.g. Cu:TCNQ [14]) systems have been reported.

Category 4: Systems Containing Mobile Ions and Redox Species

Systems containing mobile ions and redox species (e.g. RbAg_4I_5 with MEH–PPV [55], etc.) are reported to display resistive switching. In these devices, the applied voltage electrochemically oxidizes or reduces the polymer with an ionic species serving as countercharge.

Category 5: Blend of Nanoparticles in Organic Host

Systems with metallic nanoparticles (NP) blended into an organic host also display bipolar switching (e.g. polystyrene [56]).

Category 6: Molecular Traps Doped into an Organic Host

Recently, there are some reports on devices consisting of molecular traps doped into an organic host [57], [58].

The proposed underlying physical mechanisms responsible for the resistive switching of these organic MIM structures are diverse and in many cases not indisputable proven. Some suggested mechanisms are:

- Highly localized filamentary conduction (as described in 2.2.1) [29]
- A change in the number of free carriers (proposed e.g. for the charge transfer in donor–acceptor complexes [59] and for NPs acting as acceptor/donor in an organic host [56])
- Electrochemical doping of a conducting polymer [60]
- Manipulation of the Coulomb blockade due to trapped charges [61]
- Inherent electronic molecule properties [62, 63]
- etc.

The above-mentioned examples demonstrate the large number of different approaches in order to explain the resistive switching phenomena in organic MIM devices. However, in many cases the database is too weak or inconclusive to draw definite conclusions regarding the microscopic nature of the effects. In addition, it is noteworthy that in quite a few studies an aluminum top electrode has been used. Between the organic material and the aluminum electrode the formation of a thin aluminum oxide layer is inevitably, if the device is not prepared and encapsulated in-situ under vacuum. Recent studies demonstrated that this thin naturally formed oxide layer, and not the organic material, can be responsible for the resistive switching [64, 65]. A similar mechanism was revealed for specific designed monolayers of catenane molecules with titanium topelectrodes [66]. In this case, a thin titanium oxide layer is made accountable for the resistive switching comparable to MIM devices based on oxides as

described in section 2.2.1.

In conclusion, the understanding of the microscopic origins of the switching mechanisms in nearly every organic MIM structure is still a topic of active debate. The few, above-mentioned, examples show that great care must be exercised when attributing models to observed switching events. One main reason for this is a lack in measurements that go beyond the observation of resistive switching. Additional studies are necessary in order to distinguish between possible candidate mechanisms. Furthermore, in some cases undesirable phenomena, such as self-healed breakdown, are probably mistaken for reproducible switching.

2.3 The Charge Transfer Complex Cu:TCNQ

One of the promising organic materials used in resistive switching MIM devices is the metal-organic charge transfer complex Cu:TCNQ. In this material system copper acts as the metallic donor and Tetracyanoquinodimethane (TCNQ) as the organic acceptor. Potember et al. were the first to report electrical field induced resistive switching effects in such thin films sandwiched between a copper and an aluminum electrode [14]. A short introduction and overview about some basic principles of CT complexes in general and this material system in particular, will be given in the following sections.

Charge Transfer Complexes

Charge transfer complexes are part of the donor-acceptor class, whose members are composed of two different types of molecules in a certain stoichiometric ratio [67]. In a CT complex, one of the molecule types is an electron donor while the other is an electron acceptor. The donor molecule possesses a low ionization potential whereas the acceptor molecule has a strong electron affinity. As individuals, both types of molecules (or atoms) are charge neutral. Combined in a CT complex, the free energy is lowered by a (partial) charge transfer from donor to acceptor. The degree of this charge transfer is abbreviated as δ and adopts values $0 < \delta < 1$. In the used nomenclature, $\delta = 0$ represents no charge transfer, while $\delta = 1$ stands for a complete charge transfer from donor to acceptor. Depending on the conditions, this transfer results in partially occupied atom or molecule orbitals which influence the charge transport properties.

In organics that are composed of one type of molecules (e.g. polymers), inter molecular bonds are due to van der Waals forces. In CT complexes, additional Coulomb and dipole induced forces can have a strong impact on those inter-molecular bonds. Depending on those forces, the systems are classified into weak CT complexes and radical ion salts (or strong CT complexes). The transition between those groups is continuous and depends on the δ value.

Weak CT complexes are composed of molecules with fully occupied electron shells. The charge transfer δ between donor and acceptor is only marginal in the ground state, but can be much larger in the excited state. Typically, weak CT complexes crystallize in a structure where donor and acceptor molecules are stacked alternately as shown in Fig. 2.9 (a). An example for such a system is tetrathiafulvalene(TTF):TCNQ [68].

In contrast, **radical ion salts** (or strong CT complexes) display a strong ionic character.

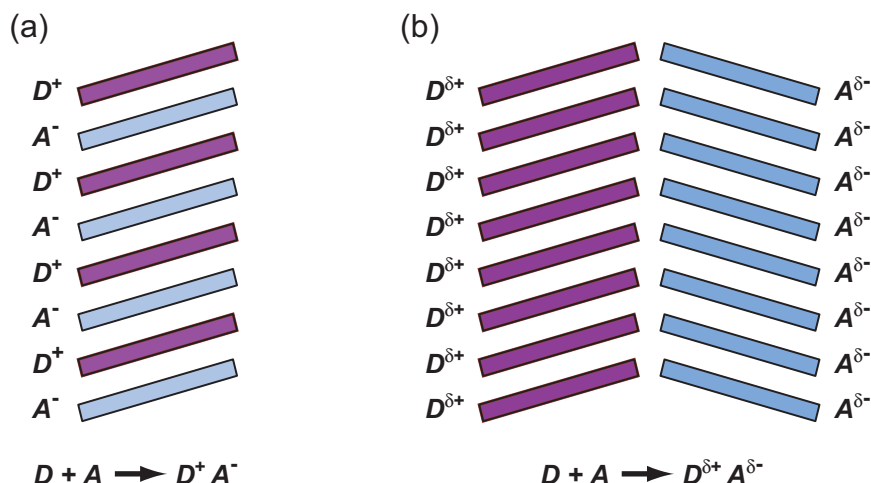


Figure 2.9: Possible configurations of the donor–acceptor molecules in a CT complex [67]. (a) Alternating stacking of donor (D) and acceptor (A) molecules, which is typical for weak CT complexes. Such crystals are insulators or semiconductors. (b) Separated stacks of donor and acceptor molecules with partial charge transfer δ , which is typical for radical ion salts. Such crystals are good conductors along the stack direction or highly anisotropy semiconductors.

This is due to a large charge transfer δ between donor and acceptor, even in the ground state. Typically, radical ion salts crystallize in a structure where donor and acceptor molecules are stacked separately as shown in Fig. 2.9 (b). An example for such a system is Cu:TCNQ [14]. It is possible to use a more precise classification of the radical ion salts which takes into account the different ionic types. In this case, three different types can be distinguished [69]. The first one, radical ion salt, is used for CT complexes where both types of ionized molecules are radicals due to the charge transfer. In this regard, radical means that unpaired electrons on an otherwise open shell configuration are present. Therefore, both molecules possess an electron spin. The second one, radical cation salt, is used for CT complexes where only the cation is a radical. In this case, the anion possesses a fully occupied electron shell and therefore no electron spin. The third one, radical anion salt, is used for CT complexes where only the anion is a radical. In this case, the cation possesses a fully occupied electron shell and therefore no electron spin. $\text{Cu}^+ \text{TCNQ}^-$ is an example for an anion radical salt.

2.3.1 The Organic Ligand TCNQ

The detailed nomenclature of the organic ligand in the studied CT complex Cu:TCNQ is 7,7',8,8'–Tetracyano–1,4–quinodimethane. The base of this molecule is the chemical compound 1,4–Benzoquinone with the formula $\text{C}_6\text{H}_4\text{O}_2$. This nonaromatic six-membered ring compound is the oxidized derivative of 1,4–hydroquinone. In the TCNQ molecule the oxygen is substituted by four cyano $\text{C}\equiv\text{N}$ (or nitrile) groups at the carbon positions 7,7',8,8' as stated in the TCNQ nomenclature. The chemical sum formula for TCNQ is $\text{C}_{12}\text{H}_4\text{N}_4$. The structure of the TCNQ molecule is shown

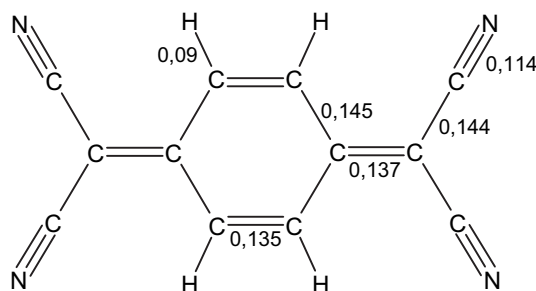


Figure 2.10: Chemical structure of the TCNQ molecule. The numbers denote the molecular bond lengths in nm calculated by Long et al. [71].

in Fig. 2.10. The electrons are localized in the benzene ring, which means that the molecule has no aromatic character. As shown in Fig. 2.10, the upper and lower carbon atoms are connected by a covalent double bond. This double bond consists of one σ -bond and one π -bond. The four functional cyano groups have a negative mesomeric (or resonance) effect on the quinoid carbon ring. The TCNQ molecule acts as an acceptor due to this electron withdrawing properties [70]. By accepting electrons, it is transformed from the quinoid to a conjugated system with a favorable energetic configuration.

TCNQ crystallizes in an orange colored monoclinic structure [71]. In these crystals the TCNQ molecules are stacked in a herringbone structure, which is typical for many planar organic molecules. The angle between the planes of molecules in adjacent stacks is 48° . The perpendicular distance between the planes of adjacent molecules within a given stack is 3.45 \AA , only about 0.1 \AA more than that in graphite. The intermolecular bonds in the TCNQ crystals are van der Waals forces, which are weak compared to covalent and ionic bonds. This crystal structure allows for an overlapping of the π -orbitals of neighboring TCNQ molecules in the stack. This configuration is responsible for a good conductivity along the stack direction.

2.3.2 Formation of Cu:TCNQ

Soon after TCNQ was first synthesized successfully [72, 73], experiments with metal-TCNQ CT complexes were conducted. Studies by Melby et al. in the DuPont laboratories on this M:TCNQ salts raised interest due to the high conductivity values of these organic systems [70]. The complex anion-radical salts exhibited the highest electrical conductivities known for organic compounds at that time, with volume electrical resistivities as low as $0.01 \Omega/\text{cm}$ at room temperature.

Mainly, there are two different deposition methods described for Cu:TCNQ thin films. The method developed the earliest is a wet chemical process [73]. This chemical solution deposition (CSD) method is based on a spontaneous electrolysis technique [14]. A copper electrode is cleaned in order to remove a possible oxide layer and then immediately dipped into a saturated solution of TCNQ. Upon contact with the solution, a direct oxidation reaction between Cu and TCNQ takes place [74, 75]. This corrosion

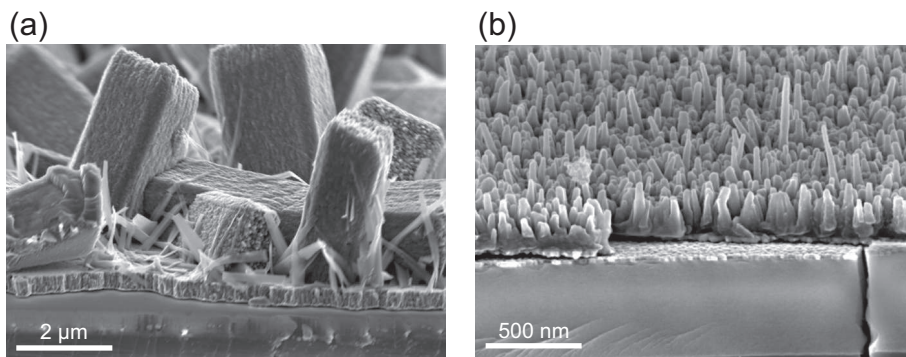
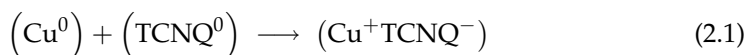


Figure 2.11: SEM Images of the Different Morphologies of Cu:TCNQ thin films. (a) Cu:TCNQ thin film prepared by a wet chemical process in an acetonitrile ($C_2H_3N_4$) solution saturated with TCNQ. (b) Cu:TCNQ thin film prepared by PVD on a Cu layer with subsequent thermal activation.

reaction is described in Eq. 2.1.



With this technique, Cu:TCNQ thin films with thicknesses in the micrometer range can be grown in short time (minutes) [14].

The second method is a physical vapor deposition (PVD) process which takes place in high vacuum (HV) or even ultra high vacuum (UHV). Using this technique, the TCNQ is thermally evaporated on a Cu layer [59]. A thermal activation is necessary in order to accelerate the diffusion of Cu into the TCNQ layer and trigger the above stated reaction (Eq. 2.1). The PVD process will be described in section 3.3 in more detail.

Within the framework of this study, both preparation types were implemented. Since the main focus of this work was on the establishing and optimization of the PVD process, only a few control samples were prepared by a CSD method using a solution of acetonitrile ($C_2H_3N_4$) saturated with TCNQ. A clear difference between the two preparation types can be seen in the morphology of the resulting thin films on scanning electron microscope (SEM) images as shown in Fig. 2.11. The Cu:TCNQ layer prepared by the wet chemical method consists mainly of micrometer sized, rectangular blocks (Fig. 2.11 (a)). In contrast, the film prepared by PVD displays a nanometer sized columnar structure (Fig. 2.11 (b)).

Heintz et al. demonstrated in a recent study the existence of two markedly different polymorphic phases of Cu:TCNQ [74]. A simple schematic view of the two different structures is shown in Fig. 2.12. The structures of both phases are based on the repeat pattern of a four-coordinate Cu ion ligated to the nitrile groups of separate TCNQ molecules. However, two important differences can be seen which lead to entirely different spatial arrangements of the TCNQ units in the two phases.

The first difference is the relative orientation of TCNQ moieties around the Cu atoms. In Phase I and in all other metal-TCNQ compounds with a stoichiometric ratio of 1:1, neighboring TCNQ molecules are rotated 90° with respect to one another. In contrast,

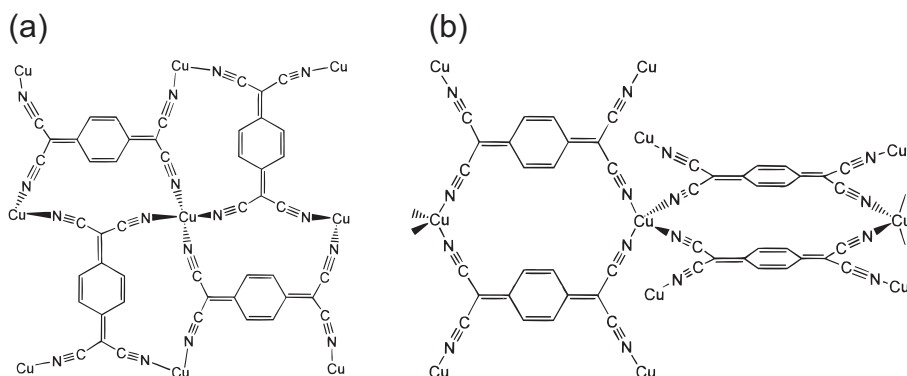


Figure 2.12: Schematic drawing of the orientation of TCNQ⁻ in Cu:TCNQ [74]. (a) In the crystallographic Phase I. (b) In the crystallographic Phase II.

Phase II displays a different structure where an infinite number of coplanar TCNQ molecules are oriented in the same direction, but in two perpendicular planes. The second major difference concerns the type of interpenetration of the networks. In Phase I, the two independent networks result in a columnar stack of TCNQ molecules with the closest distance being 3.24 Å as shown in Fig. 2.13 (a). This distance allows for a π -orbital stacking. In sharp contrast, the interpenetration in Phase II does not bring the two independent networks together. The TCNQ rings are in fact out of alignment and no π -stacking occurs as shown in Fig. 2.13 (b). In this case, the closest distance between parallel TCNQ units in the same network is 6.8 Å.

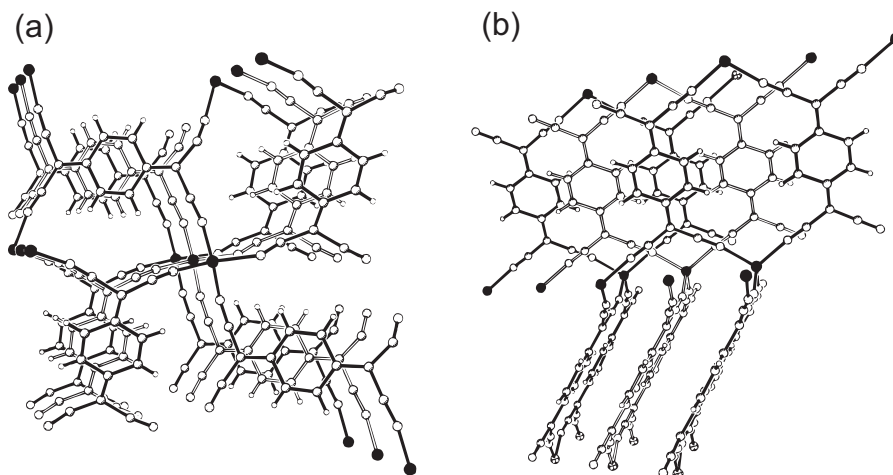


Figure 2.13: Views of interpenetrating networks in Cu:TCNQ crystals [74]. One network is labeled with solid bonds the other with open bonds. (a) In the crystallographic Phase I. (b) In the crystallographic Phase II.

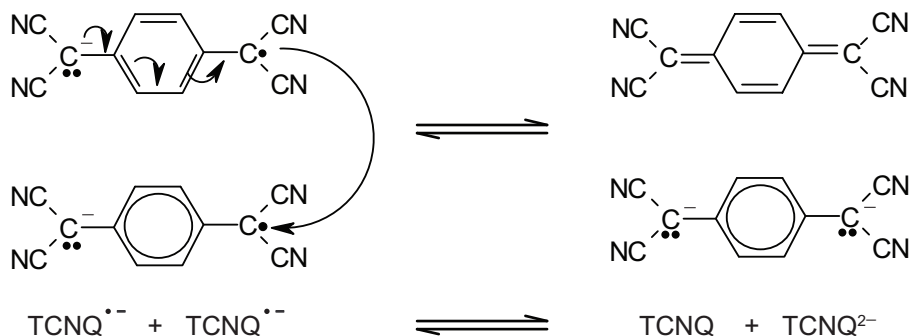
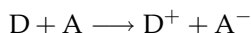


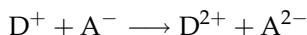
Figure 2.14: Conductivity in a CT complex with complete charge transfer ($\delta = 1$) using a TCNQ stack as example [76].

2.3.3 Conductivity of Cu:TCNQ and CT complexes in General

The conductivity of CT complexes is directly dependent on the crystal structure [76]. CT complexes with an alternating stacking of donor and acceptor molecules as shown in Fig. 2.9 (a) exhibit low conductivity values. This is due to a complete charge transfer from donor to the neighboring acceptor molecules:

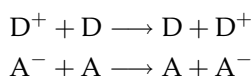


In this case, a further charge transfer (transport) is energetically disadvantageous. This is due to a necessary further ionization of the donor and acceptor molecules leading to a high ionization potential to be overcome:



Therefore, high conductivity values are only possible in CT complexes with separated stacks of donor and acceptor molecules as shown in Fig. 2.9 (b). However, this kind of stacking is mandatory, but not sufficient on its own for high conductivities. In addition, the degree of charge transfer δ has a decisive influence in this kind of systems. For example, the acceptor molecule TCNQ is negatively ionized for $\delta = 1$. A charge transfer within a TCNQ stack in this case would occur by the conversion of two $\text{TCNQ}^{\bullet-}$ anions to a neutral TCNQ molecule and a TCNQ^{2-} dianion as shown in Fig. 2.14. This dianion configuration is energetically unfavorable due to the high Coulomb potentials. Hence, a charge transfer of $\delta = 1$ results at maximum in conductivity values typical for semiconductors.

CT complexes with separated stacks of donor and acceptor molecules and partial charge transfer δ display the highest conductivity values. In this case, the charge transport occurs as follows:



One ionized and one neutral molecule are converted to a neutral and a ionized molecule. Therefore, charge can be transported without the presence of high energy barriers to be overcome. In Fig. 2.15, this is shown exemplarily for a TCNQ acceptor stack. Obviously,

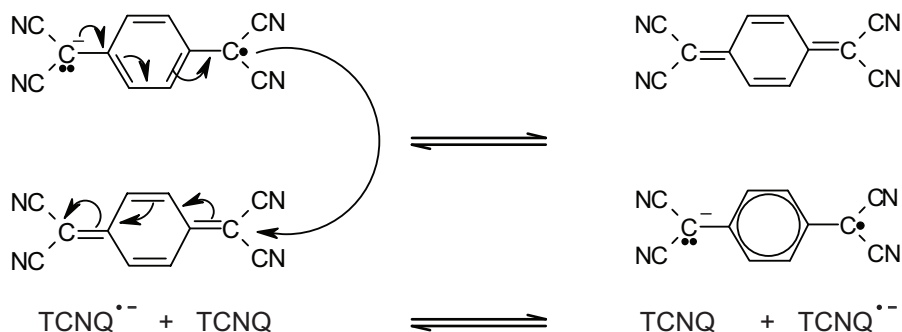


Figure 2.15: Conductivity in a CT complex with partial charge transfer using a TCNQ stack as example [76].

the distance between the single acceptor or donor molecules is also important for the conductivity. Short distances allow for a better overlapping of occupied and unoccupied orbitals.

The above-discussed conductivity mechanism, which is constricted to the direction along the stacks of the π -electrons of the molecules, is the dominating cause for the conductivity in CT complexes. In addition, a charge transport is also possible between the single stacks. This transport occurs between the central Cu atoms and the N atoms of the nitrile groups of TCNQ. The Cu ion is especially suitable for this process due to the d-orbital configuration. Thus, a good three-dimensional conductivity based on a $p\pi d$ -band is possible for CT complexes as Kato et al. showed for the radical ion salt copper-dicyanobenzoquinone-diimin (Cu:DCNQI) [77].

Heintz et al. measured the conductivity properties of Cu:TCNQ for the two crystallographic phases which were described in section 2.3.2. These measurements revealed semiconducting properties for both systems [74]. Phase I displayed a room-temperature conductivity of 0.25 S/cm and a band gap of 0.137 eV. In contrast, Phase II is a very poor semiconductor with a room-temperature conductivity of 1.3×10^{-5} S/cm and a band gap of 0.332 eV.

2.3.4 Resistive Switching in Cu:TCNQ

In 1979 Potember et al. were the first to report an electrical field induced resistive switching effect in Cu:TCNQ thin films sandwiched between a copper and an aluminum electrode [14]. In their study, 10 μm thick microcrystalline Cu:TCNQ layers were grown on Cu substrates using a CSD spontaneous electrolysis technique. The current-voltage characteristic revealed an abrupt decrease in impedance from 2 M Ω to less than 200 Ω at a field strength of 4×10^3 V/cm independent of polarity. A switching time of roughly 15 ns was reported. After removal of the applied voltage, the device was observed to act as a threshold switch, returning to the high resistance state. In case of high power dissipation during on-switching, the memory switch was reported to remain in the on-state unless a short pulse of high current of either polarity was applied or the device was exposed to heating. In this case, the device returned to the off-state.

Source	Characteristic Switching Parameters						Remarks
	Sample Structure	R_{off}	R_{on}	$V_{th,off-on}$	$V_{th,on-off}$ ($I_{th,on-off}$)	Padsizes	
Potember et al. [14]	BE: Cu 10 μ m Cu:TCNQ TE: Al	2 M Ω	200 Ω	± 5.5 V	(\pm mA)	25 mm ²	unipolar prepared by CSD switching time 15 ns
Sato et al. [80]	BE: Cu 2 μ m Cu:TCNQ TE: Al	56 k Ω	2.4 k Ω	-3.5 V	+3.2 V	0.25 mm ²	bipolar prepared by CSD switching time 2.5 ms
Liu et al. [78]	BE: Cu ? μ m Cu:TCNQ TE: Al	10 k Ω	1 k Ω	± 7.2 V	(± 8 mA)	1 mm ²	unipolar prepared by CSD
Sun et al. [79]	BE: Cu 1 μ m Cu:TCNQ TE: Al	2.4 k Ω	6 Ω	± 0.4 V	(± 75 mA)	? mm ²	unipolar prepared by CSD
Oyamada et al. [81]	BE: Al 100 nm Cu:TCNQ TE: Al	30 M Ω	70 k Ω	+10 V	-9.5 V	1 mm ²	bipolar prepared by PVD
Mueller et al. [7]	BE: Cu 500 nm Cu:TCNQ TE: Al	2 G Ω	900 k Ω	-6 V	+5 V	0.05 μ m ²	bipolar prepared by PVD nanowires
Xiao et al. [82]	BE: Cu 500 nm Cu:TCNQ TE: Au	10 G Ω	150 M Ω	-10 V	+10 V	2000 nm ²	bipolar, lateral prepared by PVD single nanowire

Table 2.3: *Excerpt of published switching parameters for Cu:TCNQ devices. (BE: bottom electrode, TE: top electrode)*

Since then, several groups have observed a switching effect in Cu:TCNQ, however often with distinctive different characteristics. An extract of the different published switching parameters is summarized in Table 2.3. While some groups report unipolar characteristics [14, 78, 79], others observed bipolar behavior [7, 80–82] (for a general introduction to unipolar vs. bipolar see section 2.2). In addition, the reported resistance values vary greatly which cannot be explained by geometrical differences alone. Furthermore, the few published data regarding the intrinsic switching time are inconsistent, as much as the data referring to retention times.

Without doubt, this is one of the reasons why the underlying physical mechanism is still not clear. Different theories have been proposed as the microscopic origin for the resistive switching effect in Cu:TCNQ thin films and are still under discussion. Potember et al. postulated that a field induced solid–state reversible phase transition is responsible for the effect [14]. It was suggested that the following equilibrium equation (2.2) is shifted to the right due to an applied electric field to form the low impedance state, and to the left to form the high impedance state respectively [59]:



This means, that some of the reduced (TCNQ^-), and oxidized (Cu^+) ions are transformed to their neutral state due to an applied electrical field. This phase transition was also claimed to be the underlying mechanism for an optical switching effect observed in polycrystalline Ag:TCNQ and Cu:TCNQ films, which were proposed as erasable optical storage media [83]. This theory was supported by a study by Matsumoto et al. who reported switching and memory phenomena on Cu:TCNQ films triggered by a

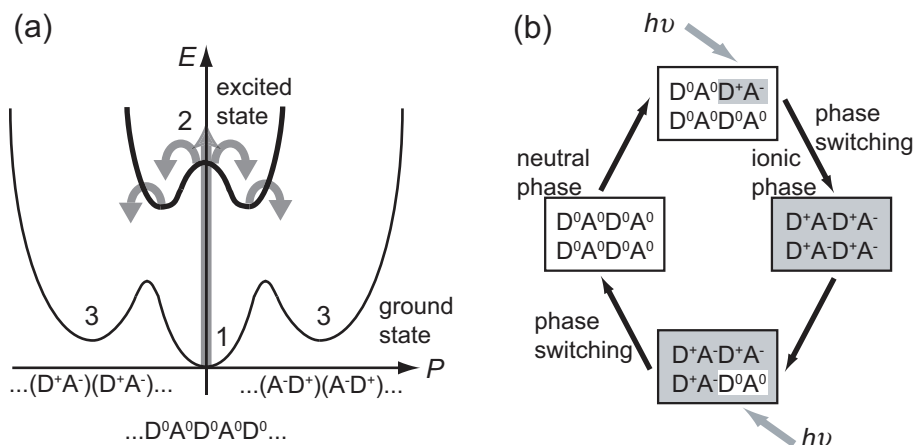


Figure 2.16: Schematic view of the photoinduced phase transition in CT complexes. (a) Neutral-to-ionic transformation path along the polar order parameter P . The stable neutral state is composed of homogeneous, nonpolar neutral chains where electron donor (D) and acceptor (A) molecules are regularly stacked (1). Photons excite DA pairs into an ionic state (2), and the coupling between the relaxed species makes the system switch to a metastable macroscopic state (3) [87]. (b) Phase change between neutral (D^0A^0) and ionic (D^+A^-) state triggered by photoinduced local CT excitation as a result of cooperative CT interaction. Arrows and $h\nu$ denote the photoirradiation for local CT excitation [88].

stimulus with a scanning tunneling microscope (STM) [84].

Such a phase transition as described in Eq. 2.2 for Cu:TCNQ, was demonstrated by Torrance et al. in a couple of alternating stacked CT complexes (Fig. 2.9 (a)) triggered by pressure [85]. Later, this phase transition was shown on tetrathiafulvalene-chloranil (TTF-CA, $C_6H_4S_4-C_6Cl_4O_2$) triggered by heat [86] and laser irradiation [87]. A schematic view of this photoinduced phase transition is shown in Fig. 2.16.

Gu et al. later expanded the phase transition model by using a one dimensional model for overlapping stacks of the donor material and the organic acceptor in the crystalline structure [89]. This model claims that the conductance in the high impedance state is dominated by charge transport along the TCNQ acceptor stacks as described in Fig. 2.15. The conductivity in this case, is limited by the overlapping of the π -orbitals of the molecules. By application of an increasing electrical field, electrons are supposed to occupy formerly unoccupied states in the Cu-N-bond, thereby weakening it. Finally, the bond between the Cu and the TCNQ molecule breaks. In this process, the reduction potential of the acceptor is proportional to the necessary field strength [14]. After the phase transition, acceptor and donor molecules exist in their neutral states. Due to the resulting delocalization of electrons in the TCNQ molecules, the conductivity along the TCNQ stacks is reduced. However, it is proposed that an increased conductivity along the now neutral metal donor stacks results in the low impedance state [89].

A different approach explaining the switching mechanism was presented by Heintz et al. [74]. As described in section 2.3.2, they demonstrated the existence of two different structural forms of Cu:TCNQ. The conductivity, in this case measured on bulk pellets

of the two different crystallographic phases, differed by some orders of magnitude. They concluded, that the resistive switching might involve a phase transition from a three-dimensional structure, that does not allow for TCNQ stacking, to a phase that brings parallel TCNQ radicals into close proximity. The fact that the resting state of the film, i.e. Phase II, is a centrosymmetric structure and that Phase I appears to be a non-centrosymmetric structure is seen to bode well for a piezoelectrically driven transition. However, the role of the electric field in the proposed structural transition is still unclear.

Furthermore, an approach based on the growth of filaments (see section 2.2.1) is also conceivable. Sakamoto et al. described a nanometer-scale switch that used a copper sulfide film [90]. In this case, the mechanism is explained by the creation and annihilation of conducting paths in the Cu_2S film. By applying a negative voltage to the top electrode, Cu ions are said to migrate towards the top electrode and to be neutralized by electrons provided by the electrode. By applying a positive voltage to the electrode, the Cu is reported to be ionized and dissolved into the Cu_2S film. A similar behavior might be considered for Cu:TCNQ devices.

All the above-mentioned approaches to explain the resistive switching in Cu:TCNQ have in common that the proposed microscopic mechanism occurs in the bulk of the material (bulk effect). Other approaches emphasize the importance of the interface to the electrodes. For example, Sato et al. proposed that the resistive switching in Cu:TCNQ can be described as a polarized memory effect [80]. As shown in Table 2.3, they observed a bipolar switching with a relatively high ohmic on-state compared to Potember et al. [14]. Furthermore, the switching speed of their devices is reported to be very low (≈ 2.5 ms). The proposed explanation for the switching effect is based on studies by Iwasa et al. on the negative resistance effect in CT complexes [91, 92]. The electric field assisted dissociation of charged defects in the contact region between Cu:TCNQ and Al and the succeeding multiplication of the charge carriers is suggested to be responsible for the effect. The switching speed should therefore be depend on the response of the charge carriers. Other groups proposed that a thin interfacial layer with a large dielectric constant is formed between the electrode and the organic [81, 93]. Therefore, a high built-in field is supposed to be formed between the electrode and the Cu:TCNQ layer. This field reportedly controls the partial charge transfer between donor and acceptor and thus the phase transition described earlier.

Some of these introduced approaches are discussed in more detail in section 5 regarding their plausibility in light of new results obtained within this thesis.

3 Device Preparation

The main aim of this thesis, as described in section 1.3 is to improve the physical understanding of the resistive switching effect in Cu:TCNQ thin films. This task can be broken down into subtasks, which are displayed in the flow-chart in Fig. 1.1. The upper parts of this schematic regarding the preparation, namely:

- Design and construction of a high vacuum chamber (3.2)
- Development of thermal evaporation processes for the deposition of Cu:TCNQ thin films (3.3)

are reported in this chapter.

3.1 Choice of the Deposition Method

There are numerous methods (e.g. MOCVD, ALD, e-Beam, Sputtering, CSD, etc.) known for the deposition of thin films. The selection of the process type is essential for quality and properties (e.g. thickness, structure, etc.) of the deposited film. The choice of the method has to reflect the physical and chemical properties of the material and the substrate. In addition, it is always wise to consider costs and feasibility of the deposition method regarding industrial utilization in application oriented research.

Contents

3.1	Choice of the Deposition Method	33
3.1.1	Basic Principles of Vacuum Evaporation	34
3.2	Design and Construction of the Evaporation Chamber	36
3.2.1	Setup of the Vacuum Chamber	37
3.2.2	Generation of the Vacuum Pressure	37
3.2.3	Tooling of the Evaporation Chamber	42
3.2.4	Control and Regulation of the System	45
3.3	Development of the Deposition Processes	48
3.3.1	Successive Evaporation Route	50
3.3.2	The Annealing Process	53
3.3.3	Simultaneous Evaporation Route	57
3.3.4	Device Setup	62
3.4	Summary	68

The deposition of Cu:TCNQ thin films so far has been realized with two different methods. As described in section 2.3.2, these methods are CSD and PVD. Preparation by CSD was carried out on some control samples in the scope of this study. First, the Cu bottom electrode was cleaned and the oxide layer was removed with acetic acid (CH_3COOH). The activated Cu surface was then immediately dipped into a solution of acetonitrile (CH_3CN), which had been saturated with neutral TCNQ^0 . Since the CT complex, which is formed by the direct oxidation reaction described in Eq. 2.1, is insoluble in CH_3CN , unlike TCNQ^0 , it is possible to grow a highly microcrystalline Cu:TCNQ salt directly on the Cu electrode. A typical resulting layer is shown in Fig. 2.11 (a). These experiments confirmed the results published in the literature [14, 74, 93] that thickness, reproducibility, and surface roughness are hard to control with the CSD process.

The second method is a PVD process. A thermal evaporation process is favorable for the deposition of organic materials due to the moderate complexity (compared to e.g. MOCVD) and relative gentle approach (compared to e.g. sputter processes). Furthermore, different studies showed [59, 81], that the PVD deposition of Cu:TCNQ thin films allows for a better control of thickness and reproducibility. Because of these data, it was decided to pursue the PVD method for the device fabrication. In order to do this, it was necessary to design and construct a vacuum evaporation chamber with two independent evaporation sources, one for Cu and other electrode metals, and one for the organic material (TCNQ). This allows for both, the subsequent in-situ deposition of a copper electrode and a TCNQ layer, and a simultaneous evaporation of both materials together. As additional features, a control of the evaporation rates and a possible heating/cooling of the substrate holder were specified. Using these tools, it was possible to develop two different PVD routes, a standard successive route, where TCNQ is deposited on top of a Cu layer with subsequent annealing step, and a simultaneous route, where Cu and TCNQ are co-evaporated at a ratio of 1:1. The empirical and anticipated properties, which were taken into account during the decision making process for the two PVD and the CSD methods, are summarized in Table 3.1. A detailed description of the successive and simultaneous evaporation processes is given later in this chapter (section 3.3).

3.1.1 Basic Principles of Vacuum Evaporation

Evaporation processes are typically carried out under vacuum, although an evaporation under atmospheric conditions would be possible for many materials. The reasons for this are manifold. Some elements and impurities of the air have detrimental effects on the substrate and the material. In particular, these are oxygen (oxidation of elements, e.g. Cu), hydrocarbons, sulfur, and chlorine compounds.

In addition, evaporation processes are depending, among other things, strongly on the ambient pressure. This is due to the fact, that all liquids and solids have a tendency to evaporate to a gaseous form, and all gases have a tendency to condense back into their original form. For any given material there is a temperature depending pressure at which the gas of that substance is in dynamic equilibrium with its liquid or solid forms. The equilibrium vapor pressure is an indication of the material's evaporation rate and relates to the tendency of molecules and atoms to escape from its original form. The vapor pressure of any substance increases non-linearly with temperature

	CSD	PVD	
		successive	simultaneous
short process description	cleaned Cu surface dipped into CH ₃ CN solution saturated with TCNQ; spontaneous electrolysis (corrosion reaction)	thermal evaporation of TCNQ on Cu surface with subsequent thermally triggered diffusion + redox reaction	thermal co-evaporation of Cu and TCNQ on any electrode material
complexity, reproducibility	straight forward process, low reproducibility, difficult thickness control	easy to adapt, good reproducibility	difficult control of evaporation ratio, reproducibility depending on the ratio
structure of resulting Cu:TCNQ layer	large crystallites randomly stacked, very rough surface	columnar structure of nanowires perpendicular to the substrate, very rough surface	better homogeneity, uniform layer, smoother surface

Table 3.1: Comparison of deposition methods for Cu:TCNQ. Empirical and anticipated parameters for thin film preparation.

according to the Clausius-Clapeyron relation:

$$\frac{dP}{dT} = \frac{L}{T\Delta V} \quad (3.1)$$

where dP/dT is the slope of the coexistence curve, L is the latent heat, T is the temperature, and ΔV is the volume change of the phase transition. The equilibrium vapor pressure can be defined as the pressure reached, when a condensed phase is in equilibrium with its own vapor. In the case of an equilibrium solid, such as a crystal (e.g. TCNQ), this can be defined as the pressure when the rate of sublimation of a solid matches the rate of deposition of its vapor phase. For most solids this pressure is very low. Therefore, either the temperature of the material has to be increased considerably or the ambient pressure has to be decreased dramatically in order to allow the vapor pressure to become sufficient to overcome the ambient pressure. Since TCNQ molecules decompose at temperatures above 300 °C (as shown by Liu et al. [78]), low pressures during the evaporation process are necessary in order to reach reasonable deposition rates.

Furthermore, the ratio between the amount of evaporated to deposited material decreases with increasing pressure. This is due to the fact that the evaporated particles lose the directional characteristic of their movement after an average of four collision with other particles (e.g. residual gases). Ideally, the evaporated particles reach the substrate unobstructed. This means, that the mean free path λ should be large compared to the distance between the evaporation source and the substrate. In kinetic theory, the mean free path of a particle, such as a molecule, is the average distance the particle travels between collisions with other moving particles. Given, that the velocities of the residual gas particles follow statistical movements, a Maxwell distribution of velocities can be assumed. Therefore, the following relationship applies for the calculation of the mean free path:

$$\lambda = \frac{k_B T}{\sqrt{2} p_r \pi d^2} \quad (3.2)$$

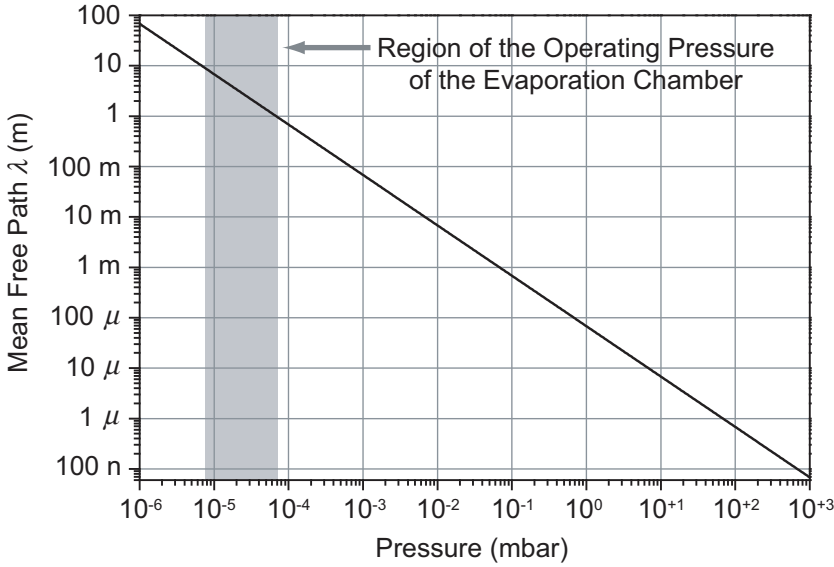


Figure 3.1: Mean free path λ as function of pressure. The graph is calculated with Eq. 3.2 for Cu atoms in air (empirical values used from [94]) at 20 °C. The operating pressure area of the designed vacuum chamber is highlighted in grey.

where T is the temperature, p_r is the residual pressure, and d is the diameter of the particle [94]. Approximated values for λ can be calculated using this equation. The mean free path for Cu atoms in air at room temperature (20 °C) is shown as a function of pressure in Fig. 3.1. The operating pressure of the evaporating vacuum chamber, which will be discussed later in section 3.2.2, is in the range of 8×10^{-6} mbar to 7×10^{-5} mbar. Therefore, the mean free path can be approximated to $\lambda \approx 1 - 10$ m. Considering that the distance between the thermal evaporation sources and the substrate is roughly 35 cm, as discussed later in section 3.2.3, these values theoretically allow for a decent condensation rate.

Another relevant parameter is the ratio between the number of residual gas molecules and evaporated molecules at the substrate surface [95]. This is important due to the fact, that residual gas molecules can be adsorbed at the substrate surface and remain there a certain amount of time until desorption. An equilibrium between adsorption and desorption is established at constant pressures. These temporarily adsorbed residual gas particles can interfere with the condensation of the evaporated material. Considering this parameter, a low pressure in the evaporation chamber is increasing the purity and quality of the deposited thin film.

3.2 Design and Construction of the Evaporation Chamber

All the basic principles and parameters regarding evaporation processes mentioned in the previous section (3.1.1) were taken into account for the design of the evaporation

chamber. Therefore, it was decided to construct a high vacuum system with two independent thermal evaporation sources, one for Cu and other electrode metals and one for the organic material (TCNQ). These sources were designed to be operated simultaneously or separately, controlled by a shutter system. A control of the evaporation rates was made possible by the use of a quartz crystal microbalance (QCM) measuring unit. In the following section, the different parts of the system are explained in detail.

3.2.1 Setup of the Vacuum Chamber

The main part of the evaporation system is the actual vacuum chamber. This chamber is bell-shaped and made of glass-bead-blasted, vacuum suitable stainless steel with a volume of 80 l. The bell has a diameter of 400 mm and a height of 500 mm. There are no ports mounted on the chamber besides a DN100 ISO-K viewport used to observe the processes. The bell is connected to an aluminum framework via a ball socket guidance, and can therefore be lifted by a cable winch as shown in Fig. 3.2. Due to this setup, the vacuum chamber can be opened and closed accurately and without back and forth swinging in order to change the substrates and/or refill the evaporation sources.

The correspondent vacuum chamber base plate is made of massive stainless steel with a diameter of 550 mm and a thickness of 22 mm. The connection to the vacuum bell is sealed by a Viton O-ring with a diameter of 400 mm. The own weight of the bell is sufficient to seal off the vacuum chamber at the beginning of the pump process.

The base plate has one central DN100 ISO-K flange, which is used to connect the pumping system, and eight additional DN40 CF ports for the connection of electrical feedthrough, shutters, etc. These ports are evenly aligned around the center port as shown in Fig. 3.3. Attached to this flanges are different pieces of equipment using partly reducer crosses and T-elements. The connections are listed in detail in Table 3.2, and a more detailed description of the elements is given later.

The base plate is mounted on the work plate as shown in Fig. 3.2. This work plate serves as protection of the below mounted devices (e.g. pumping system, electrical feedthroughs, etc.) from damage, and as a working space. It is integrated in the above mentioned aluminum framework, which is made of Item™ profiles. Overall, the evaporation system is build in a frame with the dimensions of 2 m (height), 1.27 m (width), and 1 m (depth). This framework is installed on wheels. Since the control and measuring equipment is mounted in a movable 19 inch measuring cabinet (for details see section 3.2.4), the whole evaporation system is easily portable.

3.2.2 Generation of the Vacuum Pressure

High vacuum conditions are necessary in order to obtain high evaporation rates at good qualities, as described in section 3.1.1. Therefore, the utilization of a two-stage pumping system was essential in the construction of the evaporation system. Momentum transfer pumps in conjunction with one or two positive displacement pumps are the most common configuration used to achieve high vacuums [96]. In this configuration, the positive displacement pump serves two purposes. To begin with, it obtains a rough vacuum in the vessel being evacuated, before the momentum transfer pump can be used to obtain the high vacuum, since momentum transfer pumps cannot

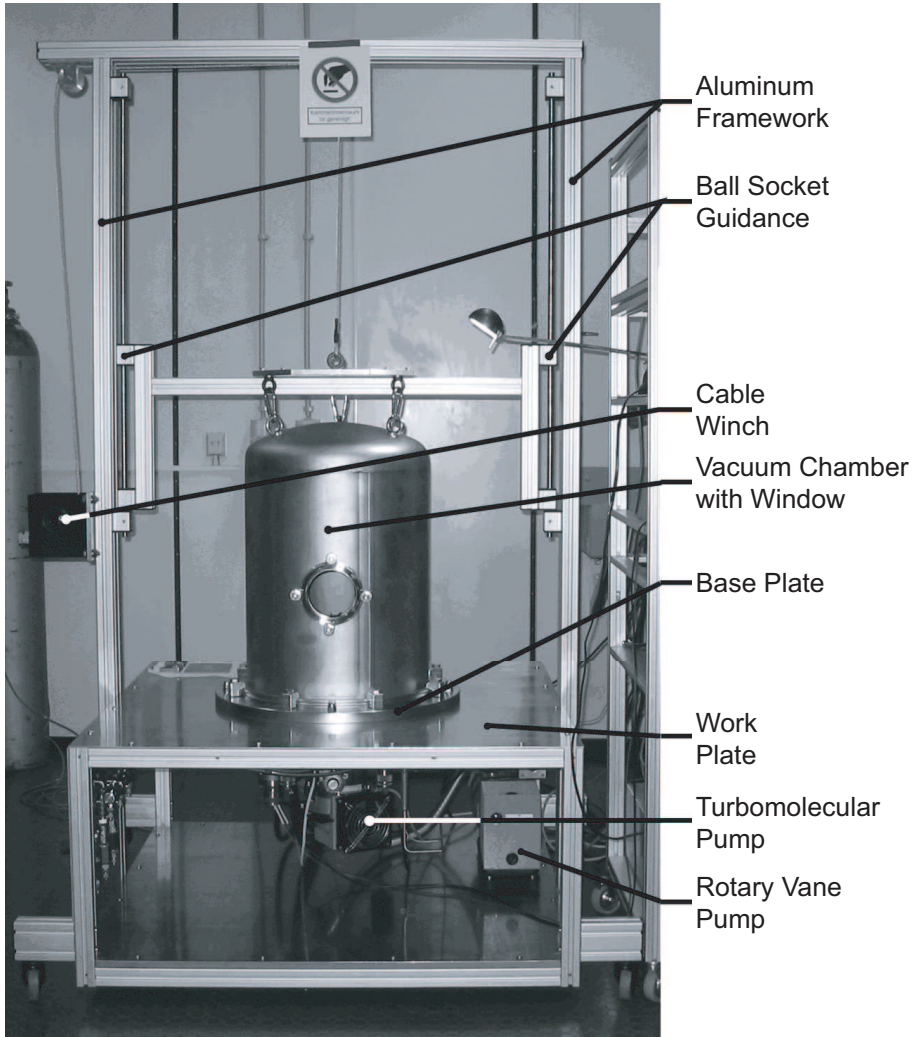


Figure 3.2: *Overview setup vacuum chamber.*

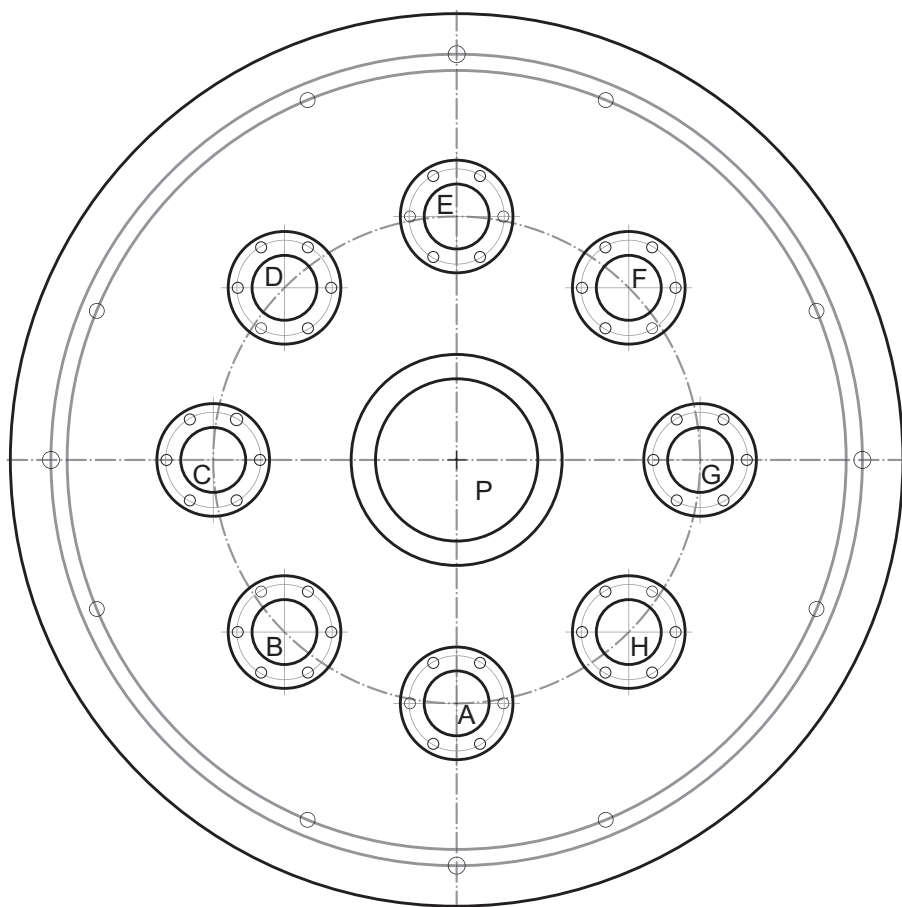


Figure 3.3: Overview vacuum chamber base plate. The diameter of the base plate is 550 mm. The connection to the vacuum bell is sealed by a Viton O-ring with a diameter of 400 mm. The use of the individual base ports is described in Table 3.2.

start pumping at atmospheric pressures. Secondly, the positive displacement pump backs up the momentum transfer pump by evacuating to low vacuum the accumulation of displaced molecules in the high vacuum pump.

Rotary Vane Pump

For the construction of this evaporation chamber, a Varian SD 300 dual-stage rotary vane mechanical vacuum pump was chosen as the positive displacement pump. A rotary vane pump is build-up of vanes mounted to a rotor that rotates inside of a cavity. This can be explained exemplary with the most simple vane pump, which is a circular rotor rotating inside of a larger circular cavity. Essential is an offset of the centers of these two circles, which causes eccentricity. The vanes are allowed to slide into and out of the rotor and seal on all edges, creating vane chambers that do the actual pumping work. On the intake side of the pump, the vane chambers are increasing in

Port	Type	Occupation
A	DN40 CF	shutter control for substrate (3.2.3)
B	DN40 CF	shutter control for source one (metal evaporation) (3.2.3)
C	DN40 CF	feedthrough for Eurotherm temperature measurement units for evaporation sources one and two, and substrate holder (3.2.4) + electrical feedthrough for the heating unit of the substrate holder (3.2.3) + needle valve
D	DN40 CF	high current electrical feedthrough for thermal evaporation sources one and two (3.2.3)
E	DN40 CF	feedthrough for the cooling water of the base plate setup (3.2.3) + integration of the vacuum measuring units (3.2.2)
F	DN40 CF	electrical and cooling water feedthrough of the QCM thin film thickness system (3.2.4)
G	DN40 CF	feedthrough for the cooling water of the substrate holder (3.2.3)
H	DN40 CF	shutter control for source two (TCNQ evaporation) (3.2.3)
P	DN100 ISO-K	vacuum pumping system (3.2.2)

Table 3.2: Occupation of base plate ports. Ports are labeled according to the base plate schematic shown in Fig. 3.3.

volume. These increasing volume vane chambers are filled with fluid forced in by the inlet pressure which normally is nothing more than the atmospheric pressure. On the discharge side of the pump, the vane chambers are decreasing in volume, forcing fluid out of the pump. The action of the vane drives out the same volume of fluid with each rotation.

In this case, the two-stage rotary vane vacuum pump can attain pressure differences of up to 10^5 . Considering the atmospheric pressure of 1×10^{-3} mbar, the fore-vacuum reached by this pump is as low as 1×10^{-2} mbar. The rotary vane pump is mounted on the vibration isolated aluminum plate at the lowest level of the system framework as shown in Fig. 3.2.

Turbomolecular Pump

The second stage of the vacuum system consists of a momentum transfer pump. In this type of pumps, gas molecules are accelerated from the vacuum side to the exhaust side, which is maintained at a reduced pressure by the above described rotary vane pump. The continuous use of a momentum transfer pump is only possible below pressures of approximately 1 mbar due to the pressure depending matter flow based on the laws of fluid dynamics. At pressures close to atmospheric conditions and mild vacuums, molecules are strongly interacting with each other and push on their neighboring molecules in what is known as viscous flow. At lower pressures the distance between the molecules increases, and the molecules are then interacting more often with the walls of the chamber than with other molecules. In this area, molecular pumping becomes more effective than positive displacement pumping. This regime is generally called high vacuum.

Molecular pumps generally sweep out a larger area than mechanical pumps, and do

so more frequently, making them capable of much higher pumping speeds. However, there is no seal between the vacuum and the exhaust side. This means, that a small pressure at the exhaust can easily cause a backstreaming of matter through the pump. In high vacuum however, pressure gradients have little effect on fluid flows, and molecular pumps can attain their full potential [96].

For the construction of this evaporation chamber, an Alcatel 5150 turbomolecular pump was chosen as the momentum transfer pump. A turbomolecular pump uses high speed fans to blow out gas molecules that diffuse into the pump by imparting momentum to the gas molecules. These pumps will stall and fail to pump if exhausted directly to atmospheric pressure, therefore they must be exhausted to a lower grade vacuum created, in this case, by a rotary vane pump. The Alcatel 5150 has a theoretical pumping speed of 140 l/s versus N_2 and a compression of 7×10^8 . The nominal rotation speed of this turbomolecular pump is 27 000 rpm.

It is advisable to use only the rotary vane pump at the beginning of the evacuation process until a pressure of at least 1×10^{-1} mbar is reached. This is due to the relatively large volume of the designed vacuum chamber and a possible degradation of the turbomolecular pump by usage at higher pressures. The Alcatel 5150 is mounted directly to the central DN100 ISO-K port of the base plate as shown in Fig. 3.2. With the described vacuum pump configuration, the operating pressure of the evaporation chamber is roughly 3×10^{-5} mbar as indicated in Fig. 3.1.

Pressure Measurement

The knowledge of the pressure in the vacuum chamber is important for the process control. A combined measuring unit for a wide range of pressures is necessary for the constructed vacuum chamber. During the evacuation process, the pressure decreases from atmospheric conditions to high vacuum. In the present case, the vacuum measuring system Alcatel CFA 212 was installed. This system consists of a control unit, a Pirani gauge (for atmospheric conditions to medium vacuum), and a Penning gauge (for high vacuum). Furthermore, a second, independent Penning gauge (an Edwards Penning 8) is installed as a backup and control unit.

A Pirani gauge is based on the fact, that a heated metal filament suspended in a gas will lose heat to the gas as its molecules collide with the wire removing heat and accelerating in the process [97]. This process is pressure dependent because the number of molecules present will fall proportionately with decreasing pressure. Therefore, the wire will rise in temperature due to the reduced cooling effect. Since the electrical resistance of a wire varies with its temperature, the pressure of the gas surrounding the wire can be determined by the measurement of this value. A Pirani gauge can be used for pressure measurement in the range between 1×10^{-3} mbar to 1×10^{-5} mbar.

A Penning gauge is a cold cathode ionization gauge. The working principle is based on the measurement of the amount of electrical ions produced, when the residual gas is bombarded with electrons [97]. The electrons, created by a high voltage electrical discharge (up to 4 kV), travel through the gauge and ionize gas molecules around them. The generated ions are collected at the anode. The resulting current depends on the number of ions, which in turn depends on the pressure in the gauge. Such gauges cannot operate if the ions generated by the cathode recombine before reaching the anodes. This happens, if the mean-free path of the gas within the gauge is smaller

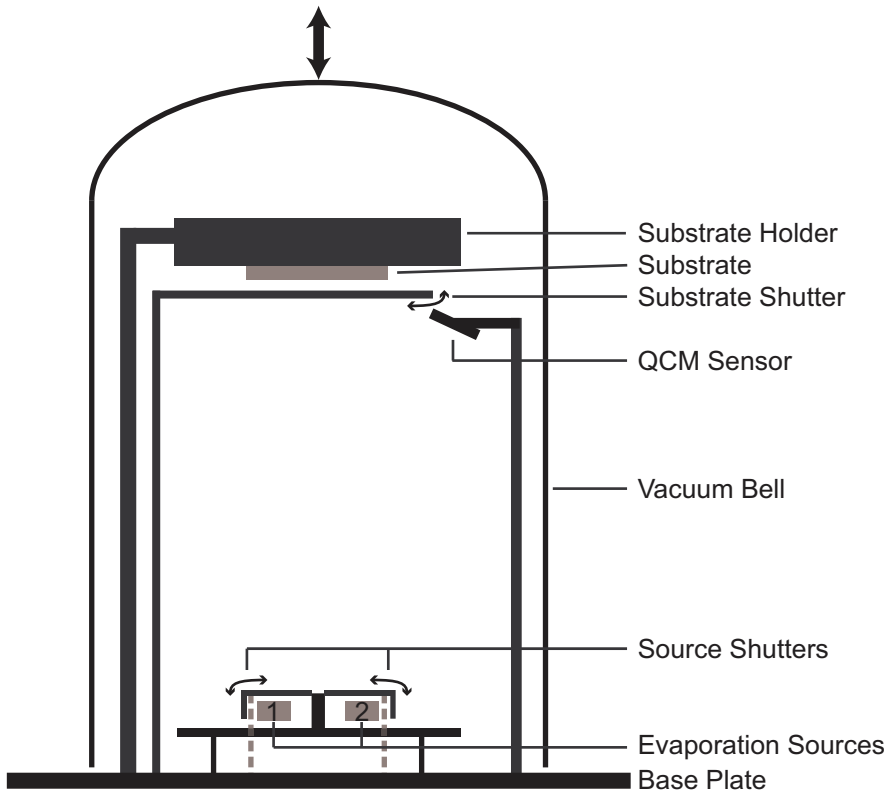


Figure 3.4: *Schematic overview of the interiors of the vacuum chamber.*

than the dimensions of the gauge. Then, the electrode current will essentially vanish. Therefore, Penning gauges are limited to operations below a pressure of roughly 1×10^{-3} mbar. In general, ionization gauges are sensitive to construction geometry, chemical composition of gases being measured, corrosion, and surface deposits. Therefore, a certain imprecision must be borne in mind, when using the measured pressures in the evaporation chamber.

3.2.3 Tooling of the Evaporation Chamber

The interior of the evaporation chamber was designed according to the requirements of the processes. A schematic drawing of the main components is shown in Fig. 3.4. A circular disc is mounted on top of the central DN100 ISO-K port. This installation aims at two purposes, the protection of the turbomolecular pump mounted directly to this port and the shielding of the evaporation sources. This disc can be cooled using a cooling water flow. This is necessary, due to the large heat dissipation of the evaporation sources, especially the metal one.

Thermal Evaporation Sources

Two independent evaporation sources are essential for the implementation of an evaporation process, where the organic compound TCNQ and the metallic donor Cu are deposited simultaneously. In order to minimize inhomogeneities in the relation of material quantities due to geometrical reasons, both sources should be placed as close to each other as possible. In this case, this was implemented by the use of the water cooled stainless steel disc with a solid screen between both sources as shown in Fig. 3.4. This design allowed for a minimum distance of ≈ 6 cm between the two sources, without interference between them.

In addition, the distance between the sources and the substrate should be large enough, so that both compounds can mix sufficiently. Furthermore, the distance is also important for a homogeneous thickness distribution on the substrate. These facts together with the necessity of taking into account the mean free path, as described earlier in section 3.1.1, results in a trade-off situation. Due to the working pressure of roughly 3×10^{-5} mbar the mean free path can be estimated by ≈ 3 m as shown in Fig. 3.1. Here, the distance between the sources and the substrate was set to 35 cm, which fulfills both requirements.

The actual sources use electrical resistance heaters in order to thermally evaporate the materials. In the case of source one, which is used mainly for Cu and other metals, evaporation boats made of thin tungsten sheets are used. Due to the high melting point of tungsten, these boats can be used up to temperatures of 1800 °C. In order to reach this temperature area, an electrical power of 260 W is necessary. Because of the low resistance of the tungsten boat of 26 m Ω at high temperatures, currents of up to 100 A are necessary. Therefore, two programmable DC power sources of the type Genesys GEN 6–100 are used for the supply of the two evaporation sources. These can provide a current of 100 A at a maximum voltage of 6 V. The connection between the power supplies and the evaporation sources is carried out by massive Cu cables using high current, high vacuum feedthroughs.

In the case of source two, which is used for the organic material TCNQ, evaporation boats made of thin molybdenum sheets are used. During some first test evaporations it could be observed, that TCNQ has a strong tendency to bounce during the heating process. Therefore, molybdenum boats with a top cover with multiple small circular openings were used. With these boats, the problem of material loss during the heating process could be evaded up to high evaporation rates.

The temperature is measured for both sources using thermocouples. In case of source two, a simple type K coated thermocouple is sufficient due to the low temperatures (< 300 °C) used for the evaporation of TCNQ. In contrast, a type S thermocouple (Pt-10% Rh versus Pt) is necessary for source one, because of the high temperatures (> 1200 °C) used for metal evaporation. The thermocouples are connected to two Eurotherm 2408 high stability temperature and process controllers. These are in turn connected to the power sources. More details on the control and regulation of the processes are described in section 3.2.4.

In addition, both evaporation sources can be opened and closed individually by different, manually operated shutters as shown in Fig. 3.4. This prevents a premature deposition of material during the heating, and a better control during the processes.

Material	Bulk Density	Z-ratio	Melting Point	Thermal Decomposition
Cu	$8.93 \frac{\text{g}}{\text{cm}^3}$	0.437	1084.4 °C	–
TCNQ	$1.36 \frac{\text{g}}{\text{cm}^3}$	1	–	300 °C

Table 3.3: QCM parameters for Cu and TCNQ.

Substrate Holder

The sample preparation can be carried out on different types of substrates. Given that the evaporation sources are positioned at the bottom of the chamber, facing up as shown in Fig. 3.4, the substrates must be clamped upside down to the substrate holder. For these purposes, different stainless steel plates were prepared. Three plates are made for 1 by 1 inch substrate pieces (for one, two or four pieces) and one for smaller pieces (1 by 1 cm). The respective plate is attached to the substrate holder using two clamps.

The actual substrate holder possesses an electrical resistance heating, which is implemented by electrically isolated metallic wires inserted into boreholes in the massive substrate holder. This electric heating is powered by a Heinzinger LNG 175–3 supply unit with a maximum electrical power of 150 W (3 A at 50 V). With this setup, the heating system can reach temperatures of up to 400 °C in a high vacuum environment. The power supply is connected to an Eurotherm 2408 controller, which uses a type K coated thermocouple for the temperature measurement of the substrate holder.

In addition, the substrate holder also possesses a cooling system in addition to the heating setup. A layer with an integrated, meander-shaped piping system is mounted on top of the heater layer, so that a thermal coupling is ensured. The piping system, in this case, is connected to a water supply with a maximum flow-rate of 21 l/min. In this configuration, the substrate heater can be cooled down to ≈ 10 °C within a short time (≈ 20 s). The cooling system is also prepared for the use of liquid nitrogen as coolant, however this option was not used during this study.

Furthermore, the attached substrate can be shielded from the evaporation sources by an additional, manually operated shutter as shown in Fig. 3.4. This allows the setting and regulation of the evaporation rates of the sources prior to the actual deposition process, without contamination of the substrate.

The QCM Sensor

The quartz crystal of the QCM monitoring unit is positioned adjacent and below the substrate shutter as shown in Fig. 3.4. In order to compensate for the shifted location relatively to the evaporation sources – substrate plain, the sensor is tilted slightly towards the vapor beam. The installed QCM monitoring system, in this case, is a XTC model from the vendor Inficon. The relevant parameters for the evaporation of Cu and TCNQ used for the QCM monitor are summarized in Table 3.3. Control measurements of the resulting thicknesses by SEM were used to calibrate the results of the QCM system.

3.2.4 Control and Regulation of the System

The installed components of the evaporation chamber possess several systems dedicated to measurement, control, and monitoring of the relevant parameters as described in the previous sections. The corresponding displays and operating controls are mounted in a 19 inch rack. A front view of this cabinet is shown in Fig. 3.5.

In addition to these automated devices, there are several manually operated controls. One group of these devices are the rotary feedthroughs of the shutters. The arrangement of these elements is shown in Fig. 3.6. For easy access they are located on the front side of the area underneath the base plate of the chamber. Furthermore, the flow rates of the different cooling systems (QCM sensor (3.2.3), substrate holder (3.2.3), and base plate setup (3.2.3)) are controlled manually. The valves are mounted on the left side of the evaporation system as shown in Fig. 3.7.

The application as a fully automated evaporation system is not possible due to the above mentioned manually operated controllers. However, due to the experimental nature of the carried out processes, this was not detrimental. On the contrary, given the multitude of parameters influencing the properties of the deposited thin films, the fast and straightforward manual control allowed for a greater flexibility. In the following, the individual partial control cycles implemented in the system setup are explained.

In spite of the various parameters, which have more or less pronounced effects on the deposition process, this work was focused on the influence of the source and substrate temperatures. Hence, other parameters, like the working pressure, were tried to be kept constant during the evaporation processes. The temperature of the resistance heated devices (evaporation sources one & two, and substrate holder) is measured by thermocouples. Each thermocouple is connected to an Eurotherm 2408 programmable temperature and process proportional–integral–derivative (PID) controller. The respective controller in turn is set to use the input of the thermocouple (the source or respectively the substrate holder temperature) as the process variable (PV) of the input–output control loop. The desired temperature, which is established by the user is called the setpoint. The difference between the measurement and the setpoint is the error, too hot or too cold and by how much. The output from the controller and input to the process (the power supplies) is called the manipulated variable (MV). In this case, the respectively Eurotherm 2408 outputs an analog signal between 0 and 10 V, which is used as input for the corresponding power supply. It is important to correctly adjust such a controller, in order to avoid either overshooting or delaying of the PV. The correct gains for the PID controllers were determined by test sweeps of the temperature range for the connected resistance heater – thermocouple systems. Therefore, the temperatures of the resistance heated devices are set by inputting them to the Eurotherm 2408 controllers, which will home in on these values controlling the current output of the power supplies.

All recordable parameters and measurement values can be logged in ASCII files using a personal computer (PC). For these purposes, the Eurotherm 2408 controllers are connected to the PC via RS-232 interfaces. The Alcatel 212 pressure measurement system and the Inficon XTC QCM device are connected using a 8 channel, 12 bit, CIO-AD08 analog–digital controller card from the vendor Measurement Computing. A Labview program was written, which can display and store the relevant values during the deposition processes. The measurement, control, and regulator circuits of the

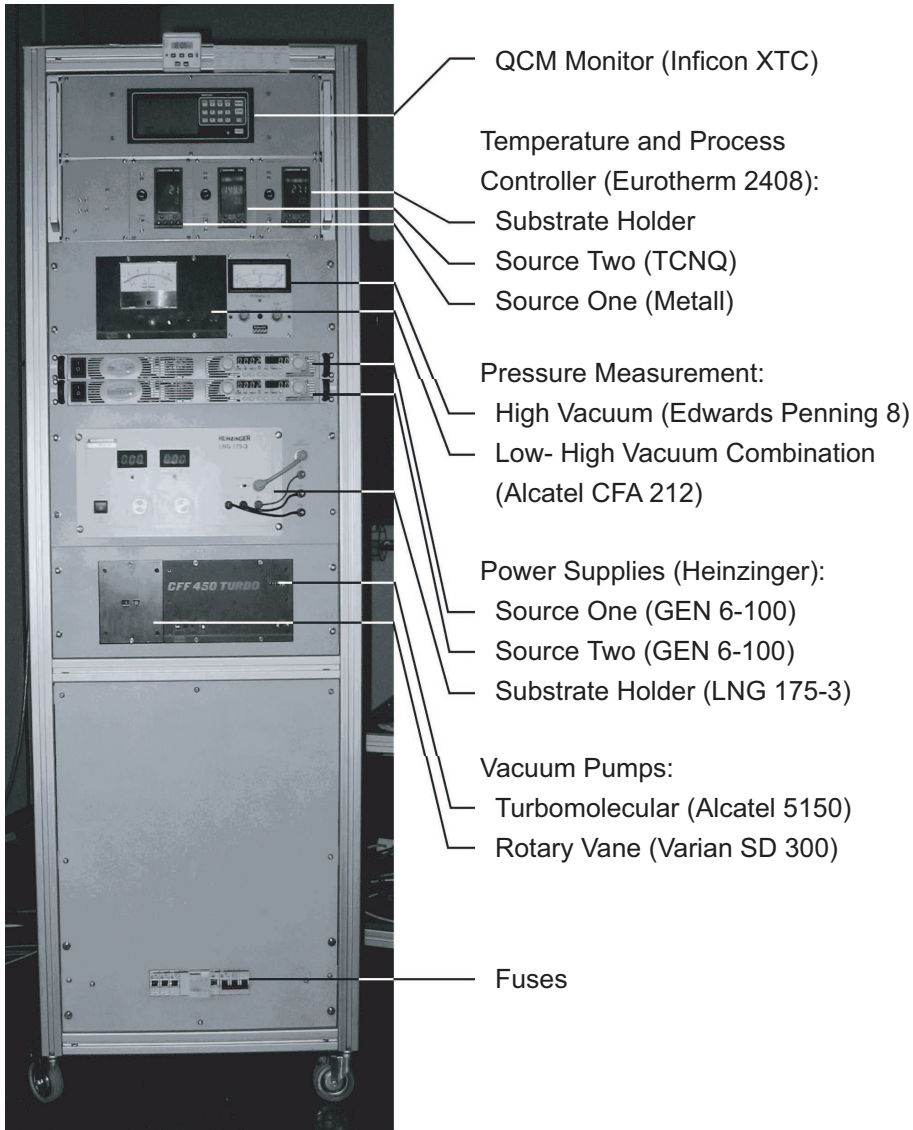


Figure 3.5: Control Elements of the vacuum chamber. Front view of the measurement cabinet.



Figure 3.6: *Manual shutter controls. Front view of the feedthroughs.*

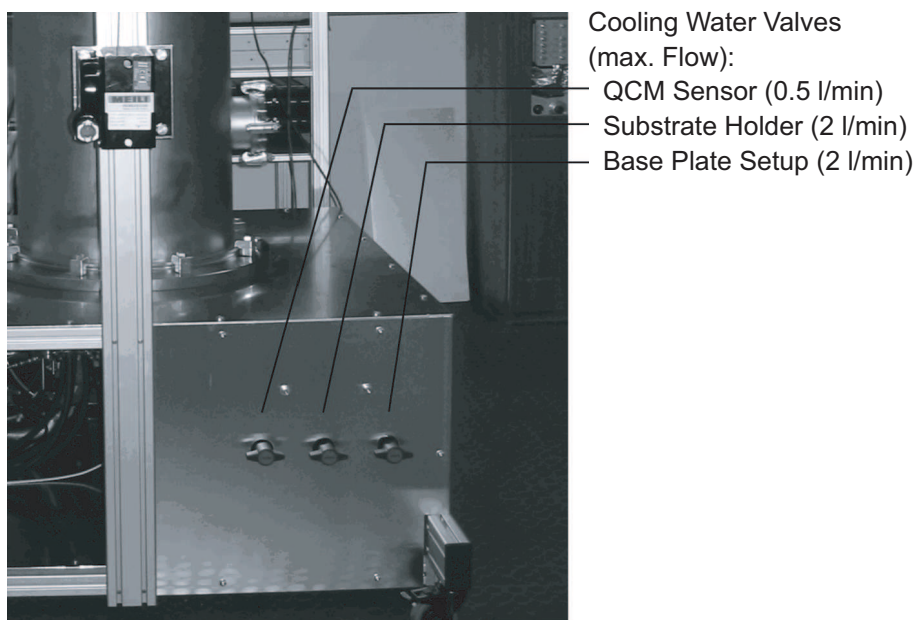


Figure 3.7: *Control of the cooling water flow. Valves and maximum flow rate.*

evaporation chamber and especially the connections to the PC are shown schematically in Fig. 3.8.

Cleaning of the Chamber

After some evaporation cycles, small amounts of TCNQ could be observed on most parts of the chamber. Therefore, the inside walls of the vacuum bell are covered by aluminum foil in order to avoid a deposition of material on the steel surface. Furthermore, a cleaning of the chamber is necessary at regular intervals due to the contamination with TCNQ and its decomposition products.

The regular cleaning process starts by the removing of the used aluminum foil. Next, a rough cleaning with diluted hydrochloric acid is performed. Afterwards, both sources are equipped with clean tungsten boats and the chamber is baked out using the heat radiation of the sources and the substrate holder. The power of these thermal sources is enough to heat up all parts of the chamber after some time (> 30 min). The temperatures in this case are high enough to evaporate the residual organic parts in the chamber. Little by little, the turbomolecular pump then removes these particles from the chamber. This process can be monitored using the QCM Sensor. After the bake out process, the inside of the vacuum bell is covered in new aluminum foil.

3.3 Development of the Deposition Processes

Two different PVD processes have been developed taking into account the possibilities and limitations of the evaporation chamber design described previously (3.2). In the following section, these two different concepts of successive (3.3.1) and simultaneous evaporation (3.3.3) are described in detail. In addition, the observed influence of an annealing step is reported (3.3.2).

Preparation of the Substrates and the Vacuum Chamber

The deposition in the evaporation chamber was carried out on substrate wafer pieces as described in section 3.2.3. These pieces, predominately 1 by 1 inch squares, were cut from either 6 inch oxidized silicon wafers or glass substrates using a Disco DAD 320 automatic dicing saw. Primarily, oxidized silicon wafers with a thin (10 nm), sputter deposited TiO_2 adhesion layer were used. A detailed description of the device setups is given in section 3.3.4.

Immediately before the use in the deposition process, the substrate pieces were subjected to a standardized cleaning process, independent of their type. This process can be broken down into the following steps:

- Cleaning in an ultrasonic bath of acetone (5 min)
- Cleaning in an ultrasonic bath of isopropanol (5 min)
- Drying with purged nitrogen
- Bake out on a hot plate at 400°C (5 min)

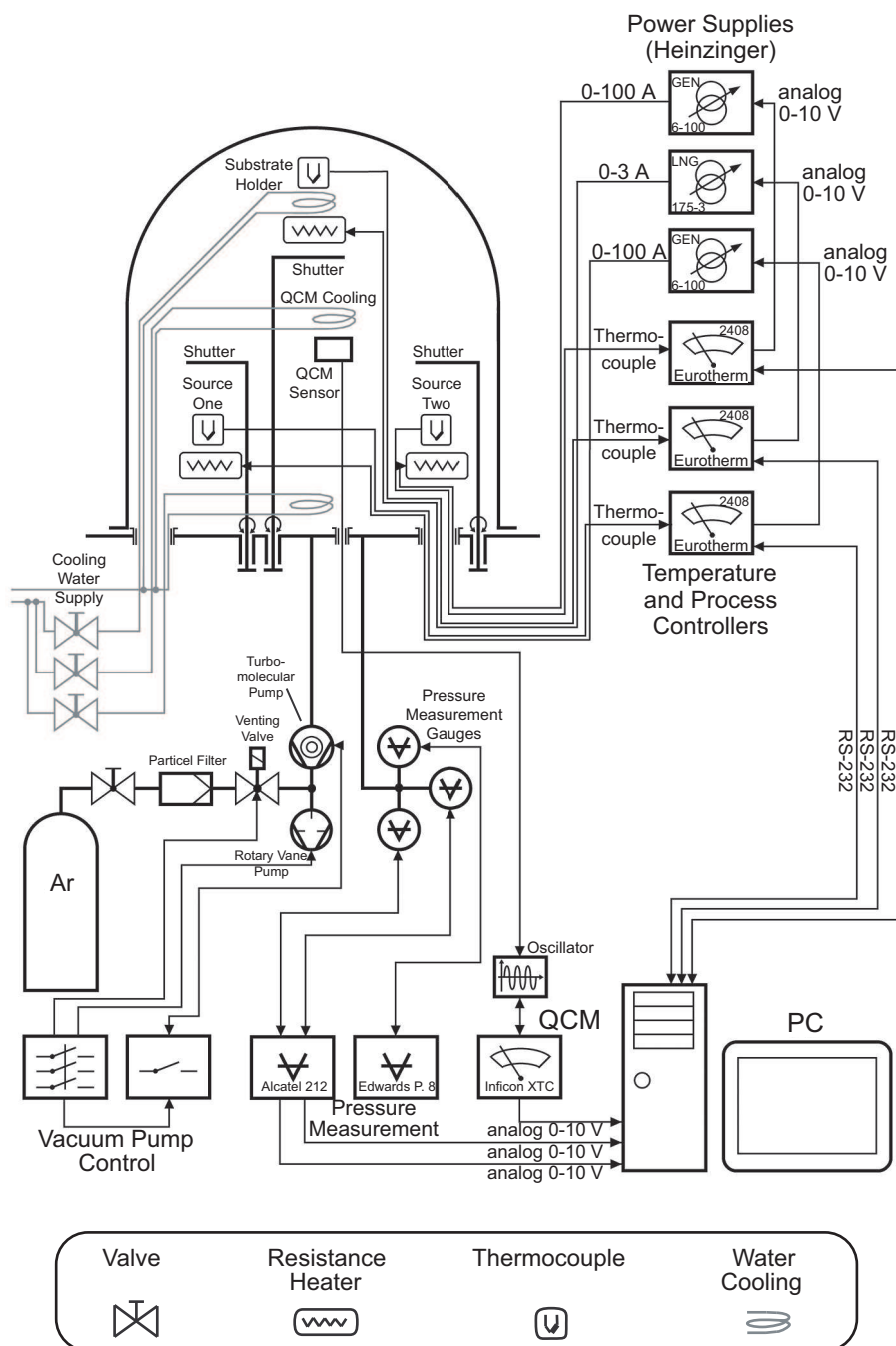


Figure 3.8: Schematic of the measurement and control circuits of the system.

Aim of these cleaning steps was the removal of dust and other detrimental particles adhering to the substrate surface.

Furthermore, a preparation of the vacuum chamber was necessary before the start of the actual processes. First, the status of the quartz crystal was checked, and the crystal, if necessary, replaced. In addition, this preparation included the replenishment of the evaporation sources. The tungsten boat (source one) was filled with Cu rods with a combined mass of ≈ 800 mg. The molybdenum boat (source two) was filled with ≈ 600 mg of TCNQ in crystalline form. These relatively large quantities of the two materials were observed to be critical in obtaining qualitatively good Cu:TCNQ thin films, especially for the simultaneous evaporation process (details are given in section 3.3.3). After refilling, both source shutters were closed. Finally, the substrate pieces were mounted to the substrate holder using one of the previously described plates (3.2.3). Then, the substrate shutter was closed and the vacuum bell lowered onto the Viton O-ring in order to seal the vacuum chamber.

3.3.1 Successive Evaporation Route

The preparation of Cu:TCNQ by PVD processes was the method of choice in this study, as described earlier (3.1). The first of the two developed PVD routes is composed of the subsequent in-situ deposition of a copper and a TCNQ layer. This process is called the successive evaporation route. Starting points for the establishment of this process were the very brief descriptions of the sample preparation by vapor deposition in some papers [59, 84, 93]. The principal process flow shown in Fig. 3.9 has emerged as ideal for the given setup during numerous experimental deposition cycles.

First, the above mentioned preparation of the substrate pieces and the vacuum chamber is carried out. After the chamber is sealed off, the Varian SD 300 dual-stage rotary vane pump is activated and the vacuum measuring system Alcatel CFA 212 is switched on. After a few minutes, the pressure within the chamber should have fallen below 1×10^{-1} mbar. Then, the Alcatel 5150 turbomolecular pump can be switched on in order to reach high vacuum pressures. During this pump down process, the substrate is baked out. For this, the Eurotherm 2408 which controls the substrate holders power supply (Heinzinger LNG 175-3), and collects feedback from the corresponding thermocouple, is set to a temperature of 200°C . It is necessary, to keep the substrate at least 10 min at this temperature to ensure a largely water free surface [95].

Meanwhile, the water flow for the cooling of the QCM sensor is turned on, and the material parameters for Cu (as stated in Table 3.3) are entered into the QCM controller. Furthermore, the source one (containing the Cu) is preheated to a temperature of $\approx 700^\circ\text{C}$, and the source two (containing the TCNQ) to 100°C , where in both cases no significant evaporation takes place at high vacuum pressures. In order to avoid a heating up of the base plate setup due to the thermal radiation, the water flow for the cooling of this setup is opened.

By the time the pressure has reached values of approximately 5×10^{-5} mbar and the bake out process is finished, the resistance heating of the substrate holder is switched off and the cooling water flow for this component is turned on. The actual evaporation can be started, when the temperature of the substrate holder has decreased to the temperature of the cooling water ($\approx 10^\circ\text{C}$). Then, the shutter of the Cu evaporation

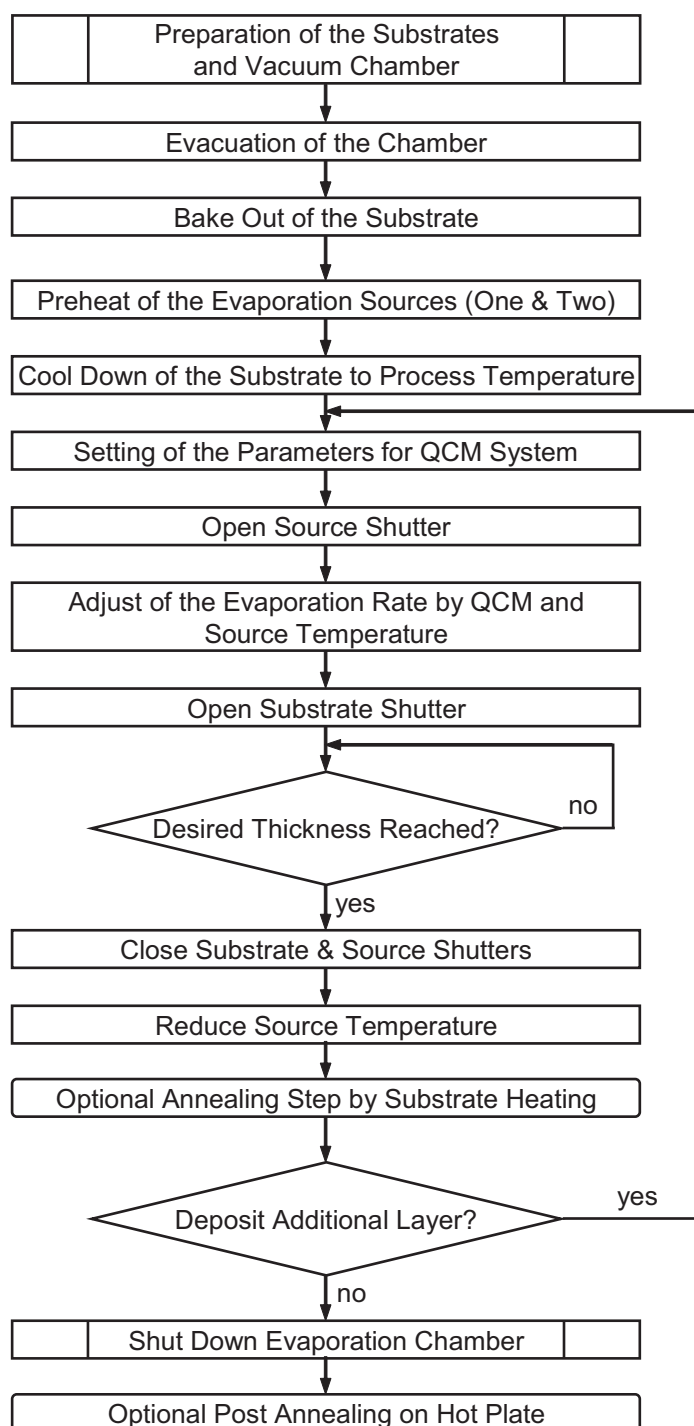


Figure 3.9: Flow chart for the successive evaporation process.

source is opened, and the temperature is increased using the coupled Eurotherm 2408 controller. The desired deposition rate is adjusted using the displayed values of the QCM system and the temperature control. In the case of this study, a deposition rate of 10 \AA/s was used for the deposition of the Cu layer. If the desired rate is reached and stable, the substrate shutter is opened and the Cu deposition on the sample begins. The temperature of the tungsten boat was roughly 1100°C for these settings, depending on the shape and the amount of Cu left in the boat. This evaporation is continued until the desired thickness is reached. Then, the substrate and source shutters are closed and the temperature of the source one is decreased. In the case of this study, the Cu thin films were 100 nm thick, which took roughly a deposition time of 100 s for the above mentioned parameters. The temperature of the source one is kept at 500°C during the remaining process steps, in order to prevent a possible deposition of TCNQ on the Cu source.

The deposition of the TCNQ layer is carried out analogous to the above described deposition of the Cu layer. First, the parameters for TCNQ (as stated in Table 3.3) are entered into the QCM controller. Then, the shutter of the TCNQ evaporation source is opened. Once more, the deposition rate is set using the QCM sensor and the Eurotherm controller of the source. Here, a deposition rate of 10 \AA/s was used for the TCNQ. If the desired rate is reached and stable, the substrate shutter is opened and the TCNQ deposition on the samples begins. The temperature of the molybdenum boat was roughly 145°C for this rate. By the time the desired TCNQ layer thickness is reached, the substrate and source shutters are closed.

Next, the power supplies for both sources are switched off. Then, it is possible to carry out the necessary annealing step for the formation of Cu:TCNQ under high vacuum conditions using the heater of the substrate holder. Optionally, the annealing step can be done later under atmospheric conditions using a hot plate. Detailed informations on the annealing step are given in section 3.3.2.

The cooling water flow of all components is turned off and the substrate holder is heated to room temperature. These steps are performed in order to avoid water condensation during the venting of the chamber. After the cooling down of the sources and the heating of the substrate, the vacuum pumps are switched off and the vacuum chamber is vented. The vacuum bell is lifted using the cable winch, and the samples are extracted from the substrate holder.

Successive Evaporation with a Seeding Layer

One of the different approaches, which were tested during the course of this study, was the deposition of a thin seeding layer prior to the TCNQ deposition. The process was similar to the above described up to the point, where the TCNQ evaporation starts. However, the temperature of the TCNQ source was kept lower at around 140°C , and therefore the deposition rate was distinctively lower ($\approx 2 \text{ \AA/s}$). Only a very thin TCNQ layer ($\approx 5 \text{ nm}$) was deposited. Afterwards, the process continued as explained before, until after the annealing step (whether carried out in the chamber or on an external hot plate). The remaining part of the TCNQ is then deposited on top of this Cu:TCNQ seeding layer. The formation of the Cu:TCNQ layer is triggered by a final annealing step.

However, the resulting Cu:TCNQ thin films prepared by the seeding layer method

Series @ 100 °C	Series @ 125 °C	Series @ 150 °C
30 s	0 s (pure TCNQ)	5 s
45 s	15 s	10 s
60 s	30 s	20 s
75 s	45 s	30 s

Table 3.4: *Annealing series parameters for successive deposited Cu:TCNQ.*

exhibited no noticeable difference in structure, morphology, and electrical behavior, when compared to samples prepared by the standard successive route. Therefore, this approach was not further pursued.

3.3.2 The Annealing Process

The standard successive evaporation route is explained in the previous section (3.3.1). However, this process initially results in a stacked structure of a TCNQ thin film on top of a Cu layer. A transport of Cu atoms via diffusion into the TCNQ layer is essential in the case of this layered structure of solids. Only then can the formation of the CT complex Cu:TCNQ occur by the direct oxidation reaction described in Eq. 2.1. While this corrosion reaction happens spontaneously using the electrolysis technique [14, 74, 75], a supply of energy in the case of solids is necessary in order to trigger the reaction. Potember et al. have shown that this reaction can be induced optically (by laser beam) [83]. Others demonstrated that the reaction also can be triggered by an electrical field [59].

In the case of this study, the diffusion as well as the oxidation reaction were activated by thermal heating. Exact parameters regarding the annealing process were not available and had to be determined by some experimental series.

Three experimental series were conducted at different temperatures. For these purposes, samples were prepared with a TCNQ thickness of 150 nm using the successive evaporation route, as described in section 3.3.1. These samples were then annealed on a hot plate under atmospheric conditions at three different temperatures. For each temperature, four different durations were tried. The parameters of these experimental series are summarized in Table 3.4.

The changes in the morphology of the thin films were examined by scanning electron microscopy with a Zeiss DSM 982 GEMINI at an acceleration voltage of 3 kV. The samples were broken and prepared with conductive silver for this analysis. In the following, the development of the annealing process is shown exemplary on the 125 °C series. In the case of pure TCNQ (0 s annealing), the layer displayed a yellowish-beige color with a matt appearance. The corresponding SEM images of a side (a) and a top view (b) are shown in Fig. 3.10. The TCNQ layer has a typical structure consisting of a granular structure with grain sizes of ≈ 400 nm. A couple of grains at a time form insular areas, which are separated only by slender rifts. These areas are separated from each other by deep trenches.

After 15 s of annealing at 125 °C, no change of appearance was visible to the naked eye. The corresponding SEM images of a side (a) and a top view (b) are shown in

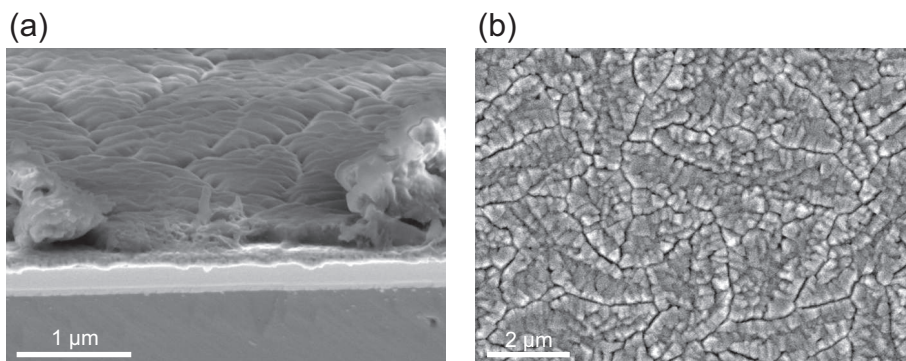


Figure 3.10: SEM images of the successive annealing series (0 s @ 125 °C). Side (a) and top view (b) of the pure TCNQ layer (thickness 150 nm) on top of a Cu layer.

Fig. 3.11. Also, no structural changes compared to the pure TCNQ can be observed on these images.

During the 30 s annealing step at 125 °C, a change of appearance could be observed. The reflectivity of the sample gradually changed to a more glossy appearance. Furthermore, the color transformed from the yellowish-beige starting point gradually to gray and finally to a dark green. The corresponding SEM images of a side (a) and a top view (b) are shown in Fig. 3.12. Numerous, needle shaped columns of Cu:TCNQ can be observed in the side view (a), which are obviously grown out of the, still partly intact, TCNQ layer. The grain like structure is still visible. The top view (b) reveals, that the growth of those Cu:TCNQ needles is favored at/next to the trenches between the TCNQ grains. The tips of the needles can be seen as the bright spots in the image. This observation gives raise to the thought, that the diffusion of the Cu occurs not uniformly, but takes place preferably at the grain boundaries.

During the 45 s annealing step at 125 °C, the change of appearance is even more

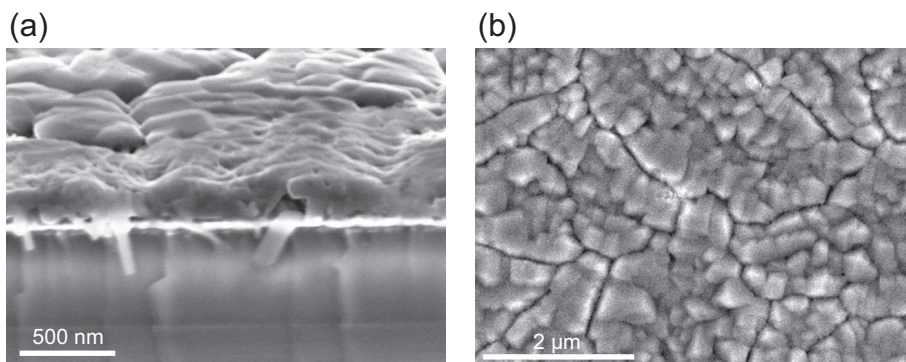


Figure 3.11: SEM images of the successive annealing series (15 s @ 125 °C). Side (a) and top view (b) of the partially annealed TCNQ layer (thickness 150 nm) on top of a Cu layer.

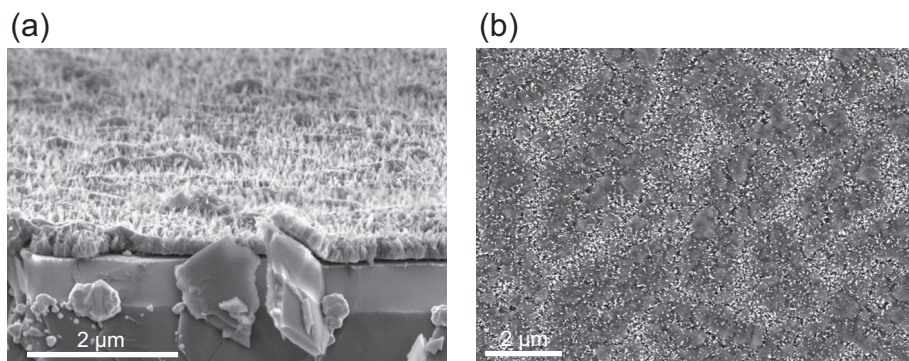


Figure 3.12: SEM images of the successive annealing series (30 s @ 125 °C). Side (a) and top view (b) of the partially annealed TCNQ layer (thickness 150 nm) on top of a Cu layer.

pronounced. In this case, the reflectivity of the sample gradually changed to a complete glossy appearance, and the color is transformed to dark green. The corresponding SEM images of a side (a) and a top view (b) are shown in Fig. 3.13. The formerly continuous TCNQ layer is no longer existent. Instead, even more of the needle shaped columns of Cu:TCNQ have been formed, as shown in the side view (a). These columns have a diameter of ≈ 50 nm and a length of up to 400 nm. The top view (b) shows no longer a grain like structure, but instead an evenly distribution of the Cu:TCNQ nanowires. It can be concluded from these results, that the transformation of TCNQ to Cu:TCNQ is completed entirely after 45 s of annealing at 125 °C.

The samples annealed at the lower temperature of 100 °C in contrast, exhibited only a marginal transformation of TCNQ to Cu:TCNQ even after 75 s. The side view of this sample is shown in Fig. 3.14 (a). Cu:TCNQ needles can be seen only very sporadic. For shorter annealing times, no change at all compared to the pure TCNQ sample could be observed.

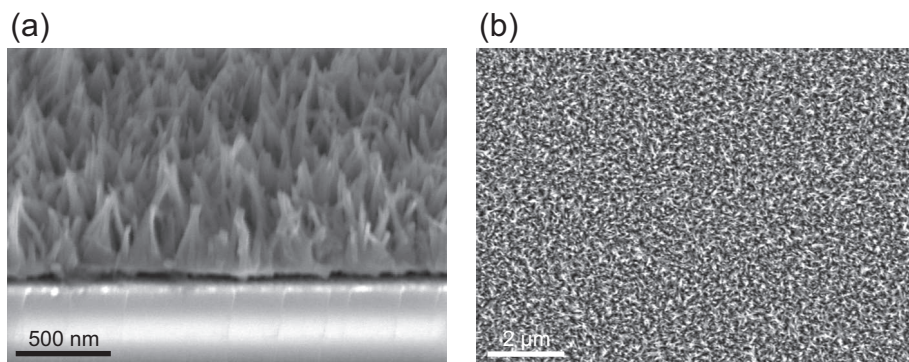


Figure 3.13: SEM images of the successive annealing series (45 s @ 125 °C). Side (a) and top view (b) of the completely annealed TCNQ layer (thickness 150 nm) on top of a Cu layer.

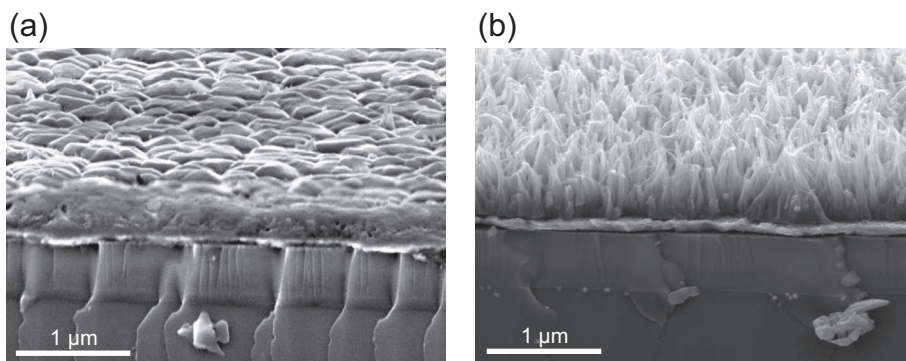


Figure 3.14: SEM images of the successive annealing series @ 100 °C and 150 °C. Side view (a) of a sample which was annealed for 75 s @ 100 °C, and side view (b) of sample which was annealed for 10 s @ 150 °C.

The samples annealed at the highest temperature of 150 °C displayed a fast transformation of TCNQ to Cu:TCNQ. Even for the shortest tested amount of time of 5 s, the transformation was further completed as it was the case of the samples annealed for 30 s @ 125 °C. The side view of a sample annealed for 10 s @ 150 °C is shown in Fig. 3.14 (b). For longer annealing times, no additional change could be observed. Therefore, it can be concluded, that no further morphological change occurs after the columnar Cu:TCNQ growths in the studied temperatures range.

Additional experiments were conducted, in order to evaluate a possible influence of the ambient conditions on the annealing process. Therefore, samples were annealed in-situ using the substrate holder heater system and compared to the above presented results of the ex-situ hot plate annealing process. No distinctive difference in the morphology could be observed for both cases. A similar growth of Cu:TCNQ nanowires could be observed as shown in Fig. 3.15. The annealing temperature was 125 °C while the duration was longer, ≈ 5 min in case (a), and ≈ 10 min in case (b) due to the slow heating rate of the substrate holder.

Further experiments were carried out, in which the influence of an increased substrate temperature during the TCNQ deposition was studied. Thereby it showed, that at elevated temperatures (> 110 °C) the deposition rate decreased due to an increasing back-evaporation of TCNQ from the substrate. A SEM image of a sample which was kept at a temperature of 115 °C during the deposition process is shown in Fig. 3.16 (a). In this case the deposition rate was deliberately kept low at a rate of 3 \AA/s . This low deposition rate in combination with the elevated substrate temperature resulted in a more compact and denser Cu:TCNQ layer. However, there were still unreacted TCNQ remains on the substrate. Therefore, an additional in-situ annealing step was carried out after the deposition at a temperature of 125 °C for ≈ 10 min as shown in Fig. 3.16 (b). It showed, that the resulting Cu:TCNQ layer again displayed the typical needle like structure, however less pronounced.

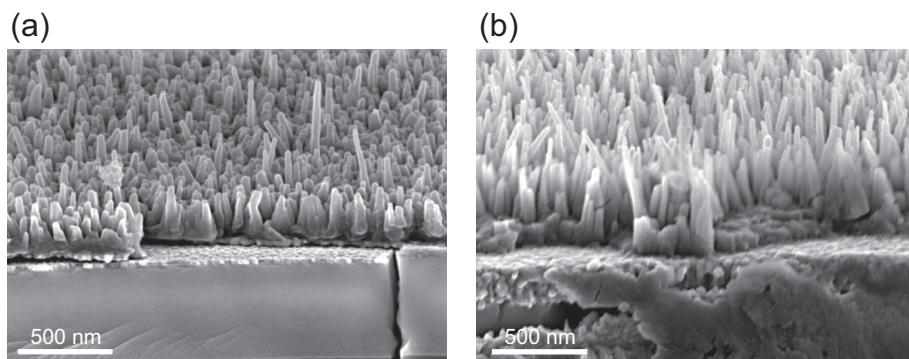


Figure 3.15: SEM images of in-situ annealed samples of successive evaporated TCNQ layers. Side view of a sample which was annealed in-situ at 125 °C for ≈ 5 min (a), and for ≈ 10 min (b) .

3.3.3 Simultaneous Evaporation Route

The preparation of Cu:TCNQ by the above-described successive PVD route (3.3.1) with a subsequent annealing step (3.3.2) resulted in very rough Cu:TCNQ layers, even after detailed process optimizations. Furthermore, the nature of the successive process requires the use of Cu as the bottom electrode. Therefore, a second PVD route was developed in order to fabricate homogeneous and dense Cu:TCNQ thin films, which can also be deposited on different electrode materials besides Cu. This process is composed of the simultaneous in-situ deposition of Cu and TCNQ together. Both compounds, the metallic donor Cu and the organic acceptor TCNQ, are mixed in the gas phase prior to the deposition on the substrate as shown schematically in Fig. 3.17. This process is called the simultaneous evaporation route and has been published in [98].

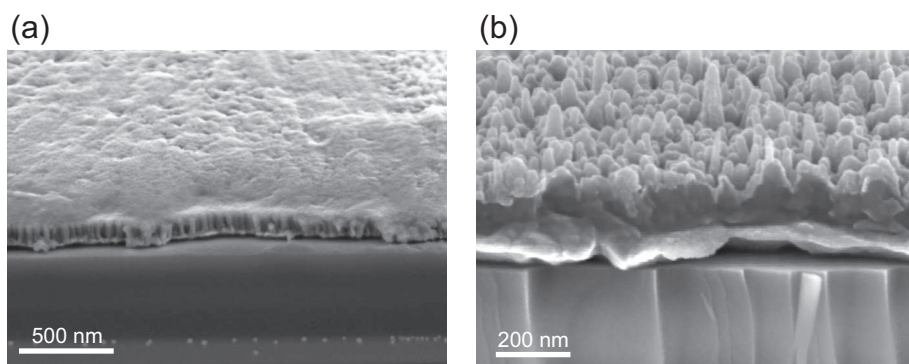


Figure 3.16: SEM images of successive deposited samples at elevated temperatures. Side view of a sample which was kept at 115 °C during deposition with a slow rate of 3 Å/s (a). Side view of a sample which was afterwards annealed in-situ for ≈ 10 min @ 125 °C, in order to ensure a complete transformation to Cu:TCNQ (b).

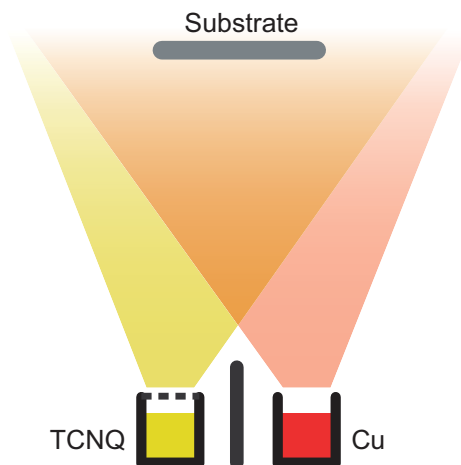


Figure 3.17: Schematic of the gas phase mixing during the simultaneous process.

Starting point for the establishment of this process was the brief demonstration of the feasibility of such a process by Oyamada et al. [81]. During numerous experimental deposition cycles, the principal process flow shown in Fig. 3.18 has emerged as ideal for the given setup.

The simultaneous evaporation process starts with the preparation of the substrate pieces and the vacuum chamber as described in section 3.3. Next, the vacuum chamber is evacuated and the substrate is baked out in order to ensure a largely water free surface. Then, the evaporation sources are preheated, the QCM system is prepared, and the cooling water supply for the base plate setup is switched on. These steps are identical with the ones at the beginning of the successive evaporation process and are described there (3.3.1) in more detail.

By the time the pressure has reached values of approximately 5×10^{-5} mbar and the bake out process is finished, the resistance heating of the substrate holder is set to the desired process temperature. The necessary cool down is accelerated using a temporary cooling water flow through the substrate holder. The temperature of the source one is then momentarily raised above the melting point of Cu (1084.4 °C). This results in a stable Cu surface in the boat, which later on leads to a more constant evaporation rate of Cu for low temperatures (below melting point). Then, the shutter of the Cu evaporation source is opened, and the temperature is increased using the coupled Eurotherm 2408 controller. The desired deposition rate is adjusted using the displayed values of the QCM system and the temperature control. In the case of this study, a deposition rate of 0.5 Å/s was normally used for the co-deposition, and a rate of 0.25 Å/s for very thin layers. The temperature of the tungsten boat was roughly 950 °C for these settings, depending on the shape and the amount of Cu left in the boat. If the desired rate is reached and stable, the shutter of this source is closed.

Next, the parameters for TCNQ (as stated in Table 3.3) are entered into the QCM controller. Then, the shutter of the TCNQ evaporation source is opened. Again, the deposition rate is set by using the QCM sensor and the Eurotherm controller of the source. The necessary TCNQ deposition rate for a particle ratio of 1:1 for Cu:TCNQ

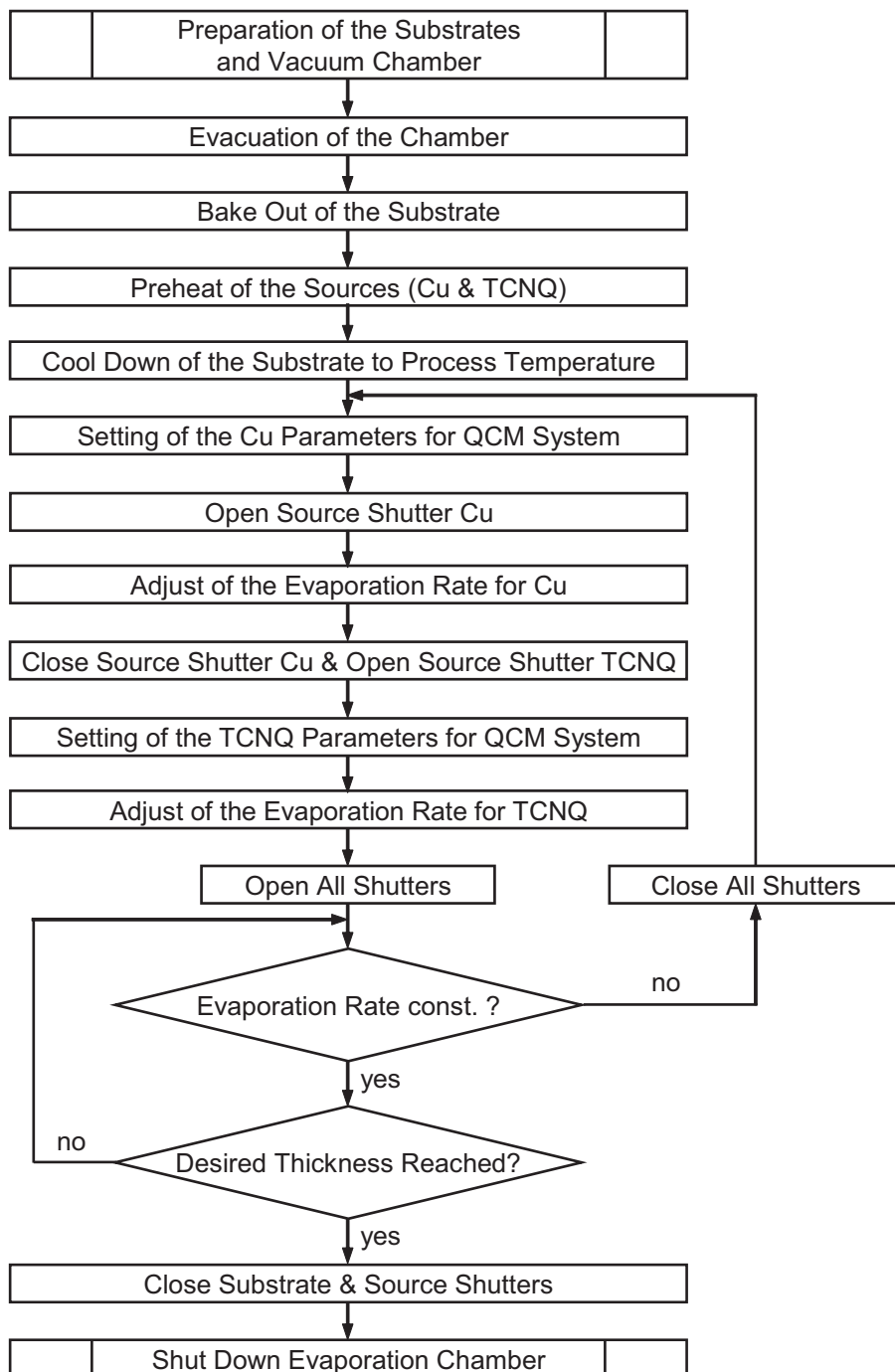


Figure 3.18: Flow chart for the simultaneous evaporation process.

can be calculated using the densities ρ and atomic, respectively molecular masses m_u :

$$\begin{aligned}
 \rho_{Cu} &= 8.93 \frac{\text{g}}{\text{cm}^3} \\
 m_{\text{grams},Cu} &= \frac{m_{u,Cu}}{N_A} = 63.55 \frac{\text{g}}{\text{mol}} \\
 \Rightarrow \frac{\rho_{Cu}}{m_{\text{grams},Cu}} &= 6.66 \times 10^{-3} \frac{\text{mol}}{\text{cm}^3} \\
 \rho_{TCNQ} &= 1.36 \frac{\text{g}}{\text{cm}^3} \\
 m_{\text{grams},TCNQ} &= \frac{m_{u,TCNQ}}{N_A} = 204.19 \frac{\text{g}}{\text{mol}} \\
 \Rightarrow \frac{\rho_{TCNQ}}{m_{\text{grams},TCNQ}} &= 0.1405 \frac{\text{mol}}{\text{cm}^3}
 \end{aligned}$$

Using these molecular volumes, the ratio for the deposition rates of the two compounds can be calculated.

$$\frac{\text{deposition rate TCNQ}}{\text{deposition rate Cu}} = 21.1 \quad (3.3)$$

Therefore, a TCNQ deposition rate of 10.5 Å/s is necessary for a Cu rate of 0.5 Å/s, and a TCNQ rate 5.3 Å/s for the lower Cu rate (0.25 Å/s) for very thin films.

The temperature of the molybdenum boat was roughly 145 °C for this rate. The experiments demonstrated, that the TCNQ deposition rate was more stable if the temperature of the TCNQ source was beforehand increased to at least 160 °C. This results in a conglomeration of the TCNQ salt crystals, and therefore to a more constant surface from which the evaporation takes place.

If the desired rate is reached and stable, the source two shutter is closed and the Cu evaporation rate is verified. If the Cu rate is still constant at the appropriate value, both source shutters are opened, otherwise the temperature of the source one must be adjusted. After a few seconds, the substrate shutter is opened and the deposition begins at a combined rate of 14 Å/s. The deposition is continued until the desired thickness is reached or the evaporation rate becomes unstable. In the latter case, the substrate shutter is closed and both sources are adjusted in their temperatures and rates individually, before the deposition process is continued.

By the time the desired Cu:TCNQ layer thickness is reached, the substrate and source shutters are closed. Next, the power supplies for both sources are switched off. The cooling water flow of all components is turned off. This step is performed in order to avoid water condensation during the venting of the chamber. After the cooling down of the sources and the substrate, the vacuum pumps are switched off and the vacuum chamber is vented. The vacuum bell is lifted using the cable winch, and the samples are extracted from the substrate holder.

Evaporation Rate Conversion

In the above-described simultaneous evaporation process, it is necessary to measure the alternating evaporation rates of Cu and TCNQ during the adjustment. Since there is only one QCM system installed in the vacuum chamber, the parameters must be

Temperature	15 °C	50 °C	75 °C	100 °C	125 °C
Thickness	90 nm	91 nm	93 nm	71 nm	61 nm

Table 3.5: Substrate temperature series for the simultaneous deposition. Studied temperature range and the resulting thicknesses measured by SEM.

changed accordingly. These additional, time consuming steps can be avoided by using the possible conversion of the parameters. The deposition rate r_{dep} can be calculated using Eq. 3.4, where d represents the thickness of the layer, respectively the quartz crystal.

$$r_{dep} = \frac{d}{dt} d_{layer} = d_{QC} \frac{\rho_{QC}}{\rho_{layer}} \frac{d}{dt} \frac{\Delta f}{f_{QC}} \quad (3.4)$$

This equation can be transformed and simplified to a term, which linearly relates the deposition rates with the quotient of the densities as a constant factor:

$$\frac{r_{dep,\rho1}}{r_{dep,\rho2}} = \frac{\rho2}{\rho1} \Leftrightarrow r_{dep,\rho2} = \frac{\rho1}{\rho2} r_{dep,\rho1} \quad (3.5)$$

With this relation it is possible to convert a deposition rate to a different density value. In this case, the evaporation of Cu with a density of $\rho_{Cu} = 8.93 \text{ g/cm}^3$, while using the parameters of TCNQ in the QCM system ($\rho_{TCNQ} = 1.36 \text{ g/cm}^3$), results in a conversion factor of 6.57. Therefore, a Cu evaporation rate of 0.5 Å/s for example would be equal to a displayed rate of 3.3 Å/s for TCNQ parameters.

Influence of the Substrate Temperature on the Simultaneous Process

In contrast to the successive evaporation route, an additional annealing step was found to be unnecessary in the case of the simultaneous process. The resulting layer already consists of the CT complex Cu:TCNQ as it is being deposited. This is shown in detail in section 4.1.1.

However, a possible influence of the substrate temperature during deposition on the layer morphology was studied. For these purposes, a substrate temperature series was prepared using the simultaneous route. Five different temperatures were tested, 15 °C, 50 °C, 75 °C, 100 °C, and 125 °C. According to the QCM system, the thickness of Cu:TCNQ was the same on all samples. However, as already mentioned earlier in section 3.3.2, a decrease of the deposition rate can be observed with increasing substrate temperature as shown in Table 3.5.

The changes in the morphology of the resulting thin films were examined by scanning electron microscopy. The study showed, that the influence of the substrate temperature within the examined range in general was small. Two examples of resulting Cu:TCNQ layers are shown in Fig. 3.19. These thin films are considerably more densely packed and uniform with a greatly reduced surface roughness independent of the substrate temperature, compared to successive deposited films. The Cu:TCNQ layers prepared at a substrate temperature of 75 °C and 100 °C (Fig. 3.19 (b)) displayed a somewhat better quality than the ones deposited at the lower temperatures of 15 °C (Fig. 3.19 (a)) and 50 °C. At even higher temperatures (125 °C), the quality deteriorated.

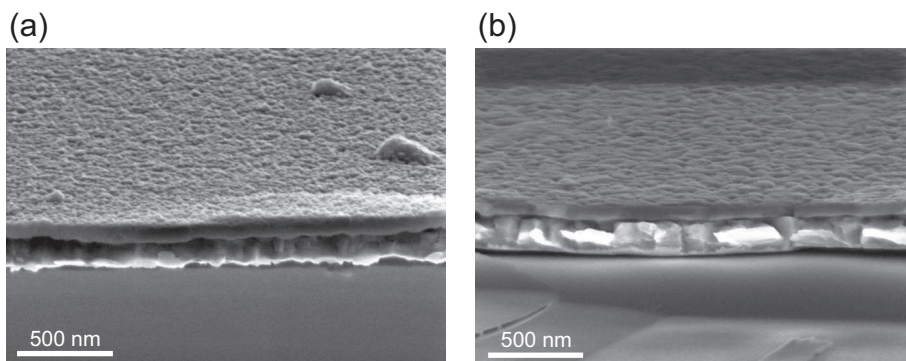


Figure 3.19: SEM images of simultaneous deposited samples. Side view of a sample which was kept at a substrate temperature of 15 °C (a), and one kept at 100 °C (b) during the deposition process.

Thickness Series of Simultaneous Evaporated Cu:TCNQ

A thickness series of Cu:TCNQ thin films was prepared using the simultaneous evaporation process described above. This was done in order to determine the minimum possible thickness at which the layer was still cohesive. The morphology and thickness of the Cu:TCNQ layers were observed by SEM.

Densely packed and uniform Cu:TCNQ layers without visible holes or trenches could be achieved down to a thickness of 25 nm. SEM images of the side views of Cu:TCNQ thin films with thicknesses between 25 nm and 138 nm are shown in Fig. 3.20. In this range, they display comparable morphologies and characteristics, independent of their thickness.

3.3.4 Device Setup

The completed devices, which were used for the electrical and physical characterization can be described as simple, capacitor like structures. The sample setup consists of a continuous bottom electrode, a continuous Cu:TCNQ layer, and a pad size top electrode.

Most of the substrates used for the sample preparation in the course of this thesis, were oxidized silicon wafer pieces with the dimensions of 1 by 1 inch. Some comparison samples were prepared on glass substrates. The pieces were cut from either 6 inch silicon wafers or glass substrates using a Disco DAD 320 automatic dicing saw. Before the dicing process, the surface of the silicon wafers were oxidized using a diffusion furnace system. This process resulted in a 450 nm SiO₂ layer. A 10 nm thin Ti layer was sputtered on top of this film. The Ti was then oxidized to TiO₂ and was used as an adhesion layer for the bottom electrode.

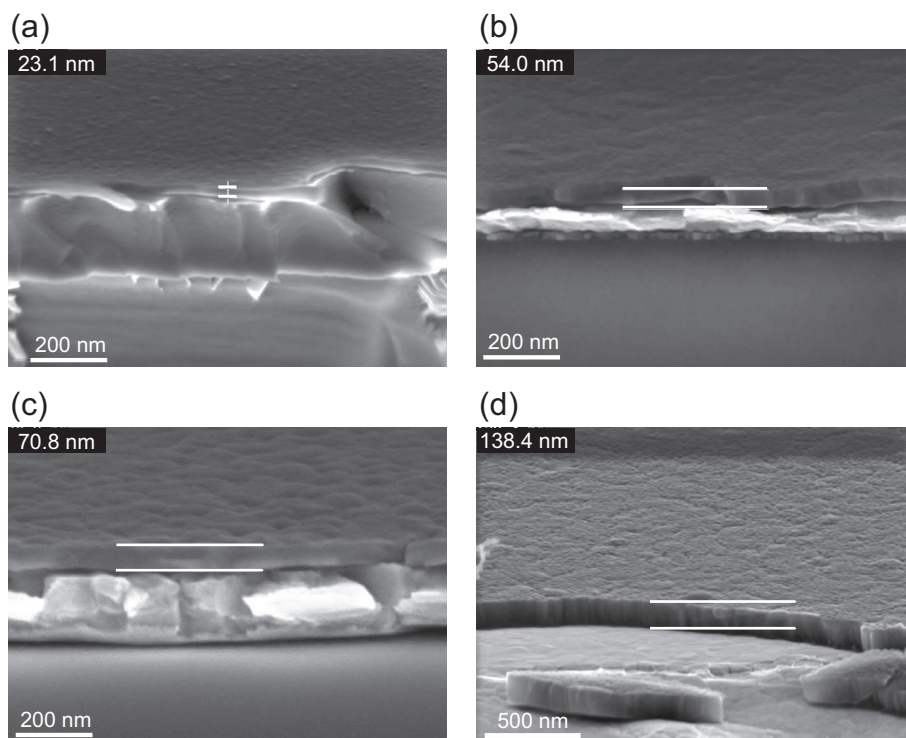


Figure 3.20: SEM images of thickness series of simultaneous deposited samples. Side views of Cu:TCNQ layers with a thickness of (a) 23 nm, (b) 54 nm, (c) 71 nm, and (d) 138 nm.

Successive Evaporation Process

In case of the successive evaporation process, the bottom electrode material has to be Cu, as described in section 3.3.1. Therefore, a continuous Cu layer was in-situ, thermally deposited with a typical thickness of 100 nm. In some cases, ex-situ deposited Cu was used. Then, an additional etching step with acetic acid was necessary in order to remove the naturally formed oxide layer. The TCNQ layer was deposited on top of the Cu bottom electrode. After an annealing step, the top electrode was deposited on the Cu:TCNQ layer through a shadow mask. The typical device setup for the successive evaporation route is shown in Fig. 3.21.

One problem of this process was the extremely rough Cu:TCNQ surface consisting mainly of needle shaped columns as shown in section 3.3.2. These resulted in rough and sometimes (especially for thin top electrodes) discontinuous top electrode pads. An example for a 100 nm thick Al top electrode is shown in Fig. 3.22 (a). The Al displays a very rough and granular surface in this case.

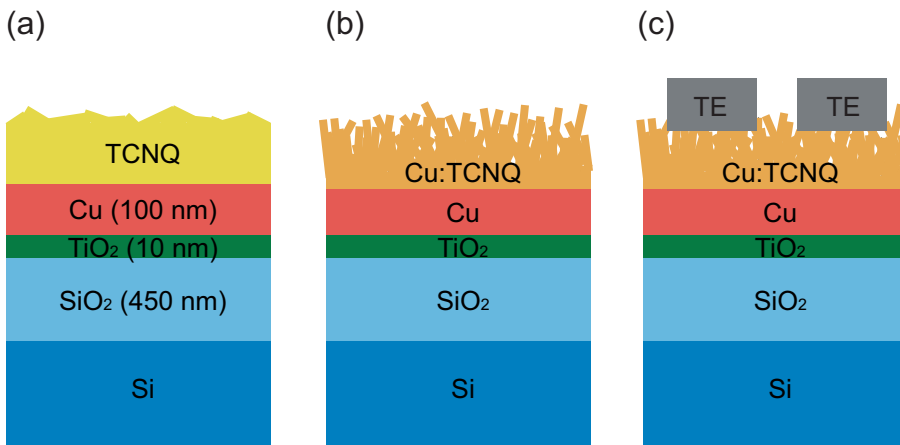


Figure 3.21: Typical device setup for the successive evaporation process. Device prior to the annealing step (a), after the annealing (b), and after the top electrode deposition through a shadow mask (c).

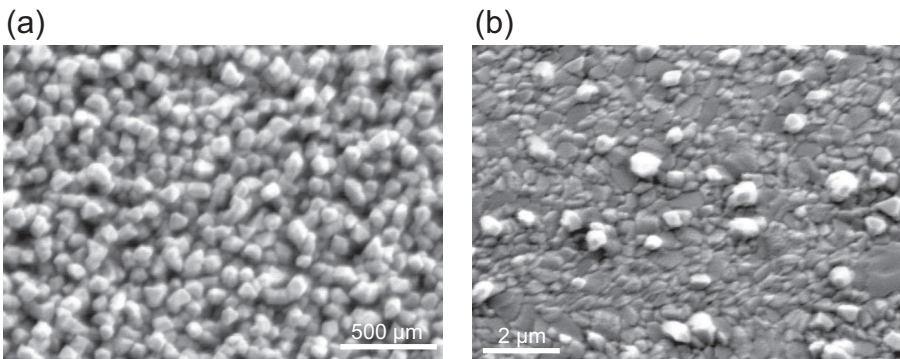


Figure 3.22: SEM images of Al top electrodes on Cu:TCNQ. Top views of 100 nm thick Al layer on top of a successive (a), and a simultaneous evaporated (b) Cu:TCNQ layer.

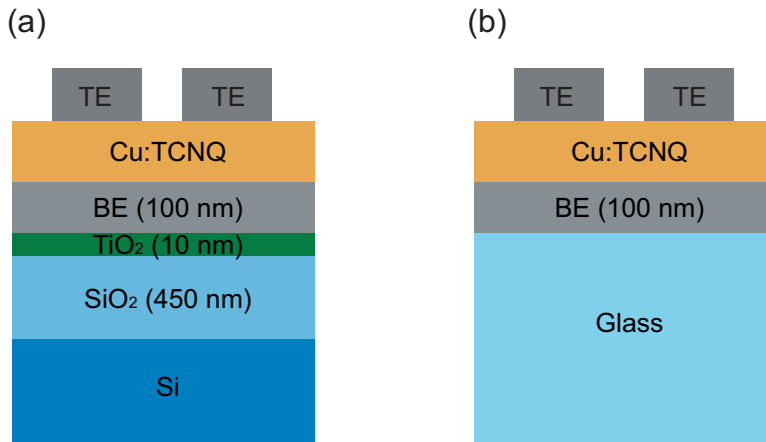


Figure 3.23: Typical device setup for the simultaneous evaporation process. Silicon substrate based device (a), and glass substrate based device (b).

Simultaneous Evaporation Process

In case of the simultaneous evaporation process, the bottom electrode material could be chosen freely, as described in section 3.3.3. Therefore, a continuous layer of the respective material was deposited ex-situ with a typical thickness of 100 nm. If necessary, an additional etching step was used to remove a naturally formed oxide layer. The Cu:TCNQ layer was then deposited on top of the continuous bottom electrode. Finally, the top electrode was deposited on the Cu:TCNQ layer through a shadow mask. The typical device setup for the simultaneous evaporation route is shown in Fig. 3.23.

The top electrodes displayed a more homogeneous and continuous structure, when compared to the rough and sometimes (especially for thin top electrodes) discontinuous top electrodes of the successive samples. The difference in the morphology for a 100 nm thick Al top electrodes is shown in Fig. 3.22. The Al displays a much smoother and cohesive surface, despite some individual, outside lying grains for the simultaneous evaporated Cu:TCNQ (Fig. 3.22 (b)).

Top Electrode Shadow Mask

The top electrode was structured using shadow masks. These masks are made of Ni foils with a thickness of 10 μm and circular openings. These openings have diameters between 75 μm and 1000 μm , which resulted in the top electrode areas shown in Tab. 3.6.

Diameter d	75 μm	150 μm	225 μm	500 μm	1000 μm
Area A	0.0044 mm ²	0.0177 mm ²	0.0398 mm ²	0.1963 mm ²	0.7854 mm ²

Table 3.6: Pad diameters and areas of the top electrode. Top electrode is deposited through a shadow mask with circular openings.

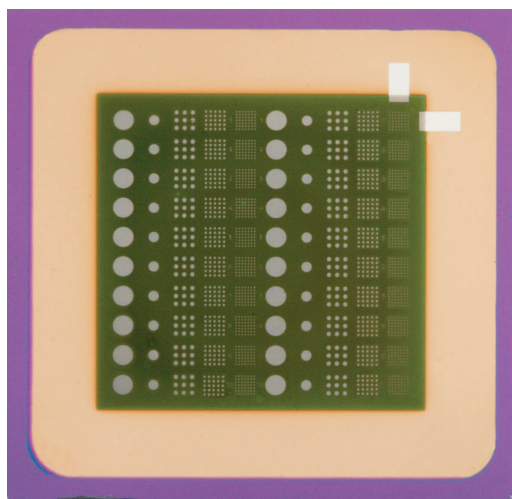


Figure 3.24: Top view of a device with a top electrode structured by a shadow mask. The device is based on a silicon wafer piece with Cu bottom electrode, successive evaporated Cu:TCNQ layer, and Al top electrode.

A photograph of the top view of a successive evaporated Cu:TCNQ sample is shown in Fig. 3.24. In this case, the top electrode consists of a 100 nm thick Al layer, which was thermally deposited through the above described shadow mask. The Cu bottom electrode and the Cu:TCNQ layer both had a thickness of 100 nm. The substrate was a 1 by 1 inch oxidized silicon wafer piece with a TiO_2 adhesion layer.

Structuring of Cu:TCNQ

Experiments regarding the compatibility of Cu:TCNQ to standard structuring methods were conducted in order to evaluate a possible preparation of more sophisticated device setups. The experiments were based on standard photolithography processes. Different photoresist types (AZ 4562, AZ nLOF, AZ 5214E, TI xLift) of the vendor MicroChemicals were spin coated on top of the Cu:TCNQ layer. Subsequently the exposure and the developing step with different developer types (MicroChemicals AZ Dev. and AZ 826 MIF) followed. The resulting pattern was then etched, either wet-chemical with 37 % hydrochloric acid or by reactive ion etching (RIE) technique. The wet-chemical process resulted in severe undercutting as shown in Fig. 3.25. This demonstrated the high anisotropic etch rates appearing in Cu:TCNQ.

The use of RIE techniques resulted in a much more isotropic etching. However, difficulties emerged during the photoresist removal process. The photoresist attached to the Cu:TCNQ layer in a manner that parts of the Cu:TCNQ were also peeled off during the removal process. Therefore, at least small holes appeared in the Cu:TCNQ, as shown in comparison to a virgin layer in Fig. 3.26. No working devices could be prepared by this method due to an electrically shortening caused by these holes.

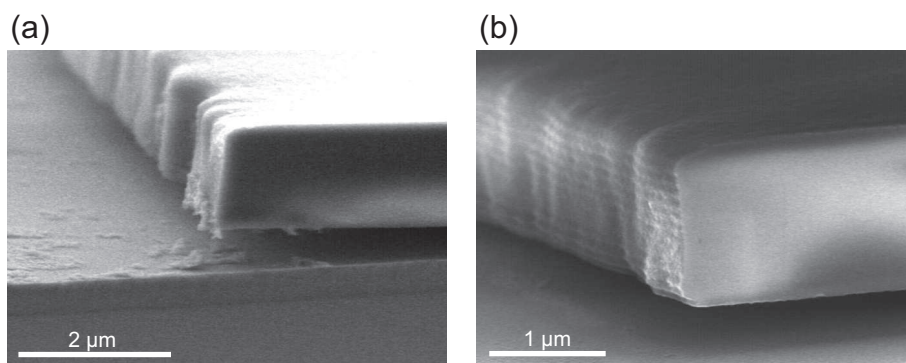


Figure 3.25: SEM images of wet-chemical etching of Cu:TCNQ. Side views of the undercutting of the photoresist layer (a), and close-up view (b).

Crossbar Array

While the measurements and experiments described in the later chapters (4 & 5) were conducted on the above-described simple pad-size devices, some experiments were carried out regarding a possible implementation in a crossbar array. A schematic of the aimed for structure is shown in Fig. 3.27 (a). The electrodes are structured into lines of different width with contact pads at the start and end. The bottom and top electrodes are distorted against each other by 90° as shown in Fig. 3.27 (b). The electrodes were structured by means of photolithography and etched by a RIE process. The resulting devices displayed no resistive switching, but rather either short circuits or open connections. Further experiments are necessary in order to enhance the process parameters.

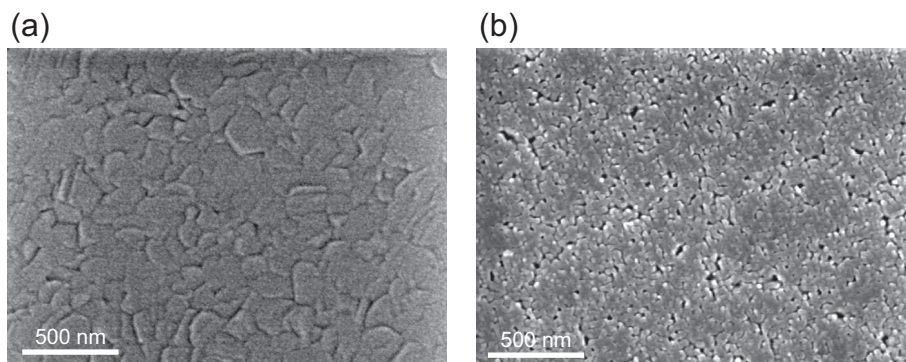


Figure 3.26: SEM images of the surface of simultaneous evaporated Cu:TCNQ. Typical morphology of a 100 nm thick layer (a), and comparable layer after photoresist deposition and removal processes.

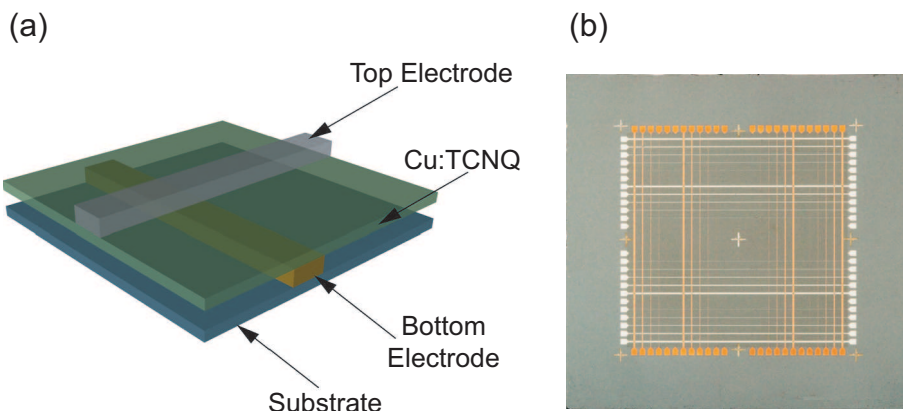


Figure 3.27: Crossbar device structure. Schematic of a single crosspoint (a), and image of a prepared device with Cu bottom and Al top electrode.

3.4 Summary

The construction of a high vacuum evaporation chamber for Cu:TCNQ thin films is described in this chapter. The designed system consists basically of two independent thermal evaporation sources, one for Cu and other electrode metals and one for organic material (TCNQ). These sources were set up to be operated simultaneously or separately, controlled by a shutter system. The temperature control of the sources and the substrate is carried out semi-automatic via thermocouples which are connected to process controllers. These controllers in turn regulate the resistance heater power supplies. A control of the evaporation rates was made possible by the use of a QCM measuring unit.

Furthermore, the development of two different deposition routes was described. Samples prepared by the successive method required the usage of a Cu bottom electrode and the execution of an annealing step in order to form the CT complex Cu:TCNQ. The resulting thin films displayed a very rough structure consisting of long columns oriented perpendicular to the substrate surface. On the other hand, samples prepared by the simultaneous method allowed the usage of different bottom electrode materials and did not require an annealing step. The resulting thin films displayed a considerably more densely packed and uniform structure with a greatly reduced surface roughness [98].

In addition, the typical device structure used for the later described electrical characterization was introduced. These devices can be described as simple, capacitor like structures. The sample setup consists of a continuous bottom electrode, a continuous Cu:TCNQ layer, and pad size top electrodes.

4 Characterization

The basic characterization of the Cu:TCNQ thin film devices, which were prepared by either the successive or simultaneous deposition method, is described in this chapter. The preparation of the analyzed samples was carried out using the constructed evaporation chamber and developed processes, as described in chapter 3. In the process, samples without top electrodes were used for the physical characterization (spectroscopy, XRD), and simple, capacitor like devices with pad size top electrodes (as described in 3.3.4) were used for the electrical characterization.

4.1 Physical Characterization

4.1.1 UV–Vis Spectroscopy

Ultraviolet–visible spectroscopy (UV–Vis) is the spectroscopy of photons in the visible and adjacent near ultraviolet and near infrared range of the spectrum. In this region of energy space, molecules undergo electronic transitions. Therefore, UV–Vis spectroscopy is routinely used in the quantitative determination of solutions of transition metal ions and highly conjugated organic compounds. Organic compounds, especially those with a high degree of conjugation, absorb light in the UV or visible regions of the electromagnetic spectrum. Charge transfer complexes also give rise to colors. However, the colors are often too intense to be used for quantitative measurement. Nevertheless, UV–Vis spectroscopy can be used in order to qualitatively detect the existence of CT transitions in thin films. In the case of this study, the UV–Vis studies were undertaken

Contents

4.1	Physical Characterization.....	69
4.1.1	UV–Vis Spectroscopy	69
4.1.2	IR Spectroscopy	71
4.1.3	XRD Measurements.....	72
4.2	Electrical Characterization.....	74
4.2.1	Quasi Static Current–Voltage Measurements	74
4.2.2	Impedance Spectroscopy	82
4.2.3	Pulse Measurements	85
4.2.4	Temperature Dependence	92
4.3	Summary	94

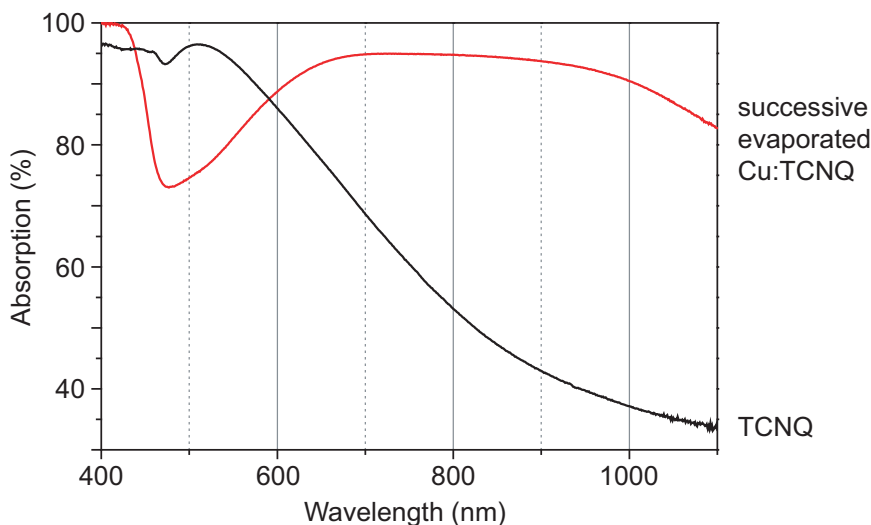


Figure 4.1: UV-Vis absorption spectrum of successive deposited Cu:TCNQ. Comparison of a TCNQ layer without annealing (pure TCNQ) and an annealed Cu:TCNQ layer. The thickness of the TCNQ and the Cu:TCNQ layer was 130 nm.

using an Unicam UV2 UV/Vis Spectrometer.

Iida reported on the optical properties of simple anion radical salts of TCNQ in general [99]. Later, Hoffman et al. specifically described the effects in Ag:TCNQ [100], and Liu et al. reported on Cu:TCNQ [78]. Typical for neutral TCNQ is a very broad absorption peak around a wavelength of 400 nm. This peak is responsible for the yellowish color of the TCNQ crystals and can be attributed to the ${}^2B_{2g} \rightarrow {}^2B_{1u}$, the ${}^2B_{2g} \rightarrow {}^2A_u$, and ${}^1A_g \rightarrow {}^1B_{3u}$ transitions [101]. Due to the measured spectrum range (wavelength > 400 nm), only parts of this broad peak can be seen on the UV-Vis measurements carried out on samples with a pure TCNQ layer, as shown in Fig. 4.1.

The TCNQ layer was successive deposited on top of a continuous Cu bottom electrode and spectroscopic measured without a prior annealing step. In contrast, after an annealing step at 125 °C on a hot plate for 45 s, as described in section 3.3.2, the absorption spectrum has changed considerably. In this case, the Cu:TCNQ displays the typical absorption peaks, which were previously described elsewhere [78]. In the blue band region, there is now one very strong and sharp peak around 400 nm visible, which can be attributed to TCNQ anion radicals (LE_2 band transition). Furthermore, three more peaks are expected to appear, one at 680 nm (LE_1 band transition), and the others at 744 nm, respectively 838 nm. The latter two are representing separate electronic transitions to the first two doublet excited states of TCNQ anion radicals and can be considered as the CT_1 transition. These three peaks are partly overlapping due to their proximity and broadness. In the case of this study, they are especially difficult to discriminate due to the resolution of the used measurement set up.

A typical UV-Vis absorption spectrum for a simultaneous evaporated Cu:TCNQ layer is shown in Fig. 4.2. Only slight differences to the spectrum measured on a successive deposited layer (Fig. 4.1) are visible. The formation of the CT complex is confirmed

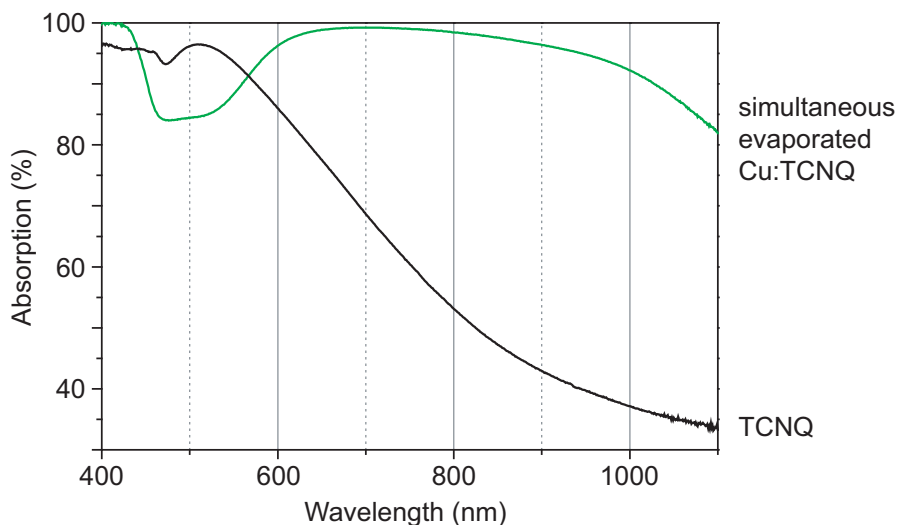


Figure 4.2: UV-Vis absorption spectrum of simultaneous deposited Cu:TCNQ. Comparison of a TCNQ layer without annealing (pure TCNQ) and a simultaneous evaporated Cu:TCNQ layer. The thickness of the TCNQ and the Cu:TCNQ layer was 130 nm.

in both cases. However, these measurements do not allow a quantitative interpretation. Therefore, the possibility of unreacted, neutral TCNQ within the Cu:TCNQ layer can not be ruled out due to these UV-Vis measurements.

4.1.2 IR Spectroscopy

It has been demonstrated, that the peaks in the infrared (IR) spectrum can be attributed to vibronic effects in a CT complex [102]. Therefore, IR spectra of devices were measured using a Nicolet Impact 410 Fourier Transform Infra Red (FTIR) spectrometer in the case of this study. The IR reflectance spectra of Cu:TCNQ thin films with a thickness of 130 nm, which were deposited using the simultaneous and the successive methods, are shown in Fig. 4.3.

Only slight shifts in the wavenumbers of the peaks between the simultaneous and the successive case can be observed. The $\text{C}\equiv\text{N}$ stretching region (visible in the chemical structure shown in Fig. 2.10) is characterized by the strong peak at 2197 cm^{-1} for the simultaneous (respectively 2200 cm^{-1} for the successive) case, and a shoulder at 2167 cm^{-1} (2166 cm^{-1}). The $\text{C}=\text{C}$ ring stretching region is characterized by two bands, a weak one at 1581 cm^{-1} (1577 cm^{-1}) and a sharper one at 1505 cm^{-1} (1508 cm^{-1}). The appearance of this peak at 1505 cm^{-1} (1508 cm^{-1}) indicates that TCNQ was changed to TCNQ anion radicals [103]. The band at 1352 cm^{-1} (1352 cm^{-1}) can also be attributed to the $\text{C}=\text{C}$ ring stretching region. The $\text{C}=\text{C}-\text{H}$ bending is characterized by the weak peak visible at 826 cm^{-1} (827 cm^{-1}). The other weak peaks observable in the spectra at 1185 cm^{-1} (1184 cm^{-1}) and 989 cm^{-1} (991 cm^{-1}), may be synergetic vibrations of both $\text{C}=\text{C}$ stretching and $\text{C}=\text{C}-\text{H}$ bending. The observed peaks in both, the simultaneous and the successive, cases are in good accordance with previous results published for amorphous thin films prepared by the solution growth method [103].

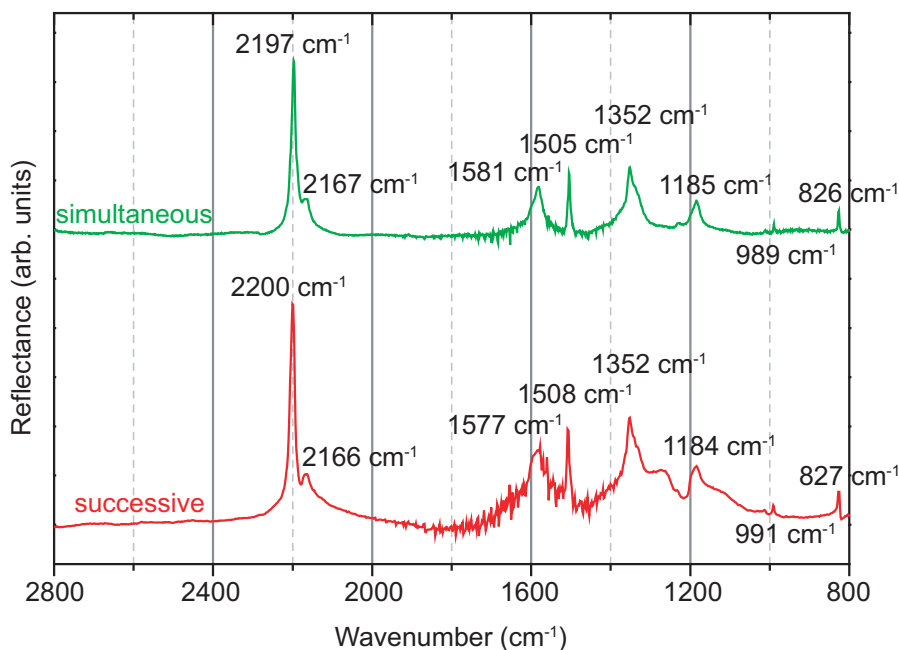


Figure 4.3: IR reflectance spectra of Cu:TCNQ layers. The films had a thickness of 130 nm and were deposited using the simultaneous and successive method.

Degree of Charge Transfer

In previous studies, it was shown that the degree of charge transfer (Z) between donor and TCNQ correlates linear with the wavenumber of the $\text{C}\equiv\text{N}$ stretching mode [104]. This nitrile stretching mode occurs at a wavenumber of 2227 cm^{-1} for neutral TCNQ. Chapell et al. demonstrated, that since the occupancy of the conduction band is $n_c = Z$ in simple salts, ω_0 should be a linear function of Z . They proved this assumption for a number of donor materials. Therefore, Z can be calculated by the simple Equation 4.1.

$$Z = \frac{\omega_0 - \omega}{44\text{ cm}^{-1}} \quad (4.1)$$

Calculated with this method, the $\text{C}\equiv\text{N}$ stretching peak at 2197 cm^{-1} for the simultaneous evaporated Cu:TCNQ results in $Z = 0.68$ and the successive evaporated reference sample with the peak at 2200 cm^{-1} results in $Z = 0.61$. These results place Cu:TCNQ, regarding the degree of charge transfer Z , in the area of other good conducting complexes of TCNQ (e.g. TTF:TCNQ with $Z = 0.59$, or TSF:TCNQ with $Z = 0.63$). On the other hand, complexes with a total charge transfer $Z = 1$ display insulating properties (e.g. Na:TCNQ, or K:TCNQ) as described in section 2.3.3.

4.1.3 XRD Measurements

Additional physical characterization measurements were conducted in order to verify, whether the deposited Cu:TCNQ layers display a polycrystalline or an amorphous

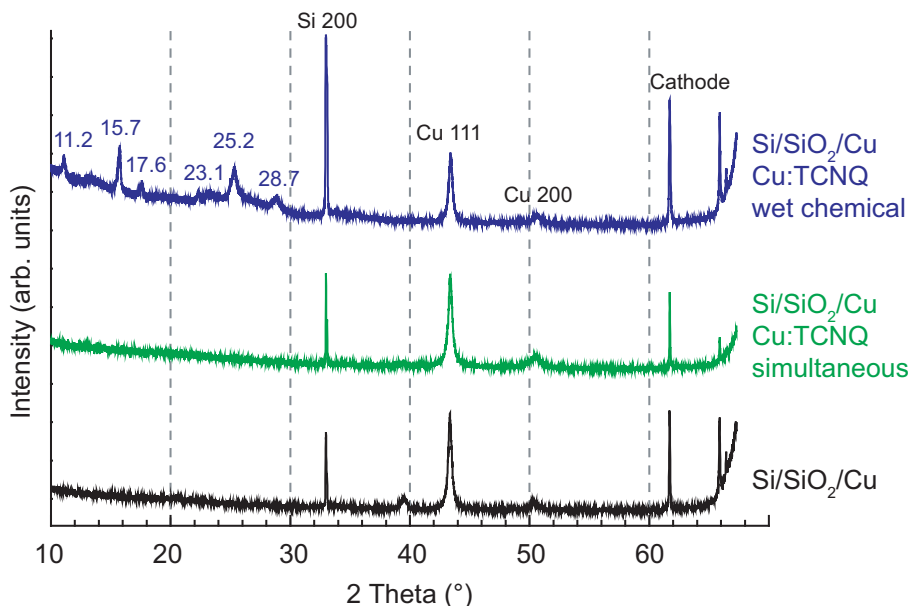


Figure 4.4: XRD measurements on different types of samples. From bottom to top: Si/SiO₂ substrate with Cu bottom electrode, Si/SiO₂ substrate with Cu bottom electrode and simultaneous evaporated Cu:TCNQ layer, and Si/SiO₂ substrate with Cu bottom electrode and wet chemical processed Cu:TCNQ layer.

nature. Heintz et al. demonstrated, as mentioned in section 2.3.2, the existence of two different stable phases of Cu:TCNQ. In addition, this group published experimental X-ray Diffraction (XRD) data for both of the polycrystalline phases, measured on Cu:TCNQ powder, which was prepared by a wet chemical process [74].

In the case of this study, XRD measurements were carried out in ambient conditions with a Philips thin film diffractometer (PW 3710) coupled with a PW 1830 Generator operated at 40 kV and 35 mA. Multiple types of samples were scanned in the 2θ angular range between 10° and 70°. Some graphs of the x-ray intensity plotted over the scatter angle 2θ are displayed in Fig. 4.4.

These results are in good agreement with the observations made by SEM imaging on the morphology of the layers. Three exemplary intensity plots, measured on samples based on Si/SiO₂ substrates with Cu bottom electrodes, are shown in Fig. 4.4. The measurement on the sample with only the Cu bottom electrode (plot shown at the bottom) display the Si and Cu intensity peaks. The XRD measurements on samples with simultaneous evaporated Cu:TCNQ displayed no additional peaks, which means that those thin films are amorphous. However, samples prepared by the wet chemical method resulted in additional intensity peaks at 11.2, 15.7, 17.6, 23.1, 25.2, and 28.7°. These peaks correspond closely to the ones reported by Heintz et al. for phase I Cu:TCNQ [74]. This phase is described as monoclinic polycrystalline with a needle shaped morphology.

Since a resistance switching effect could be observed on the amorphous as well as the polycrystalline Cu:TCNQ layers, the proposed physical mechanism by Heintz et al.

can be discarded [74]. This theory, which is explained in more detail in section 2.3.4, involves a structural phase transition between two polycrystalline phases.

4.2 Electrical Characterization

The electrical characterization of the devices is the most important aspect of the characterization regarding both, the clarification of the switching mechanism, and the assessment of a possible usage in memory cells. Therefore, a wide range of electrical characterization methods were carried out on the devices. During the measurements, the devices were contacted using metal needles, which were manually controlled by micro manipulators. The devices themselves were placed in a Summit 9600 thermal probe station with a mounted microscope from the vendor Cascade Microtech. The devices could be cooled down to $-50\text{ }^{\circ}\text{C}$ and heated up to $200\text{ }^{\circ}\text{C}$ during measurements while using this probe station. The measurement equipment was connected to the contact needles via BNC cables. The load signal was always applied to the padsize top electrodes, while the continuous bottom electrode was connected to the ground input of the respective measurement unit.

4.2.1 Quasi Static Current–Voltage Measurements

Quasi static current–voltage measurements were used as the most important method for the verification of the fundamental electrical properties of the devices. These measurements were carried out using a Keithley 2410 Sourcemeter. This instrument has the advantage of a built-in current compliance. The limitation of the current is important, because otherwise the current level can increase abruptly by some orders of magnitude during the switching to the on-state. This often leads to a break through and therefore destruction of the memory cells.

An exemplary quasi static current–voltage measurement is shown in Fig. 4.5. After preparation, the memory cells were initially in the high ohmic off-state. One cycle is displayed with a linear progression of the applied voltage, starting from 0 V , decreasing to -3 V , increasing to $+3\text{ V}$, and decreasing back to 0 V . The applied voltage is changed discrete, in this case in 100 mV steps. Every step has a duration of 100 ms . Therefore, in this case the cycle consisted of 120 steps and the whole cycle had a duration of 12 s . For every step, the current is measured. Here, the current compliance was set to $100\text{ }\mu\text{A}$. If the current is limited to a compliance value, the voltage is, accordingly to Ohm's law, decreased. In the present case, during the switching to the on-state the current is limited to $100\text{ }\mu\text{A}$ and the applied voltage drops accordingly to a value of about -1.7 V . However, the Keithley sourcemeter records only the nominal values. While analyzing the data, this has to be taken into account.

The measuring points can be illustrated more clearly as a current over voltage $I(V)$ diagram. Two possible forms of this kind of diagram are shown exemplary in Fig. 4.6. The measurement data from Fig. 4.5 were used for these graphs.

A linear plot of the current is the first displayed graph (a), while the second graph is a logarithmic plot of the absolute current values (b). Naturally, the linear plot has a better resolution of the on-state current values. In contrast, the logarithmic plot allows for a general overview of both, on- and off-state currents even for large

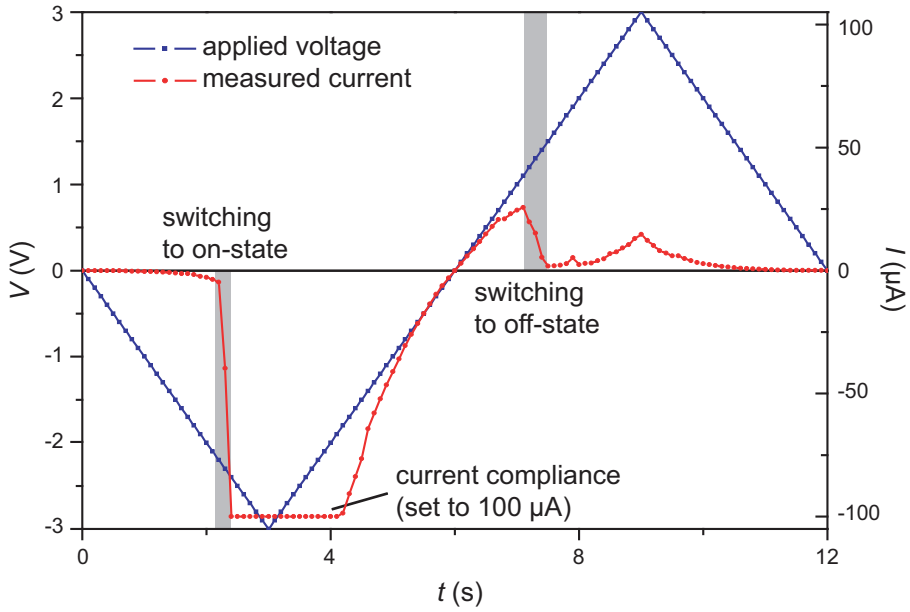


Figure 4.5: Exemplary current–voltage characteristic plotted over time. The parameters for this quasi static measurement were: nominal applied voltage cycle $0 \text{ V} \Rightarrow -3 \text{ V} \Rightarrow +3 \text{ V} \Rightarrow 0 \text{ V}$, voltage step width 100 mV , voltage step rate 10 Hz , current compliance $100 \mu\text{A}$, sample rate 10 Hz . This measurement was carried out on a successive evaporated device (Cu:TCNQ thickness: 150 nm) with Cu bottom and Al top electrode (pad diameter: 75μ).

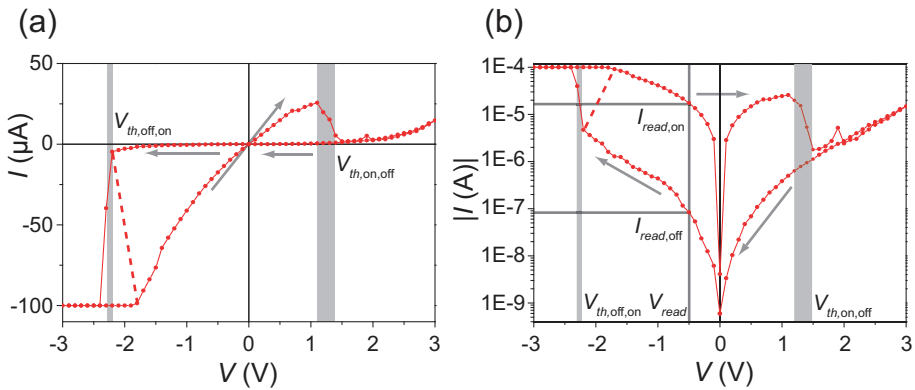


Figure 4.6: Exemplary linear and logarithmic current over voltage plots. The direction is indicated by arrows in both cases. Linear (a), and logarithmic (b) plot of the (absolute in case (b)) current values.

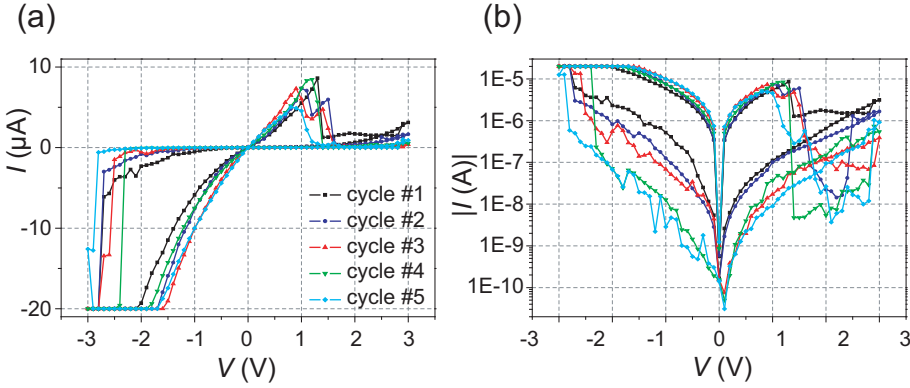


Figure 4.7: Current over voltage plots for a 150 nm successive deposited Cu:TCNQ layer. The parameters for this quasi static measurement were: nominal applied voltage cycle $0\text{ V} \Rightarrow -3\text{ V} \Rightarrow +3\text{ V} \Rightarrow 0\text{ V}$, voltage step width 100 mV, voltage step rate 10 Hz, current compliance 20 μA , sample rate 10 Hz. Linear (a), and logarithmic (b) plot of the (absolute in case (b)) current values for five cycles.

off/on ratios. The dashed lines in both cases indicate the corrected graphs, which take the above-mentioned differences in nominal versus true applied voltages due to the current compliance into consideration. The switching voltage threshold for on ($V_{th,off,on}$) and off switching ($V_{th,on,off}$) can be read out easily as indicated in the graphs. The resistance values for the off- (R_{off}) and on-state (R_{on}) are normally determined by pulse measurements (see section 4.2.3). However, they can be fairly well estimated using the logarithmic plot as shown in Fig. 4.6 (b). The current value at the defined read voltage (V_{read}) is measured in both, the on- and off-state branch. For this example the following values can be calculated for $V_{read} = -0.5\text{ V}$:

$$R_{off}(V_{read}) = \left| \frac{I_{off}(V_{read})}{V_{read}} \right| \Rightarrow R_{off}(-0.5\text{ V}) = \left| \frac{I_{off}(-0.5\text{ V})}{-0.5\text{ V}} \right| = 6\text{ M}\Omega$$

$$R_{on}(V_{read}) = \left| \frac{I_{on}(V_{read})}{V_{read}} \right| \Rightarrow R_{on}(-0.5\text{ V}) = \left| \frac{I_{on}(-0.5\text{ V})}{-0.5\text{ V}} \right| = 29\text{ k}\Omega$$

Measurements on Devices Prepared by the Successive Method

Quasi static current-voltage measurements were carried out on devices with Cu:TCNQ layers prepared by the successive evaporation route, which is described in section 3.3.1. The characterized memory cells had a simple capacitor like structure, consisting of a continuous Cu bottom electrode (150 nm), the Cu:TCNQ layer, and a circular Al top electrode (130 nm). The device setup is described in more detail in section 3.3.4. These memory cells exhibited bipolar resistive switching. The on-switching occurred at negative applied voltages to the Al top electrode, while the off-switching was achieved by the application of a positive voltage.

Typical $I(V)$ measurements for those types of devices are shown in Fig. 4.7 for a 150 nm, and in Fig. 4.8 for a 200 nm Cu:TCNQ layer. Some typical characteristics can be observed in these graphs.

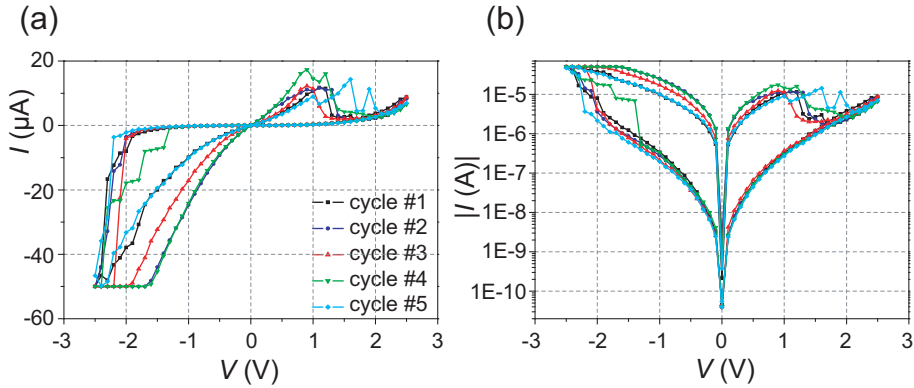


Figure 4.8: Current over voltage plots for a 200 nm successive deposited Cu:TCNQ layer. The parameters for this quasi static measurement were: nominal applied voltage cycle $0\text{ V} \Rightarrow -2.5\text{ V} \Rightarrow +2.5\text{ V} \Rightarrow 0\text{ V}$, voltage step width 100 mV, voltage step rate 10 Hz, current compliance 50 μA, sample rate 10 Hz. Linear (a), and logarithmic (b) plot of the (absolute in case (b)) current values for five cycles.

Switching Threshold Voltages

The absolute value of the switching threshold voltage for the on-switching $V_{th,off,on}$ for most samples was greater than for the off-switching $V_{th,on,off}$. The distribution of the switching thresholds for successive deposited memory cells with a Cu:TCNQ thickness of $\approx 150\text{ nm}$ is shown in the histogram in Fig. 4.9. The values can be fitted decently by a normal distribution for both cases. As a result of these measurements, the mean value for the on-switching can be calculated to $V_{th,off,on} = -2.4\text{ V}$, and the mean value for the off-switching to $V_{th,on,off} = +1.6\text{ V}$.

The switching thresholds displayed no dependence on the pad size of the top electrode in the studied range. The circular pads thereby had diameters between 75 μm and 500 μm with the according areas as stated in Table 3.6. The larger the cell areas were, the more of them were initially short due to defects. Therefore, the memory cells with a pad diameter of 1000 μm could not be measured in this case.

The current-voltage characteristics were studied on devices with different Cu:TCNQ thicknesses. The successive deposited films were between 90 nm and 400 nm thick. No significant trend of a dependence of the switching threshold on the thickness of the Cu:TCNQ layer could be observed within this range.

Current-Voltage Dependences in the Low- and High-Ohmic Branch

The successive prepared memory cells displayed a non-linear current dependence on the applied voltage in the on-state (low-ohmic branch) as visible in Fig. 4.7 and Fig. 4.8. The devices exhibited an even more pronounced non-linear current-voltage behavior in the off-state (high-ohmic branch). The off-state dependency is discussed in more detail in section 5.1.1.

First Cycle (Forming)

The $I(V)$ measurements carried out on numerous Cu:TCNQ devices demonstrated

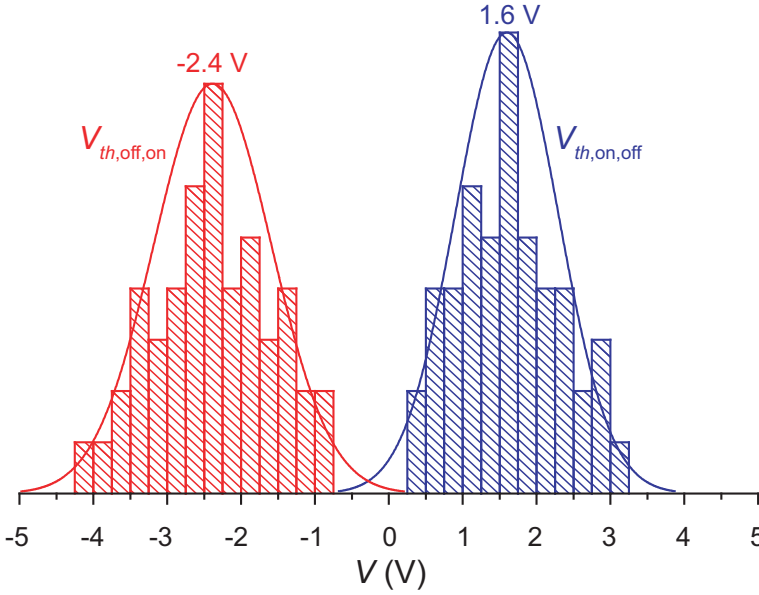


Figure 4.9: Histogram of the switching thresholds for successive deposited devices. The plot shows the distribution of $V_{th,off,on}$ and $V_{th,on,off}$ for successive deposited memory cells with a Cu:TCNQ thickness of ≈ 150 nm.

that the memory cells do not require a specific forming operation, or the initial forming is just a modified set operation with slightly different $I(V)$ characteristics. Fig. 4.10 shows the first 20 current–voltage cycles of a device with a 200 nm successive deposited Cu:TCNQ layer in a logarithmic plot. The initial switching to the on–state (indicated by the black line and squares in Fig. 4.10) in this case requires an increased voltage level ($V_{th,initial,on} \approx -2.1$ V). The switching to the on–state during the subsequent cycles occurs at -1.6 V $\leq V_{th,off,on} \leq -0.9$ V. In most cases, the difference between $V_{th,initial,on}$ and $V_{th,off,on}$ was less pronounced, or even not visible, which can be seen in Fig. 4.7 and Fig. 4.8.

Measurements on Devices Prepared by the Simultaneous Method

Quasi static current–voltage measurements were also carried out on devices with Cu:TCNQ layers prepared by the simultaneous evaporation route, which is described in section 3.3.3. The characterized memory cells had a simple capacitor like structure, consisting of a continuous Cu bottom electrode (100 nm), the Cu:TCNQ layer, and a circular Al top electrode (130 nm). The device setup is described in more detail in section 3.3.4. These memory cells exhibited also bipolar resistive switching with the same polarity dependence as the successive ones described earlier in section 4.2.1. The on–switching again occurred at negative applied voltages to the Al top electrode, while the off–switching was achieved by the application of a positive voltage. One important aspect observed during the measurements is the fact that the fraction of memory cells, which exhibits resistive switching, is significantly lower than the one for devices prepared by the successive method.

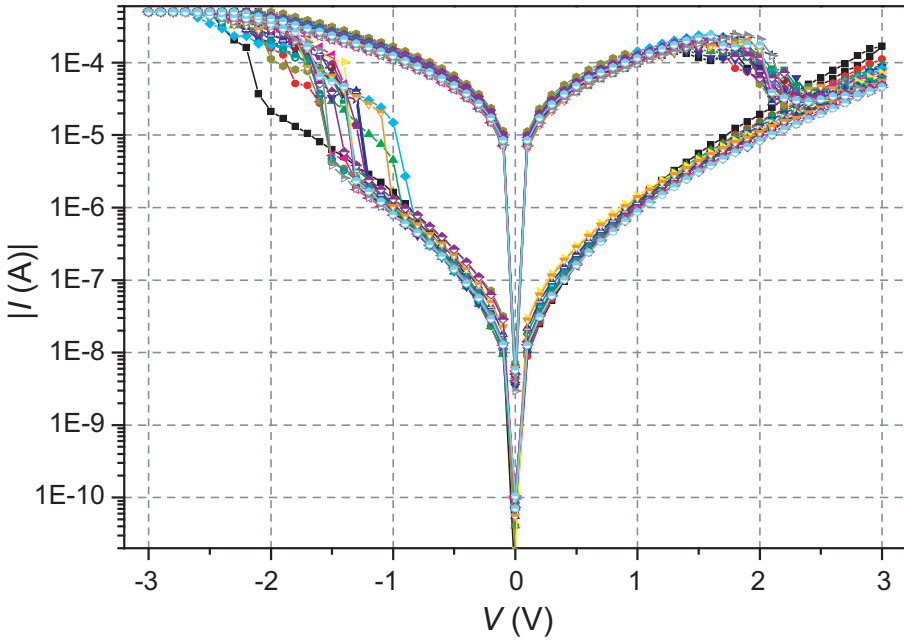


Figure 4.10: Current over voltage plots for a 200 nm successive deposited Cu:TCNQ layer. The parameters for this quasi static measurement were: nominal applied voltage cycle $0\text{ V} \Rightarrow -3\text{ V} \Rightarrow +3\text{ V} \Rightarrow 0\text{ V}$, voltage step width 100 mV, voltage step rate 10 Hz, current compliance 500 μA , sample rate 10 Hz. Logarithmic plot of the absolute current values for twenty cycles.

A typical $I(V)$ characteristic measured on a device with a 150 nm thick simultaneous evaporated Cu:TCNQ layer is shown in Fig. 4.11. A single current–voltage cycle measured on a memory cell with a Cu:TCNQ layer thickness of 100 nm is shown in Fig. 4.12.

The measured quantitative parameters ($V_{th,off,on}$, $V_{th,on,off}$, R_{off} , R_{on}) displayed distinctive different values in comparison to the successive samples as visible in the graphs. The voltage thresholds for both, the switching to the on– and off–state were significantly higher. The on–switching occurred predominately at voltages in the range of $-11\text{ V} \leq V_{th,off,on} \leq -6\text{ V}$. The off–switching process displayed an even larger spread of the threshold voltages (somewhere in the range of $+1.5\text{ V} \leq V_{th,off,on} \leq +10\text{ V}$). The stability of the on–state at positive bias voltages was in general worse than at negative bias voltages as visible in Fig. 4.11.

The resistance values in both, off– and on–state, were much higher for simultaneous prepared Cu:TCNQ than for successive memory cells with identical device parameters (film thickness, pad area, electrode structure). The differences in the resistance values amounted to roughly a factor of 100 valid for both, the off– and on–state.

Comparable to the successive memory cells, the switching threshold voltages displayed no dependence on the pad size of the top electrode in the studied range. Furthermore, no significant trend of a dependence of the switching threshold from the Cu:TCNQ layer thickness could be observed within the studied range (70 nm to

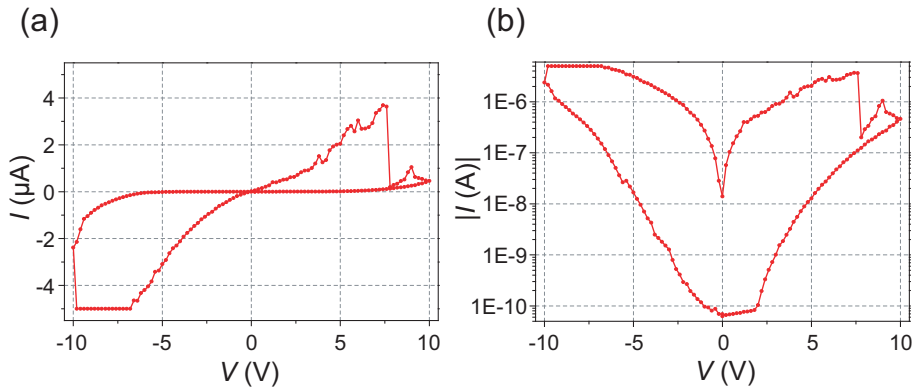


Figure 4.11: Current over voltage plots for a 150 nm simultaneous deposited Cu:TCNQ layer. The parameters for this quasi static measurement were: nominal applied voltage cycle $0\text{ V} \Rightarrow -11\text{ V} \Rightarrow +11\text{ V} \Rightarrow 0\text{ V}$, voltage step width 100 mV, voltage step rate 10 Hz, current compliance $5\text{ }\mu\text{A}$, sample rate 10 Hz. Linear (a), and logarithmic (b) plot of the (absolute in case (b)) current values for a three cycles.

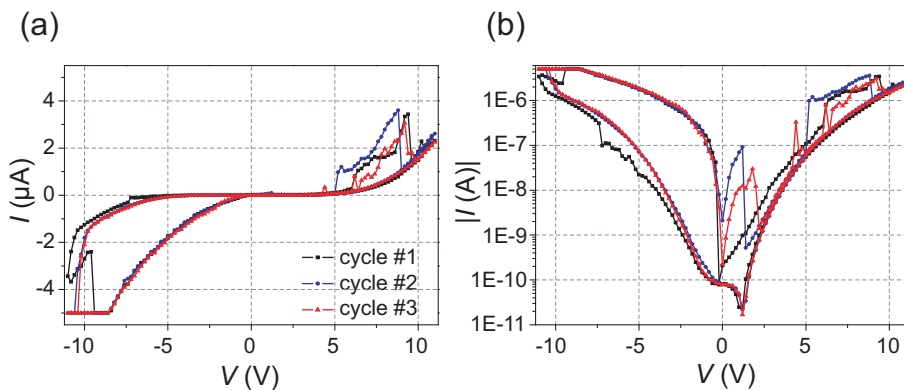


Figure 4.12: Current over voltage plots for a 100 nm simultaneous deposited Cu:TCNQ layer. The parameters for this quasi static measurement were: nominal applied voltage cycle $0\text{ V} \Rightarrow -10\text{ V} \Rightarrow +10\text{ V} \Rightarrow 0\text{ V}$, voltage step width 100 mV, voltage step rate 10 Hz, current compliance $5\text{ }\mu\text{A}$, sample rate 10 Hz. Linear (a), and logarithmic (b) plot of the (absolute in case (b)) current values for a single cycle.

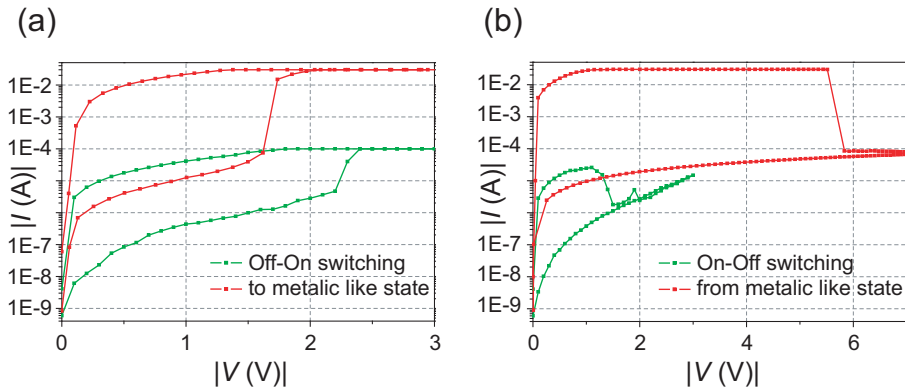


Figure 4.13: *Unipolar switching to a metallic like state. Comparison of the on-switching (a), and the off-switching process (b) of the unipolar and the bipolar switching effect. Plotted are the absolute current over voltage characteristics.*

400 nm). Those measurements were additionally complicated by the above-mentioned large spreads of the switching threshold voltages.

Similar to the successive case, the simultaneous prepared memory cells displayed non-linear current dependencies on the applied voltages in both states. This can be seen in Fig. 4.12.

Unipolar Switching to Metallic Like State

Besides the above-described bipolar resistive switching behavior, a small fraction of samples exhibited an unipolar switching, independent on the preparation method (successive or simultaneous). In fact, in a few cases both switching types could be measured on the same memory cells.

A comparison of the on- and off-switching processes of the unipolar and the bipolar switching effect is shown in Fig. 4.13. These measurements were carried out on a successive evaporated device with a Cu:TCNQ thickness of 150 nm and an Al top electrode with a diameter of 75 μm . The maximum current was restricted to 40 mA due to measurement device limitations.

The switching to the metallic like state occurred spontaneously by the application of a voltage independent of the polarity of the signal. The threshold voltage for this effect was between 1.5 V and 5 V. This switching resulted in a fairly unstable metallic like state with a resistance of below 100 Ω . On removal of the applied voltage the memory cells returned to the high resistance state after a short period of time (seconds to minutes). Reverse switching could just as well be caused by application of a higher voltage signal of about 6 V also independent of polarity as shown in Fig. 4.13 (b). The switching effect in both directions was abrupt.

These observed characteristics are in good accordance to the switching effect initially described by Potember et al. in 1979 [14]. They reported bistable electrical switching in a lamellar structure with a Cu:TCNQ layer between Cu and Al electrodes. The $I(V)$ characteristics in their case revealed an abrupt decrease in impedance from 2 M Ω to

less than 200Ω at a field strength of $4 \times 10^3 \text{ V/cm}$ independent on the direction of the current flow.

These experiments indicate that two distinctive reversible resistive switching effects, and therefore three different conductivity states (R_{met} , R_{on} , and R_{off}) can exist in Cu:TCNQ thin films [107].

4.2.2 Impedance Spectroscopy

Further electrical characterizations were conducted in order to determine the capacitance values of the devices as well as the frequency behavior of the impedance. Therefore, impedance spectra of the test structures in the frequency domain (100 Hz–10 MHz) were measured at zero dc-bias with a voltage oscillation amplitude of 50 mV using a HP 4194A impedance analyzer.

One exemplary capacitance and resistance characteristic, measured in the above stated frequency domain, is shown in Fig. 4.14. The device setup in this case consisted of a 100 nm Cu bottom electrode, a 150 nm thick, successive deposited Cu:TCNQ layer and a 130 nm Al top electrode. The displayed measurement was carried out on a circular top electrode pad with a diameter of $75 \mu\text{m}$. The measurement was executed as follows:

- the memory cell was switched a couple of times between off- and on-state in order to ensure functionality
- the impedance was measured during a frequency sweep in the off-state
- the memory cell was switched to the on-state
- the impedance was measured during a frequency sweep in the on-state

The characteristics shown in Fig. 4.14 are typical for the results. A clear difference between R_{off} and R_{on} can be seen, with off/on ratios similar to the ones observed in the quasi static current–voltage measurements. However, the capacitance values of C_{off} and C_{on} remain constant within the error of measurement, independent of the resistance state.

Furthermore, a relaxation step is visible in the frequency domain. This is due to the fact, that the device represents a simple, parallel RC-circuit. The time constant τ can be calculated as follows:

$$\tau = RC \quad (4.2)$$

Using Eq. 4.2, the time constant for the memory cell shown in Fig. 4.14 can be calculated to

$$\tau_{\text{off}} = 2.2 \text{ M}\Omega \cdot 40 \text{ pF} = 88 \mu\text{s}$$

in the off-state and to

$$\tau_{\text{on}} = 50 \text{ k}\Omega \cdot 40 \text{ pF} = 2 \mu\text{s}$$

in the on-state. These steps can be seen in the resistance plot at the corresponding frequencies (11 kHz and 500 kHz respectively).

The capacitance values were measured in dependence of the top electrode area. The different available circular pad sizes are summarized in Table 3.6. The off- and on-state

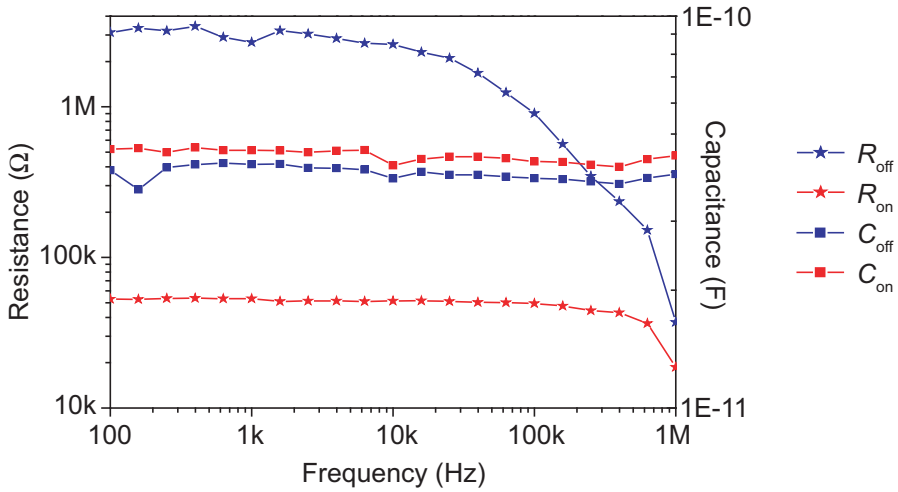


Figure 4.14: Exemplary impedance spectroscopy measurement. Capacitance and resistance characteristics plotted over frequency. The parameters for this measurement were: frequency domain (100 Hz–10 MHz), zero dc-bias, voltage oscillation amplitude 50 mV. This measurement was carried out on a successive evaporated device (Cu:TCNQ thickness: 150 nm) with Cu bottom and Al top electrode (pad diameter: 75 μm).

capacitances are shown in Fig. 4.15 for a successive (a), and a simultaneous (b) deposited Cu:TCNQ layer. The device setup in both cases consisted again of a Cu (100 nm) / Cu:TCNQ (150 nm) / Al (130 nm) layered structure.

For both, the successive and the simultaneous deposited films, no change in the capacitance can be seen due to the resistive switching effect. However, the memory cells

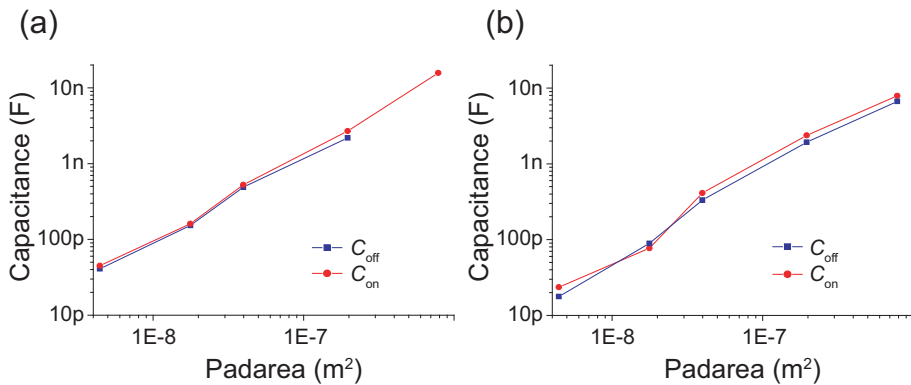


Figure 4.15: Top electrode area dependence of the capacitance. Comparison of the off- and on-state capacitance measured on a successive (a), and a simultaneous evaporated device (b). Both have a Cu:TCNQ layer thickness of 150 nm and a Cu bottom and Al top electrode.

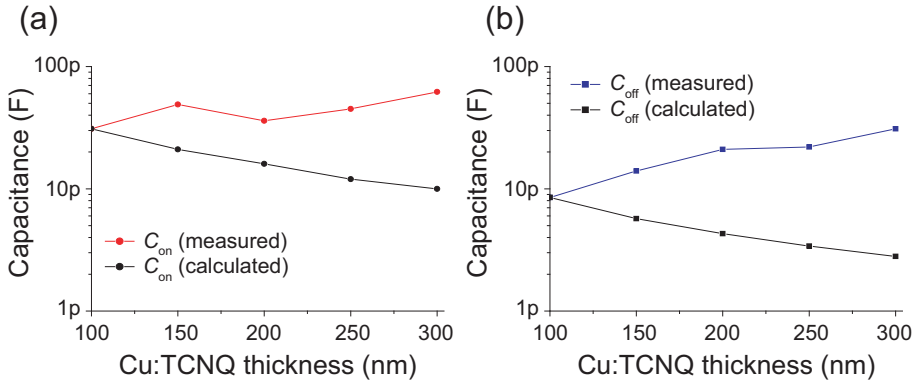


Figure 4.16: *Cu:TCNQ* thickness dependence of the capacitance. Comparison of measured and calculated capacitance values for a successive evaporated device in the on-state (a), and a simultaneous evaporated device in the off-state (b). Both have a Cu bottom and an Al top electrode with a diameter of 75 μm .

prepared by the successive method displayed approximately twice as high capacitance values for the same thickness and pad area as the ones prepared by the simultaneous process.

The function of the capacitance values over the top electrode area matches well to the values calculated with the assumption of a simple, parallel plate capacitor,

$$C = \epsilon_0 \epsilon_r \frac{A}{d} \quad (4.3)$$

where A is the plate area, d denotes the distance, and ϵ_r is the dielectric constant of the material between the plates. Assuming that the Cu:TCNQ can be estimated as a homogeneous dielectric material, a calculation of the dielectric constant using Eq. 4.3 is possible. This calculation results in $\epsilon_r \approx 200$ for the successive deposited Cu:TCNQ layers, and $\epsilon_r \approx 100$ for the simultaneous deposited Cu:TCNQ films. These values are extremely high for such a type of material. An interpretation of these values is discussed later in section 5.

Furthermore, the capacitance values were measured in dependence of the Cu:TCNQ thickness. For these purposes, devices with thicknesses between 100 nm and 300 nm were prepared in 50 nm steps, using the successive and the simultaneous deposition method. Two exemplary results of those measurements are shown in Fig. 4.16 for the successive (a), and simultaneous (b) deposited memory cells. The device setup in all cases consisted again of a Cu (100 nm) / Cu:TCNQ / Al (130 nm) layered structure, and the displayed measurements were carried out on circular top electrodes with a diameter of 75 μm .

The respective plot of the capacitance values for the on-state in successive (a), and for the off-state in simultaneous (b) deposited memory cells is compared with calculated values. This calculation is based on Eq. 4.3 with the assumption, that A and ϵ_r are independent of the Cu:TCNQ thickness. Therefore, the capacitance values can be

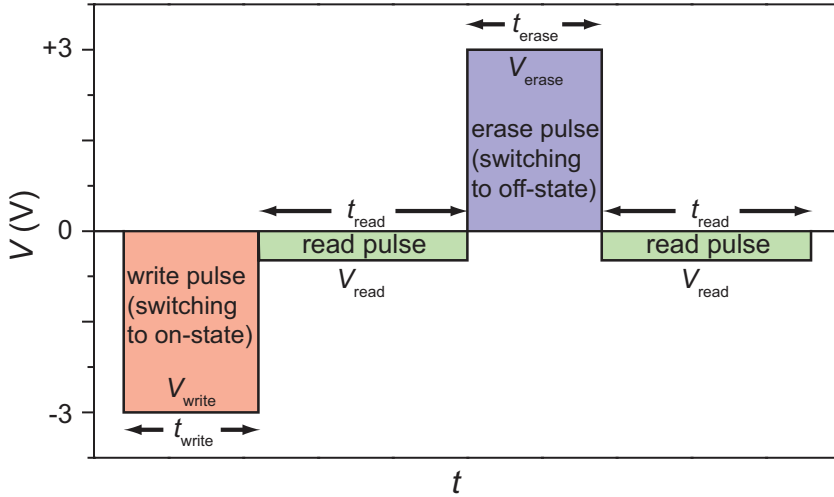


Figure 4.17: Exemplary applied voltage signal for a pulse cycle.

calculated using Eq. 4.4.

$$C(d_2) = C(d_1) \frac{d_1}{d_2} \quad (4.4)$$

In the case of Fig. 4.16, the capacitances of the memory cells with a Cu:TCNQ thickness of 100 nm were used as the starting points for the calculation.

The calculated values result in the expected dependence: the capacitance decreases with increasing thickness of the dielectric material in the case of constant A and ϵ_r . However, the measurements on the Cu:TCNQ memory cells exhibit a different behavior as shown in Fig. 4.16. The capacitance is barely changed, or even increasing, with increasing dielectric layer thickness. An interpretation of these values is discussed later in section 5.

4.2.3 Pulse Measurements

Pulse measurements of the current–voltage characteristics were carried out on the devices in order to determine further electrical properties. These measurements were conducted using a Keithley 2410 Sourcemeter with a built-in current compliance for the standard characterizations. The switching time characteristics were measured using a custom–designed, computer controlled current–voltage measuring system.

In order to ensure functionality and determine the switching voltage thresholds, the memory cells were characterized using a current–voltage measurement prior to the pulse measurements. For example, for the device with the $I(V)$ characteristic shown in Fig. 4.10, the write pulse voltage was set to $V_{\text{write}} = -3 \text{ V} < V_{th, \text{off}, \text{on}}$, the erase pulse voltage to $V_{\text{erase}} = +3 \text{ V} > V_{th, \text{on}, \text{off}}$, and the read pulse voltage to $V_{\text{read}} = -0.5 \text{ V}$. The applied voltage signal for this case is shown schematically for one pulse cycle in Fig. 4.17.

The used Keithley 2410 Sourcemeter has a minimum time resolution of 100 ms.

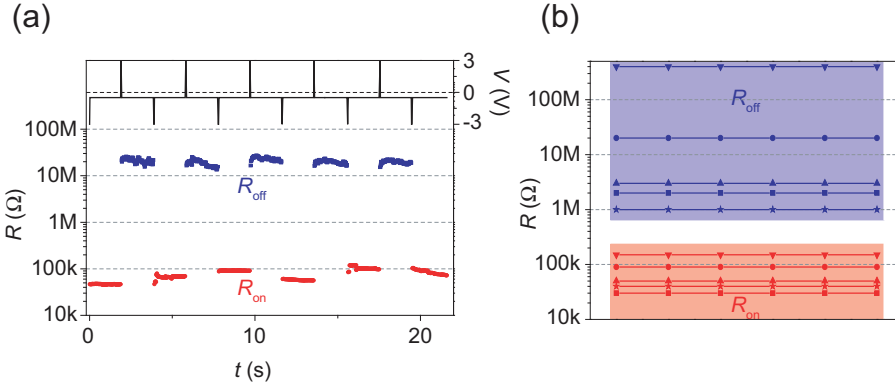


Figure 4.18: *Pulse measurement on a successive deposited memory cell with a Cu:TCNQ thickness of 200 nm, a Cu bottom, and an Al top electrode (with 75 μm diameter). Measurement parameters: $V_{\text{write}} = -3\text{ V}$, $V_{\text{erase}} = +3\text{ V}$, $V_{\text{read}} = -0.5\text{ V}$, $t_{\text{write}} = t_{\text{erase}} = 100\text{ ms}$, $t_{\text{read}} = 2\text{ s}$. (a) Plot of $R(t)$ and $V(t)$, and (b) R_{off} and R_{on} for measurements on five different memory cells on the same sample.*

Therefore, the current was measured, and a data point recorded, every 100 ms. The minimum width of the write, erase, and read pulses were restricted to 100 ms for the standard, retention, and endurance measurements due to the sourcemeter's limitations.

Pulse Measurements on Devices Prepared by the Successive Method

An exemplary result of a pulse measurement on a successive deposited device is shown in Fig. 4.18 (a). The resistance measured at $V_{\text{read}} = -0.5\text{ V}$ is plotted over time. The corresponding applied voltage is shown in the upper part of the graph. Both states, $R_{\text{off}} = 20\text{ M}\Omega$ and $R_{\text{on}} = 90\text{ k}\Omega$, display good stability with an off/on ratio of ≈ 200 . However, the resistance states vary considerably even between memory cells on the same sample with identical geometrical parameters. The resulting memory states of the pulse measurement shown in Fig. 4.18 (a) and four adjacent cells on the same device are shown in Fig. 4.18 (b). In this case, the off-state varies between $1\text{ M}\Omega$ and $400\text{ M}\Omega$, while the on-state varies between $30\text{ k}\Omega$ and $150\text{ k}\Omega$.

The distribution of the resistance values for the off- and the on-state for successive deposited memory cells with a Cu:TCNQ thickness of $\approx 150\text{ nm}$ and an Al top electrode with a diameter of $75\text{ }\mu\text{m}$ is shown in the histogram in Fig. 4.19. A wide spread of the resistance states is clearly visible. A factor of ≈ 330 exists between $R_{\text{off,max}} = 400\text{ M}\Omega$ and $R_{\text{off,min}} = 120\text{ k}\Omega$. The factor in the on-state is somewhat lower (≈ 50) with $R_{\text{on,max}} = 250\text{ k}\Omega$ and $R_{\text{on,min}} = 5\text{ k}\Omega$.

The resistance values for off- and on-state are plotted in dependence of the pad size of the Al top electrode for successive deposited Cu:TCNQ with a thickness of roughly 150 nm in Fig. 4.20. The circular pads thereby had diameters between $75\text{ }\mu\text{m}$ and $500\text{ }\mu\text{m}$ with the according areas as stated in Table 3.6. The larger the cell areas were, the more of them were initially short due to defects. Therefore, the memory cells with a pad diameter of $1000\text{ }\mu\text{m}$ could not be measured in this case.

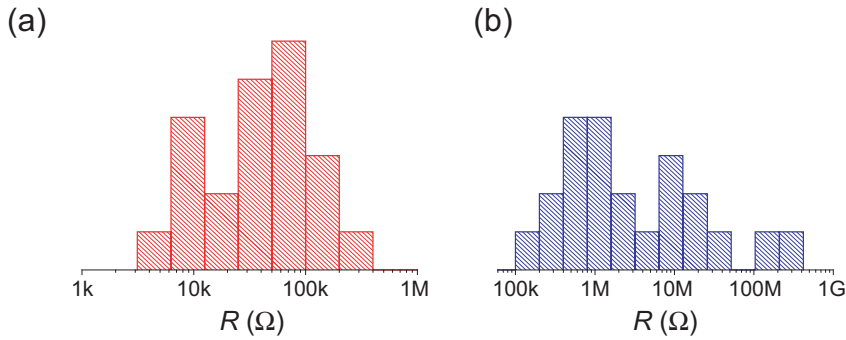


Figure 4.19: Histogram of the off- and on-state resistances for successive deposited devices. The plot shows the distribution of R_{off} and R_{on} for successive deposited memory cells with a Cu:TCNQ thickness of ≈ 150 nm and an Al top electrode with a diameter of $75 \mu\text{m}$. The mean value for the on-state is $70 \text{ k}\Omega$ and $30 \text{ M}\Omega$ for the off-state, the median is $50 \text{ k}\Omega$ for the on- and $1 \text{ M}\Omega$ for the off-state.

Again, a large spread of the resistance values, and therefore a partial overlap of the off- and on-state resistances ($R_{\text{off,min}} < R_{\text{on,max}}$) is visible. The data points within the studied range indicate, that the on-state resistance is probably independent of the pad size, while the off-state resistance decreases with increasing pad size.

Pulse measurements were carried out on devices with different Cu:TCNQ thicknesses. The successive deposited films were between 90 nm and 400 nm thick. No significant trend of a dependence of the resistance values in off- or on-state on the thickness of the Cu:TCNQ layer could be observed within this range. However, the large spread in the resistance values possibly obscures changes due to the, in comparison, minor thickness differences.

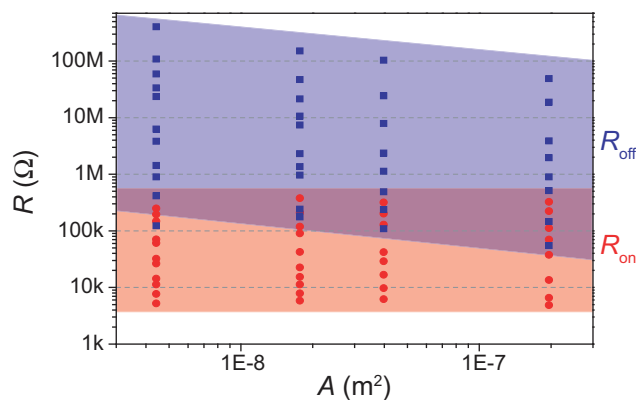


Figure 4.20: Plot of the off- and on-state resistance values vs. pad size. Measured on devices prepared by the successive method with a Cu:TCNQ thickness of 150 nm and Al top electrodes.

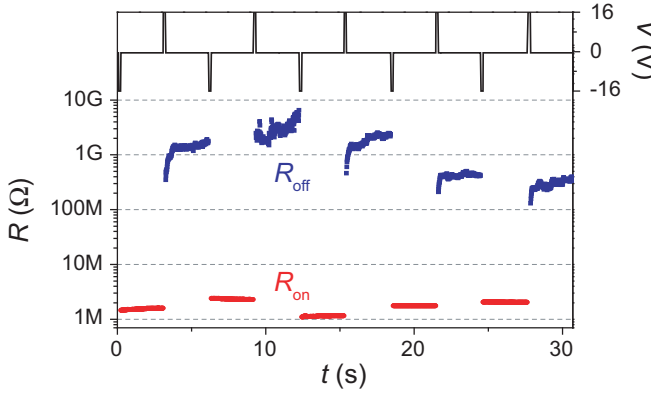


Figure 4.21: Pulse measurement on a simultaneous deposited memory cell. The sample had a Cu:TCNQ thickness of 200 nm, a Cu bottom, and an Al top electrode (with 75 μm diameter). Measurement parameters: $V_{\text{write}} = -16\text{ V}$, $V_{\text{erase}} = +16\text{ V}$, $V_{\text{read}} = -0.5\text{ V}$, $t_{\text{write}} = t_{\text{erase}} = 100\text{ ms}$, $t_{\text{read}} = 3\text{ s}$. Plot of $R(t)$ and $V(t)$.

Pulse Measurements on Devices Prepared by the Simultaneous Method

Pulse measurements were also carried out on devices with Cu:TCNQ layers prepared by the simultaneous evaporation route. As described in section 4.2.1, the fraction of memory cells, which exhibit resistive switching is significantly lower than the one for devices prepared by the successive method. Also, the switching threshold voltages are significantly higher. The resulting $R(t)$ characteristic of a typical pulse measurement on a memory cell with a 200 nm thick simultaneous evaporated Cu:TCNQ layer is shown in Fig. 4.21.

The write and erase voltages in this case are set to $V_{\text{write}} = -16\text{ V}$, $V_{\text{erase}} = +16\text{ V}$, in order to ensure resistive switching. As already shown in section 4.2.1, the resistance states are much higher for simultaneous evaporated samples than for the successive evaporated ones. In the case of the pulse measurement shown in Fig. 4.21, the on-state resistance is $R_{\text{on}} \approx 2\text{ M}\Omega$, while the off-state is less stable with a resistance value of $100\text{ M}\Omega < R_{\text{off}} < 8\text{ G}\Omega$. Resistance values in the $\text{G}\Omega$ range result in sub-nano ampere currents at the read voltage $V_{\text{read}} = -0.5\text{ V}$. It has to be taken into consideration, that these currents are close to the minimum measurement setup sensitivity.

Failure Types during Pulse Measurements

Three different failure types could be observed to occur during pulse measurements. Exemplary $R(t)$ plots are shown in Fig. 4.22 for the respective types. Some memory cells remain in the off-state (Fig. 4.22 (a)), or in the on-state (Fig. 4.22 (b)) at a certain point of the measurement. In these cases, it is sometimes possible to switch the cells again by an increase of the write/erase voltages. The third occurring failure type is the electrical break down of the memory cell, which results in a persistent short state (Fig. 4.22 (c)).

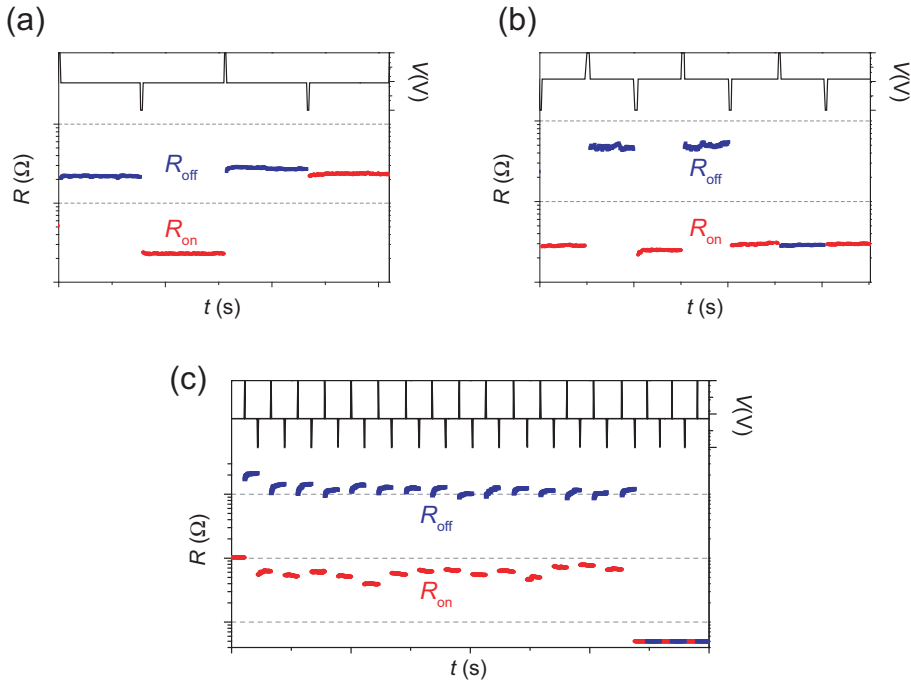


Figure 4.22: $R(t)$ plots of the failure types occurring during pulse measurements. (a) Memory cell remains in off-state. (b) Memory cell remains in on-state. (c) Memory cell breaks down and is shorted.

Retention Measurements

Pulse measurements with elongated read times t_{read} were carried out on memory cells in order to determine the retention times in the off- and on-state. The result of a typical measurement on a successive deposited Cu:TCNQ device is shown as a $R(t)$ plot in Fig. 4.23. Here, the memory cell was switched to the respective state and the resistance was then measured at an applied voltage of -0.5 V every 100 ms for a period of $t_{read} = 1$ h.

These measurements showed, that the off-state is stable over time. In contrast, the memory cell sometimes switches spontaneously from the on-state to the off-state after a period of time. In general, the memory cells displayed good stability over the studied time frame (up to a few hours). Sezi et al. already demonstrated retention times of >250 days for Cu:TCNQ memory cells [108].

Endurance Measurements

The maximal endurance of the prepared memory cells was determined. For this reason, a large number of write-read-erase-read cycles, consisting of the voltage pulse sequence shown in Fig. 4.17, and using the minimal time resolutions of the sourcemeter, was applied to the devices. Therefore, the pulse widths were set to $t_{write} = t_{erase} = t_{read} = 100$ ms.

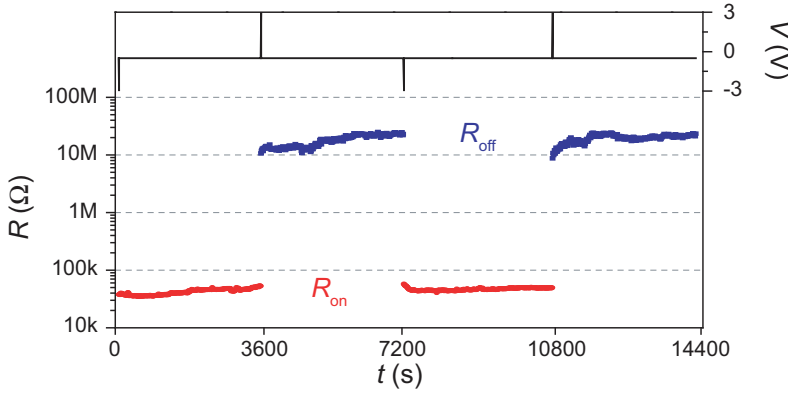


Figure 4.23: Retention measurement on a successive deposited device. The sample had a Cu:TCNQ thickness of 200 nm, a Cu bottom, and an Al top electrode (with 75 μm diameter). Measurement parameters: $V_{\text{write}} = -3\text{ V}$, $V_{\text{erase}} = +3\text{ V}$, $V_{\text{read}} = -0.5\text{ V}$, $t_{\text{write}} = t_{\text{erase}} = 100\text{ ms}$, $t_{\text{read}} = 3600\text{ s}$. Plot of $R(t)$ and $V(t)$.

This measurements demonstrated, that the memory cells prepared by the successive method displayed a better cycling endurance than the ones prepared by the simultaneous route. Some memory cells achieved an endurance of up to 10000 write–read–erase–read cycles [107]. A resistance over the number of cycles plot of such a measurement is shown in Fig. 4.24. In this case, the minimum off/on ratio results in a value of:

$$\frac{R_{\text{off,min}}}{R_{\text{on,max}}} = \frac{1.16\text{ M}\Omega}{515\text{ k}\Omega} = 2.25.$$

These measurements are in good accordance to results published by other groups on Cu:TCNQ memory cells with pad areas in the μm range [108, 109].

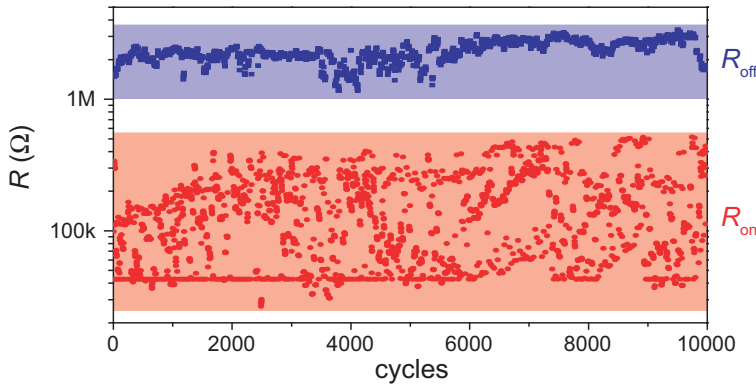


Figure 4.24: Endurance measurement on a successive deposited device. The sample had a Cu:TCNQ thickness of 150 nm, a Cu bottom, and an Al top electrode (with 75 μm diameter). Measurement parameters: $V_{\text{write}} = -3\text{ V}$, $V_{\text{erase}} = +3\text{ V}$, $V_{\text{read}} = -0.5\text{ V}$, $t_{\text{write}} = t_{\text{erase}} = t_{\text{read}} = 100\text{ ms}$. Plot of $R(\text{cycles})$.

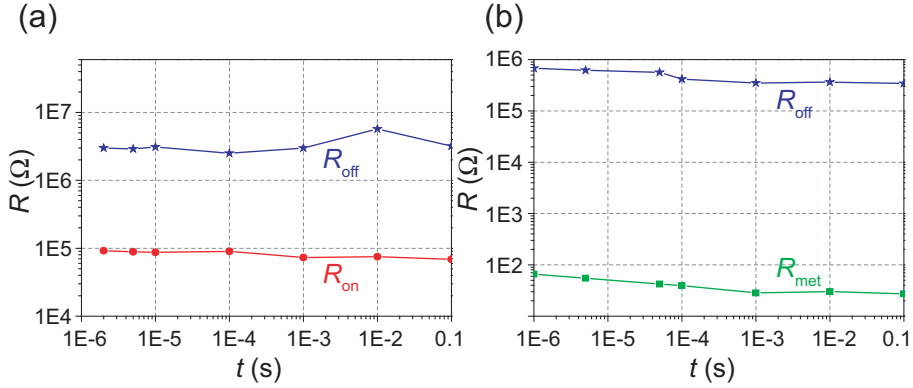


Figure 4.25: Resistance states dependence on the write/erase pulse width. (a) Bipolar off/on switching in a successive deposited sample with a Cu:TCNQ thickness of 150 nm. (b) Unipolar switching to metallic like state. All measurements were carried out on the smallest top electrode areas.

Switching Time

The intrinsic switching time of Cu:TCNQ thin film cells is an important aspect regarding the possible application in memory devices. As described in section 2.3.4, the switching time is closely connected to the underlying physical mechanism. While Potember et al. reported switching times in the ns range for unipolar switching devices [14], Sato et al. observed minimum times of 2.5 ms for bipolar switching cells [80].

In the case of this study, the time characteristics of the resistive switching effect were measured using a custom-designed, computer controlled current-voltage measuring system. Thereby, a pulse cycle as shown in Fig. 4.17 was applied to the memory cells with the following parameters: $t_{\text{read}} = 100$ ms, $V_{\text{read}} = -0.5$ V, $V_{\text{write}} < V_{\text{th,off,on}}$, and $V_{\text{erase}} > V_{\text{th,on,off}}$. The pulse width of the write/erase pulses $t_{\text{write}} = t_{\text{erase}}$ was decreased from ms to μ s. The dependence of the resistance state from the pulse widths measured in this way is shown in Fig. 4.25.

The capacitance values and the resultant calculated time constants (in the μ s range) of the memory cells, which were determined in section 4.2.2, must be considered for these measurements. Hence, devices with smaller pad areas and therefore smaller capacitance values are necessary for measurements with shorter pulse lengths than described here.

The bipolar switching between off- and on-state is shown in Fig. 4.25 (a). The resistance states displayed no dependence on the write/erase pulse widths within the investigated range. The pulse width dependence of the unipolar switching to the metallic like state, which is described in detail section 4.2.1, was also studied. The measurement results are shown in Fig. 4.25 (b). The resistance states in this case also displayed no dependence on the write/erase pulse widths in the investigated range.

This measurement setup was also used to analyze the current responses on short voltage pulses as shown Fig. 4.26. Thereby, four different cases were examined. Starting in the off-state, a positive voltage pulse (no-switching, cell remained in off-state), and a

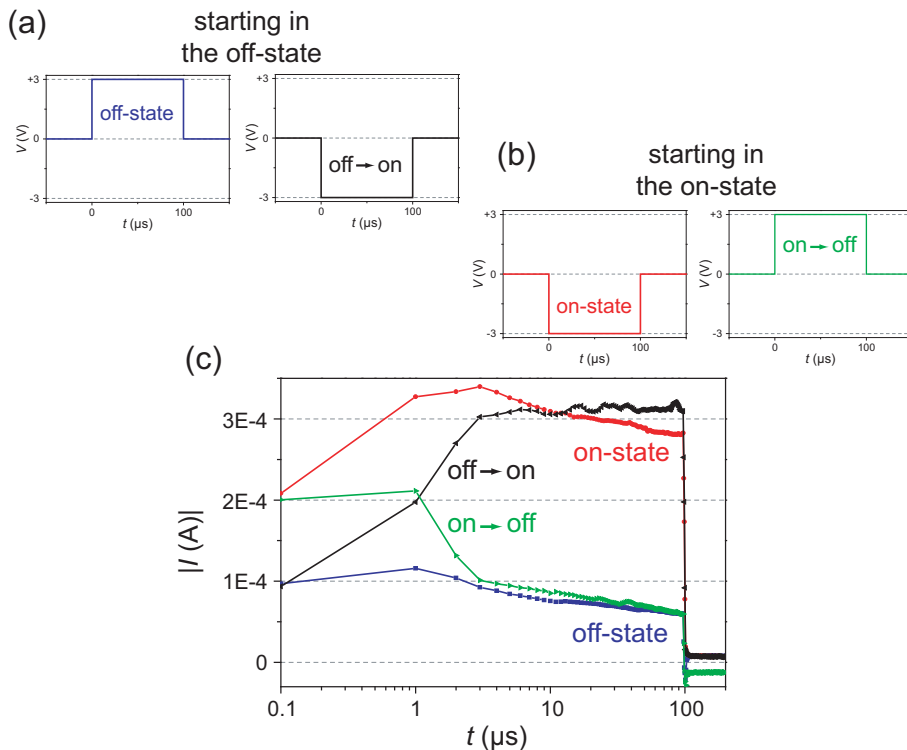


Figure 4.26: Current responses on voltage pulses. Applied voltage signal on memory cell, which was (a) prior in off-state, and (b) prior in on-state. (c) Measured absolute current response plotted over time (logarithmic) for the four cases.

negative voltage pulse (switching to the on-state) was applied, as shown in Fig. 4.26 (a). Starting in the on-state, a negative voltage pulse (no-switching, cell remained in on-state), and a positive voltage pulse (switching to the off-state) was applied, as shown in Fig. 4.26 (b).

The resulting absolute values of the current response for all four cases are plotted over the logarithmic time in Fig. 4.26 (c). Both switching cases, off → on and on → off occur within the accuracy of measurement. These results confirm the observations shown in Fig. 4.25, that the switching process in Cu:TCNQ thin films takes less than 2 μs.

4.2.4 Temperature Dependence

Measurements regarding the temperature dependence of the switching parameters were carried out using the Summit 9600 thermal probe station. The temperature dependencies of the current in the three conductance states (R_{met} , R_{on} , and R_{off}) were measured between -50°C and 70°C . The resulting characteristics are displayed in the Arrhenius plot shown in Fig. 4.27. These measurements were carried out on a successive evaporated device with a Cu:TCNQ thickness of 150 nm and an Al top

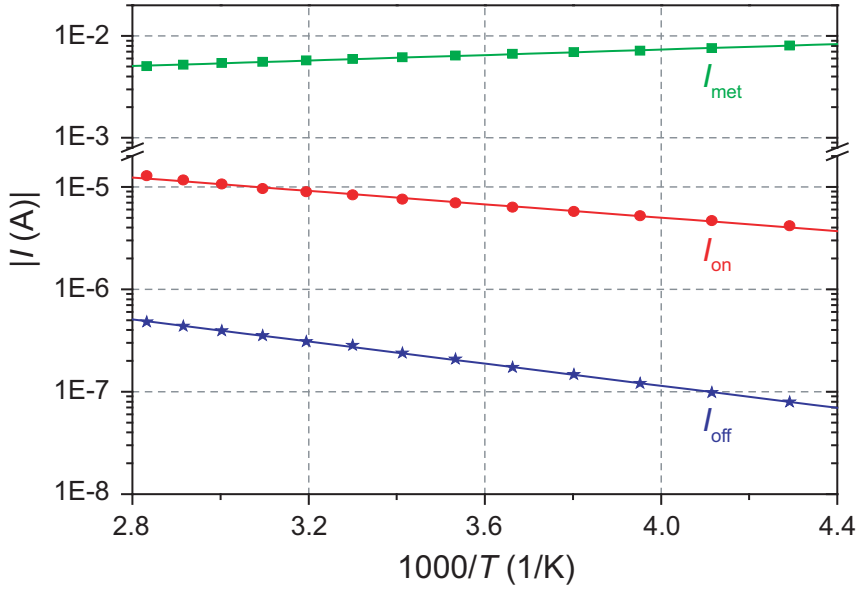


Figure 4.27: Temperature dependencies of the conductance states. The currents are plotted over the reciprocal temperature ($1000/T$) in an Arrhenius graph.

electrode diameter of 75 μm .

The current–temperature characteristic of the on– and off–state displayed a thermally activated behavior. In these cases, the activation energies ($W_{a,\text{on}}$ and $W_{a,\text{off}}$) can be calculated using the Arrhenius equation (Eq. 4.5), where A is a constant of proportionality, and k denotes the examined variable.

$$k = A \exp\left(-\frac{W_a}{k_B T}\right) \quad (4.5)$$

In this measurement, the variable is the electrical current ($k = I$). Using Eq. 4.5, the activation energies can be calculated to:

$$W_{a,\text{on}} = 0.07 \text{ eV}$$

$$W_{a,\text{off}} = 0.10 \text{ eV}$$

In contrast, the current–temperature characteristic of the metallic like state displayed a decrease of current with increasing temperature. In this case, the temperature coefficient at room temperature α_{20} of the resistance can be determined using the simple linear equation 4.6.

$$R(T) = R(T = 293 \text{ K})(1 + \alpha_{20}(T - 293 \text{ K})) \quad (4.6)$$

Using the measurement values displayed in Fig. 4.27, the temperature coefficient for the metallic like state can be calculated to:

$$\alpha_{20} \approx 4 \times 10^{-3} \text{ K}^{-1}$$

Material	Ag	Al	Au	Cu	Fe	Ni	Pb	Pt	Sn
$\alpha_{20}(10^{-3}/\text{K})$	3.6	4.3	3.8	4.3	6.5	6.0	3.9	3.5	4.3

Table 4.1: *Temperature coefficients of different metals [110].*

These value is in good accordance with the temperature coefficients of many metals as stated in Table 4.1. Therefore, these results indicate that the unipolar switching observed in some of the memory cells is possibly based on a metallic filamentary process, which is described in general in section 2.2.1.

4.3 Summary

The characterization of Cu:TCNQ thin film devices is described in this chapter. The physical characterization (UV-Vis, IR spectroscopy, XRD) confirmed the formation of a Cu:TCNQ CT-complex for both preparation methods.

The electrical characterization ($I(V)$ characteristics, impedance spectroscopy, pulse measurements, temperature dependence) yielded the following results:

- The memory cells were initially in a high resistance state
- No forming step was necessary prior to the resistive switching
- The capacitances were constant in off- and on-state ($C_{\text{off}} = C_{\text{on}}$)
- High capacitance values were measured for both preparation methods, somewhat higher for successive deposited devices ($C(A = 0.0398 \text{ mm}^2) = 500 \text{ pF}$) than for simultaneous ones ($C(A = 0.0398 \text{ mm}^2) = 350 \text{ pF}$)
- The capacitance was independent of the Cu:TCNQ thickness
- The devices exhibited bipolar switching with the following polarities:
 - On-switching occurred by application of a negative voltage to the Al top electrode
 - Off-switching occurred by application of a positive voltage to the Al top electrode
- The devices exhibited non-linear $I(V)$ characteristics in off- and on-state
- Switching characteristics for successive evaporated Cu:TCNQ:
 - The threshold voltages were normal distributed with the mean values:
 - * $V_{th, \text{off}, \text{on}} = -2.4 \text{ V}$
 - * $V_{th, \text{on}, \text{off}} = +1.6 \text{ V}$
 - No dependence of V_{th} on the pad area in the studied range ($0.0044 \text{ mm}^2 < A < 0.1963 \text{ mm}^2$)
 - Off-state resistance: mean value $R_{\text{off}} = 30 \text{ M}\Omega$, median value $R_{\text{off}} = 1 \text{ M}\Omega$
 - On-state resistance: mean value $R_{\text{on}} = 70 \text{ k}\Omega$, median value $R_{\text{on}} = 50 \text{ k}\Omega$
 - In the studied range of pad areas the resistance values displayed the following dependencies:
 - * R_{off} decreased with increasing pad size

- * R_{on} was independent of the pad size
- Switching characteristics for simultaneous evaporated Cu:TCNQ:
 - The fraction of memory cells, which exhibited resistive switching was significantly lower than the one for devices prepared by the successive method
 - The voltage thresholds were significantly higher and with a wider spread
 - The on-switching occurred at voltages in the range of $-11 \text{ V} \leq V_{th, \text{off}, \text{on}} \leq -6 \text{ V}$
 - The off-switching occurred at voltages in the range of $+1.5 \text{ V} \leq V_{th, \text{off}, \text{on}} \leq +10 \text{ V}$
 - The resistance values were roughly 100 times higher than for successive deposited devices
- The switching process in Cu:TCNQ thin films takes less than $2 \mu\text{s}$
- Up to 10000 switching cycles could be performed on some samples
- The current–temperature characteristic of the on– and off–state displayed a thermally activated behavior
- Some samples display an unipolar switching to a very low ohmic state ($R_{\text{met}} < 100 \Omega$) with a metallic like current over temperature behavior

5 Switching Mechanisms

As described in section 2.3.4, the underlying physical mechanism responsible for the resistive switching in Cu:TCNQ thin film devices is still under debate. The results of the basic characterization, which are reported in chapter 4, provide some meaningful information on the mechanism.

Resistive switching in amorphous Cu:TCNQ thin films could be demonstrated using XRD measurements (section 4.1.3) and electrical characterization methods (section 4.2.1). Therefore, the theory proposed by Heintz et al. [74], that a phase transformation between two polycrystalline states is responsible for the switching effect, can be discarded.

Furthermore, the measurements on the prepared memory cells proved the existence of two switching mechanisms in Cu:TCNQ thin film devices, an unipolar switching to a metallic like state, and a bipolar switching process (section 4.2.1) [107]. A discrimination between these different types of switching with quite diverse characteristics was not common in the literature.

The different dependencies of the resistance values in off- and on-state, which are described in section 4.2.3, indicate that the conduction in the off-state ($R \uparrow$ with $A \downarrow$) is a homogeneous distributed material property, while the conduction in the on-state ($R \neq f(A)$) is primarily caused by a local (filamentary) effect.

The impedance spectroscopy (section 4.2.2) demonstrated, that the memory cell structure cannot be regarded as a simple parallel plate capacitor, with Cu:TCNQ as a homogeneous dielectric sandwiched between two metal electrodes. The application of this model resulted in a dielectric constant of $\epsilon_r \approx 200$. In addition, the capacitance values of the memory cell seems to be independent of the Cu:TCNQ layer thickness according to the measurements. These results of the impedance spectroscopy indicate, that an interface layer must be considered, when analyzing the memory cell structure. Therefore, experiments with different electrode materials were carried out, in order to

Contents

5.1	Use of Different Electrode Materials	98
5.1.1	Devices with Al Top Electrodes	99
5.1.2	Devices with Pt Top Electrodes	100
5.1.3	Equivalent Circuits	102
5.1.4	TOF-SIMS Measurements	106
5.2	Control Experiments	108
5.3	Summary	109

Sample Setup	Electrical Parameters	
	Resistance States	Threshold Voltages
TE: Al BE: Cu	$R_{\text{off}} \approx 5 - 50 \text{ M}\Omega$ $R_{\text{on}} \approx 10 - 100 \text{ k}\Omega$	$V_{th,\text{off,on}} \approx -2.4 \text{ V}$ $V_{th,\text{on,off}} \approx +1.6 \text{ V}$
TE: Al BE: Au	$R_{\text{off}} \approx 1 - 10 \text{ M}\Omega$ $R_{\text{on}} \approx 5 - 50 \text{ k}\Omega$	$V_{th,\text{off,on}} \approx -3 \text{ V}$ $V_{th,\text{on,off}} \approx +1.5 \text{ V}$
TE: Al BE: Al	$R_{\text{off}} \approx 0.1 - 1 \text{ G}\Omega$ $R_{\text{on}} \approx 1 - 10 \text{ M}\Omega$	$V_{th,\text{off,on}} \approx -4.5 \text{ V}$ $V_{th,\text{on,off}} \approx +4 \text{ V}$
TE: Al BE: Pt	no switching, very high resistance values up to breakdown at high voltages ($> 12 \text{ V}$)	
TE: Au BE: Cu	no switching, all cells initially shorted	
TE: Pt BE: Cu	$R_{\text{off}} \approx 10 - 100 \text{ k}\Omega$ $R_{\text{on}} \approx 1 - 10 \text{ k}\Omega$	$V_{th,\text{off,on}} \approx +2.5 \text{ V}$ $V_{th,\text{on,off}} \approx -2 \text{ V}$
TE: Pt BE: Pt	$R_{\text{off}} \approx 100 \text{ k}\Omega$ $R_{\text{on}} \approx 10 \text{ k}\Omega$	$V_{th,\text{off,on}} \approx +1.5 \text{ V}$ $V_{th,\text{on,off}} \approx -1.5 \text{ V}$

Table 5.1: *Electrical Parameters of the Investigated Electrode Setups. (TE: top electrode, BE: bottom electrode).*

gain a better understanding of the proposed interface layer.

5.1 Use of Different Electrode Materials

Devices with different electrode materials (Al, Cu, Au, Pt) were prepared using the PVD methods, which are discussed in detail in section 3.3. Some general electrical parameters obtained using the electrical characterization tools described in section 4.2 are summarized in Table 5.1.

The different devices showed strongly diverse behaviors depending on the electrode materials. These experiments showed, that the top electrode material has a crucial impact on the electrical characteristics. Memory cells with aluminum top electrodes generally showed the smallest conductivity values of all tested setups. Resistive switching could be observed in combination with any of the tested bottom electrode materials besides Pt, which resulted in very high resistance values of the memory cells up to breakdown at high voltages.

Memory cells with noble metal top electrodes generally showed much higher conductivity values. Samples with Au top electrodes were all in an extreme low resistance state and displayed no resistive switching. This is possibly attributed to the migration of Au atoms during the top electrode evaporation process. Devices with Pt top electrodes exhibited bipolar resistive switching with opposite polarities regarding the threshold voltages and considerable lower resistance values.

The influence of the top electrode on otherwise identical memory cells will be

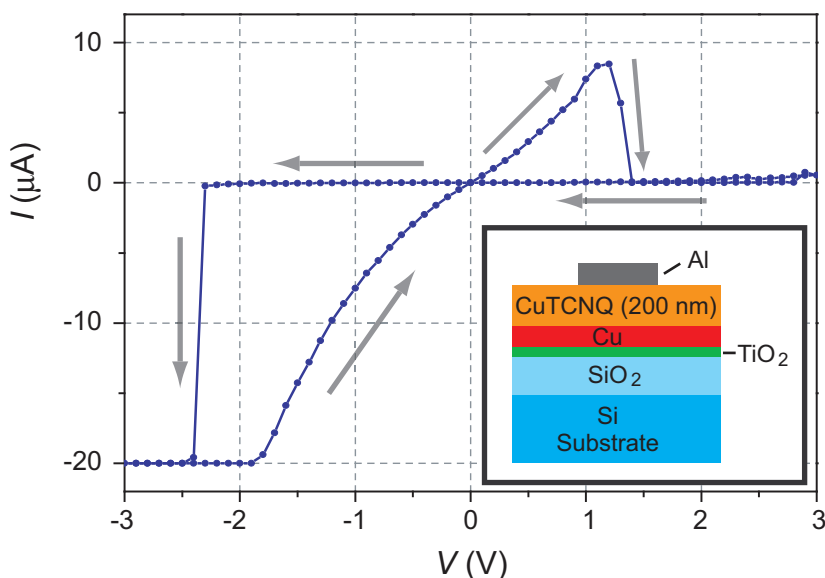


Figure 5.1: $I(V)$ plot of the successive deposited reference device (Cu:TCNQ thickness 200 nm) with Al top electrode. The parameters for this quasi static measurement were: nominal applied voltage cycle $0\text{ V} \Rightarrow -3\text{ V} \Rightarrow +3\text{ V} \Rightarrow 0\text{ V}$, voltage step width 100 mV, voltage step rate 10 Hz, current compliance 20 μA , sample rate 10 Hz.

described in the following. Thereby, devices with an identical film structure consisting of a successive deposited Cu:TCNQ layer with a thickness of 200 nm on top of a Cu bottom electrode served as reference systems. The design of the substrate holders in the evaporation chamber (3.2.3) made it possible to prepare two samples at a time in one process. One was then configured with an Al top electrode, and the other with a Pt top electrode.

5.1.1 Devices with Al Top Electrodes

Memory cells with a Cu bottom electrode and an Al top electrode exhibited the most stable and reproducible behavior. This is also by far the most common electrode setup published in the literature. The results of the electrical characterization are discussed in detail in section 4.2. Here, a typical $I(V)$ characteristic of a memory cell measured on the above described reference sample with an Al top electrode (pad diameter 150 μm , area 0.0177 mm^2) is shown in Fig. 5.1.

The reference samples were initially in the high resistance state and displayed a bipolar switching behavior. By application of a more negative voltage than the threshold voltage ($V_{th,off,on}$) to the Al top electrode the memory cell is switched abruptly to the low resistive state. The memory cell can be switched back by application of a positive voltage greater than $V_{th,on,off}$. In this case, the off/on resistance ratio is approximately 100. Temperature dependent measurements revealed a thermally activated conductance behavior for both the off- and on-state.

Both conductance states displayed a non linear current-voltage behavior as described

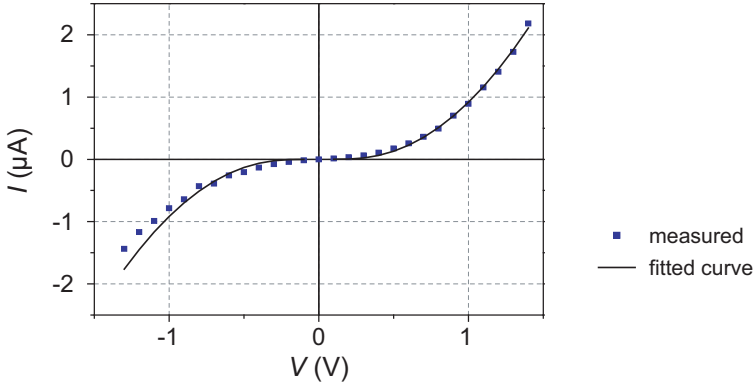


Figure 5.2: *Conductance process in the off-state. Current-voltage characteristic of the off-state for a successive deposited memory cells with a Cu:TCNQ thickness of 150 nm. The continuous black line indicates a fit of a Fowler-Nordheim tunneling process (see Eq. 5.1).*

in section 4.2.1. The conductance behavior for the off-state is separately displayed in Fig. 5.2. The blue points mark the measured values, while the continuous black lines indicate the fitted conductance model. Since a thin insulating interface layer is expected to form between the Cu:TCNQ and the Al top electrode and dominates the conductance behavior of the device, the $I(V)$ characteristic was fitted using the Fowler-Nordheim tunneling process described in Eq. 5.1. These tunneling mechanism can express the current density J_{FN} flowing through a thin insulating layer as a function of the applied voltage V [105, 106].

$$I_{\text{FN}} = P_{\text{FN}} V^2 \exp\left(-\frac{b}{V}\right) \quad \text{with } b = \text{const.} \cdot (\phi_B)^{\frac{3}{2}} \sqrt{m_{\text{ox}}^*} \quad (5.1)$$

Here, ϕ_B is the barrier height, and m_{ox}^* the effective mass of the insulator. The constants of the fit shown in Fig. 5.2 (a) were calculated to the values $P_{\text{FN}} = 1.608 \times 10^{-6} \text{ A/V}^2$, and $b = 0.56257 \text{ V}$. Hence, the current-voltage behavior in the off-state can be fitted closely by a tunneling mechanism.

5.1.2 Devices with Pt Top Electrodes

Resistive switching could be observed on samples with Pt top electrodes in combination with Cu and Pt bottom electrodes. The tested structures with their electrical parameters are summarized in Table 5.1. A typical $I(V)$ characteristic of a memory cell measured on a reference device with Pt top electrodes and a Cu bottom electrode is shown in Fig. 5.3. This characteristic differs significantly from the results for samples with Al top electrodes (Fig. 5.1).

The observed switching effect in this case is bipolar as was the case with Al top electrodes. However, the polarity of the switching effect is reversed with respect to the reference samples with Al top electrodes. By application of a more positive voltage than the threshold voltage ($V_{\text{th,on,off}}$) to the Pt top electrode, the memory cell could be switched gradually to the low resistance on-state. The device could be switched back

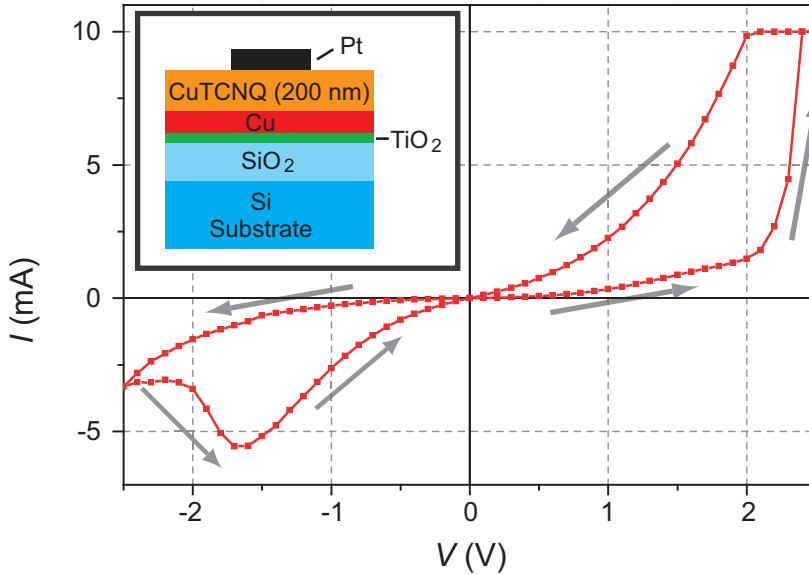


Figure 5.3: $I(V)$ plot of the successive deposited reference device (Cu:TCNQ thickness 200 nm) with Pt top electrode. The parameters for this quasi static measurement were: nominal applied voltage cycle $0\text{ V} \Rightarrow +2.5\text{ V} \Rightarrow -2.5\text{ V} \Rightarrow 0\text{ V}$, voltage step width 100 mV, voltage step rate 10 Hz, current compliance 10 mA, sample rate 10 Hz.

to the initial high resistance off-state by application of a more negative voltage than $V_{th,off,on}$.

The resistive switching in memory cells with Pt top electrodes occurred gradually and not abruptly as it does with Al top electrodes. This was further proven by an $I(V)$ cycling measurement with an increasing V_{write} voltage as shown in Fig. 5.4. It was possible to write in intermediate resistance states depending on the value of V_{write} .

The resistivity ($\rho_{TE,Pt,on} = 880\text{ }\Omega\text{cm}$, $\rho_{TE,Pt,off} = 8\text{ k}\Omega\text{cm}$) was at least 20 times lower than in the on-state of the reference device with Al top electrodes ($\rho_{TE,Al,on} = 180\text{ k}\Omega\text{cm}$, $\rho_{TE,Al,off} = 18\text{ M}\Omega\text{cm}$) and hence in much better accordance to results published by Melby et al. on bulk Cu:TCNQ [70]. He observed semiconducting properties with low resistivity values on synthesized Cu:TCNQ bulk crystals with a resistivity of $\rho_{Cu:TCNQ} = 200\text{ }\Omega\text{cm}$. The off/on ratio for the reference devices with Pt top electrode was therefore less than 10. Temperature dependent measurements revealed a thermally activated conductance behavior for both the off- and on-state.

Pulse measurements in the manner reported in section 4.2.3 were carried out on reference samples with Pt top electrodes with opposite polarities as previously described. Resistive switching with low off/on ratios (≈ 5) could be observed for standard measurements as shown in Fig. 5.5 (a). The resistance values in this case amounted to $R_{off} \approx 15\text{ k}\Omega$ and $R_{on} \approx 3\text{ k}\Omega$.

Another important difference compared to the reference samples with Al top electrodes is the fact, that the on-state stability is poor. By increasing the read time to $t_{read} = 60\text{ s}$ it could be observed, that the resistance asymptotically returns to the

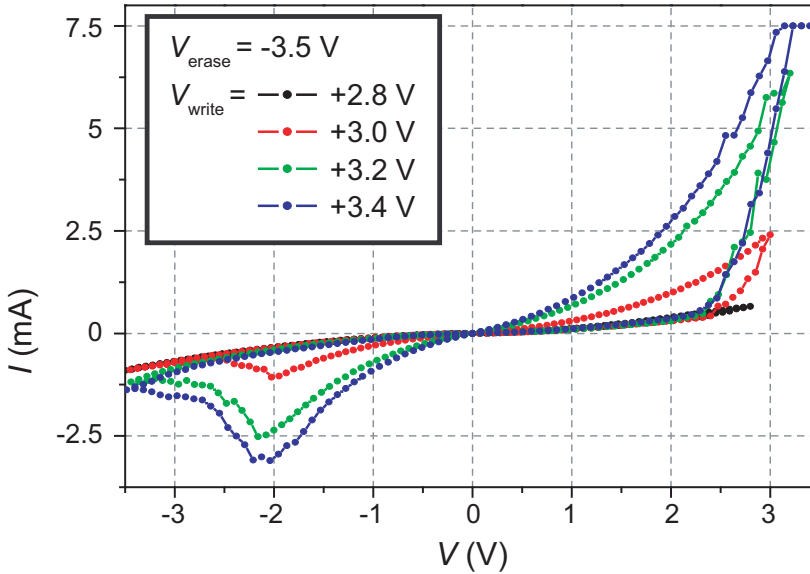


Figure 5.4: Plot of $I(V)$ subloops of the successive deposited reference device (Cu:TCNQ thickness 200 nm) with Pt top electrode. The parameters for this quasi static measurement were: nominal applied voltage cycle $0\text{ V} \Rightarrow V_{\text{write}} \Rightarrow -3.5\text{ V} \Rightarrow 0\text{ V}$, voltage step width 80 mV, voltage step rate 10 Hz, current compliance 7.5 mA, sample rate 10 Hz. The V_{write} voltage was increased from 2.8 V to 3.4 V in 200 mV steps.

off-state as shown in Fig. 5.5 (b). Furthermore, the on-state resistance R_{on} was strongly depending on the write pulse width t_{write} . This showed even at rather long write times as shown in Table 5.2.

Finally, impedance spectroscopic measurements in the manner reported in section 4.2.2 were carried out on the reference devices with Pt top electrodes. Memory cells with a top electrode diameter of 150 μm and thus an area of $A = 0.0177\text{ mm}^2$ exhibited a capacitance value of $C_{\text{off}} = C_{\text{on}} = 2\text{ pF}$, and resistance values of $R_{\text{off}} = 3\text{ k}\Omega$ and $R_{\text{on}} = 600\Omega$. Memory cells with the same pad size on the reference devices with Al top electrodes on the other hand had capacitances of $C_{\text{off}} = C_{\text{on}} = 100\text{ pF}$.

5.1.3 Equivalent Circuits

The comparison of the electrical characteristics of memory cells with Pt and Al top electrodes, which were otherwise identical, supported the idea that the interface to the

t_{write}	0.1 s	0.2 s	0.5 s	1 s	2 s	5 s
R_{on}	5.3 k Ω	4.9 k Ω	4.3 k Ω	2.5 k Ω	983 Ω	468 Ω

Table 5.2: Dependence of R_{on} on the write pulse width for reference samples with Pt top electrodes.

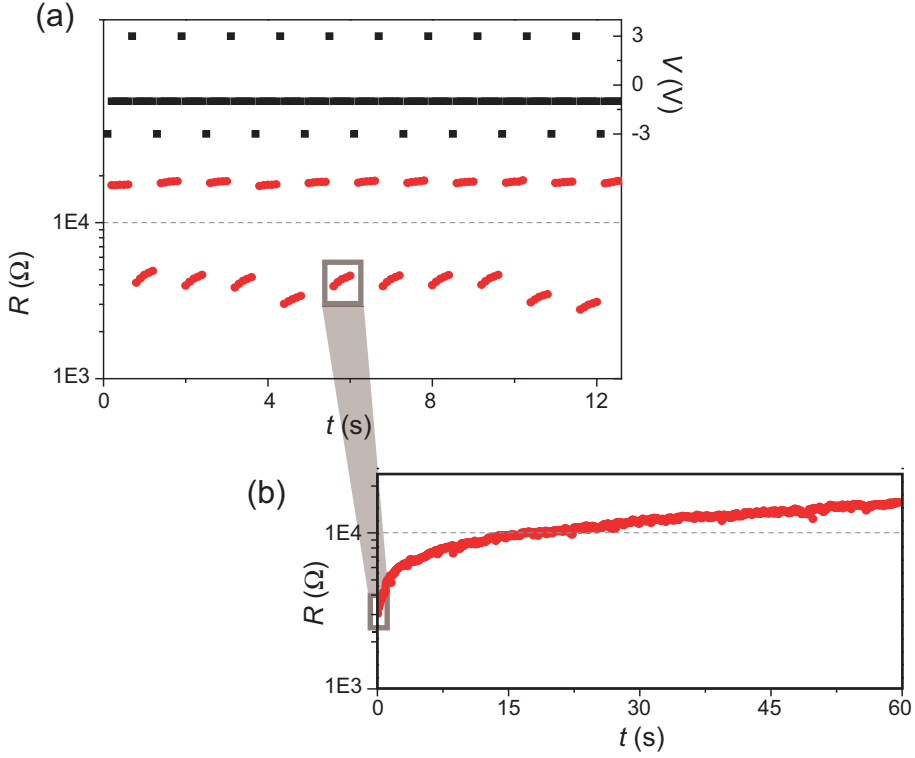


Figure 5.5: Pulse measurement on a reference sample with Pt top electrodes. The sample had a Cu:TCNQ thickness of 200 nm, a Cu bottom, and an Al top electrode (with 75 μm diameter). (a) Plot of $R(t)$ and $V(t)$ with measurement parameters: $V_{\text{write}} = +3\text{ V}$, $V_{\text{erase}} = -3\text{ V}$, $V_{\text{read}} = -1\text{ V}$, $t_{\text{write}} = t_{\text{erase}} = 200\text{ ms}$, $t_{\text{read}} = 0.8\text{ s}$. (b) Retention measurement of R_{on} for $t_{\text{read}} = 60\text{ s}$.

top electrode is decisively important regarding the impedance values and the resistive switching properties in Cu:TCNQ devices. In order to gain further knowledge of the nature of this interface layer, the memory cells were modeled by electrical equivalent circuits.

The memory cell impedance $Z_{\text{MC,Pt}}$ of memory cells with Pt top electrodes with an area of $A = 0.0177\text{ mm}^2$, as shown in Fig. 5.6 (a), can be described by a simple equivalent circuit. This circuit consists of a parallel connection of a capacitance C_{MC} and a changeable resistance R_{MC} as shown in Fig. 5.6 for off- (b) and on-state (c).

The values of the elements of the equivalent circuit can be set to $C_{\text{MC}} = 2\text{ pF}$, $R_{\text{MC,off}} = 3\text{ k}\Omega$, and $R_{\text{MC,on}} = 600\text{ }\Omega$ using the results of the impedance spectroscopy. The memory cell impedance $Z_{\text{MC,Pt}}$ of this simple equivalent circuit can therefore be described by the Eq. 5.2.

$$Z_{\text{MC,Pt}} = \frac{R_{\text{MC}}}{1 + \omega^2 R_{\text{MC}}^2 C_{\text{MC}}^2} - j \frac{\omega R_{\text{MC}}^2 C_{\text{MC}}}{1 + \omega^2 R_{\text{MC}}^2 C_{\text{MC}}^2} \quad (5.2)$$

The impedance of the memory cells with Al top electrodes (setup shown in Fig. 5.7 (a)) can be modeled using an extended form of the simple equivalent circuit described in

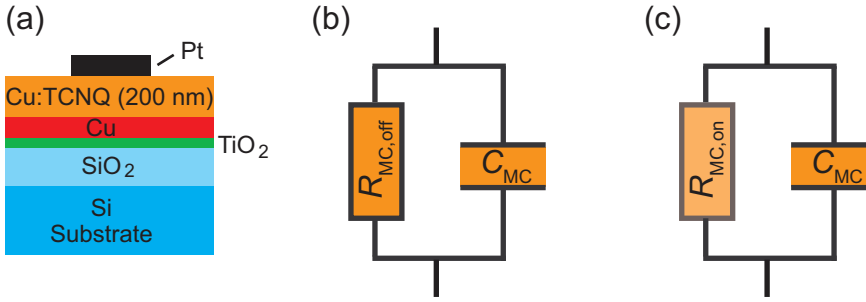


Figure 5.6: *Equivalent circuit for reference devices with Pt top electrodes. (a) Device setup. (b) Simple equivalent circuit in off-state. (c) Simple equivalent circuit in on-state.*

Eq. 5.2 and Fig. 5.6 (b),(c). A second RC–element is added to this circuit in series with the first one, as shown in Fig. 5.7 for the off– (b) and on–state (c).

One of the RC–elements represents the conducting, homogeneous Cu:TCNQ thin film (R_{TF} , C_{TF}) with the interface to the Cu bottom electrode. The other RC–element (R_{IF} , C_{IF}) represents the interface to the Al top electrode. For this model, the real and imaginary parts of the impedance $Z_{MC,Pt}$ can be calculated using Eq. 5.3 respectively Eq. 5.4.

$$\text{Re}\{Z_{MC,Al}\} = \frac{R_{TF}}{1 + \omega^2 R_{TF}^2 C_{TF}^2} + \frac{R_{IF}}{1 + \omega^2 R_{IF}^2 C_{IF}^2} \quad (5.3)$$

$$\text{Im}\{Z_{MC,Al}\} = \frac{\omega R_{TF}^2 C_{TF}}{1 + \omega^2 R_{TF}^2 C_{TF}^2} + \frac{\omega R_{IF}^2 C_{IF}}{1 + \omega^2 R_{IF}^2 C_{IF}^2} \quad (5.4)$$

This equivalent circuit model was then fitted to the results of the impedance spectroscopic measurements carried out on the reference samples with Al top electrodes in off–state (as shown in Fig. 5.8) and on–state (as shown in Fig. 5.9).

In these cases, the value of the RC–element representing the Cu:TCNQ thin film was set as an approximation to the one of the reference sample with Pt electrodes. Thereby, the value of the resistor (R_{TF}) was set to the value of the off–state resistance $R_{TF} = R_{MC,off} = 3 \text{ k}\Omega$ because this is the initial, stable state of these cells. Furthermore in the case of the extended model shown in Fig. 5.7, the applied voltage is divided over both RC–elements, and therefore this results in $V \ll V_{th,off,on}$ for the thin film element due to the much higher resistivity of the interface. The capacitor element is accordingly set to $C_{TF} = C_{MC} = 2 \text{ pF}$.

By using this approximation, the interface parameters (R_{IF} , C_{IF}) can be determined for both states by a fit of the equations to the measured curves of the impedance spectroscopy. These fitted curves for both, the real and imaginary part of the impedance spectrum are shown in Fig. 5.8 for the off– and in Fig. 5.9 for the on–state. The parameters according to these fits could be calculated to $R_{IF,off} = 12 \text{ M}\Omega$ for the off–state and $R_{IF,on} = 23 \text{ k}\Omega$ for the on–state. The value of the capacitor is constant in both states at $C_{IF} = 104 \text{ pF}$.

Calculated with the assumption of a parallel plate capacitor model, this results in a quotient of $\epsilon_{r,IF,TE}/d_{IF,TE} = 0.52 \text{ nm}^{-1}$ for the unknown thickness and dielectric

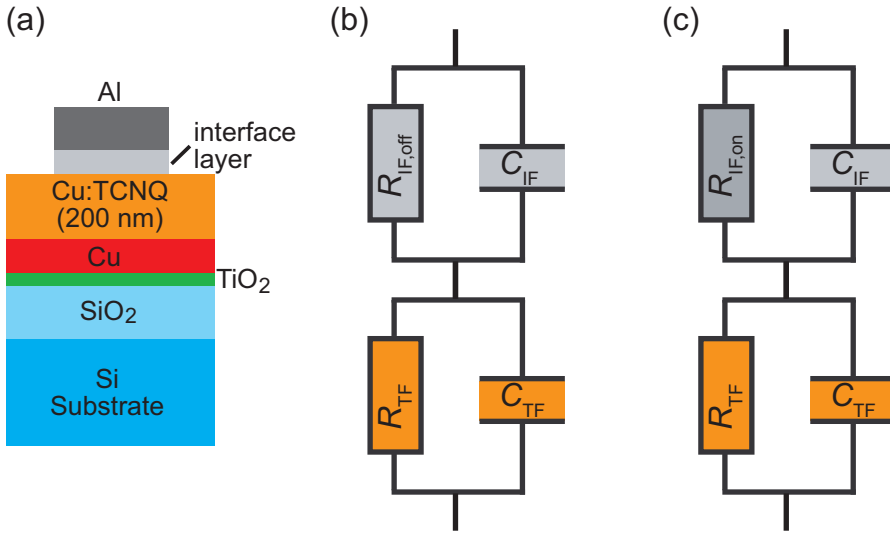


Figure 5.7: Equivalent circuit for reference devices with Al top electrodes. (a) Device setup. (b) Equivalent circuit in off-state. (c) Equivalent circuit in on-state.

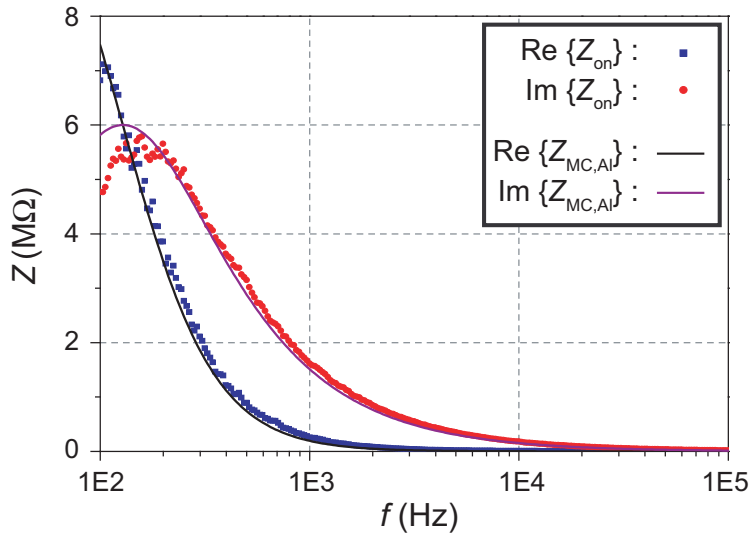


Figure 5.8: Impedance spectroscopy of reference devices with Al top electrodes in off-state. Measured values of real and imaginary part of Z_{off} (scatter) and fitted equivalent circuit model (line).

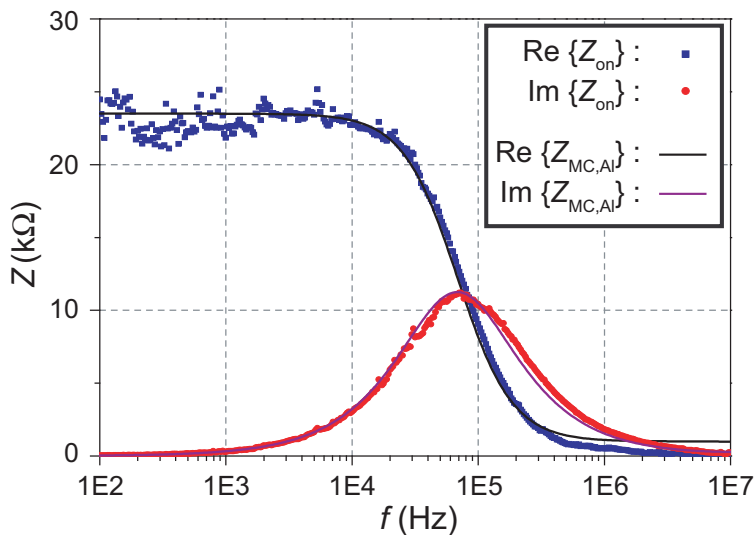


Figure 5.9: Impedance spectroscopy of reference devices with Al top electrodes in on-state. Measured values of real and imaginary part of Z_{on} (scatter) and fitted equivalent circuit model (line).

constant of the interface. The result calculates to an interface layer of a few nanometer thickness and a dielectric constant between 1.5 and 3. These values match to an interface layer of naturally oxidized aluminum between Cu:TCNQ and the aluminum top electrode. This Al oxide film may be formed by oxygen adsorbed and entrapped by the Cu:TCNQ layer and the ex-situ deposition of the Al, which is the typical process of the Cu:TCNQ cells reported in the literature.

These results are in good accordance to previously published results on resistive switching in rose bengal molecular devices [64]. The switching in these devices is attributed to the formation of a thin aluminum oxide layer between the top electrode and molecular layer. Coelle et al. proposed a similar mechanism for spin-coated polymeric films [65].

5.1.4 TOF–SIMS Measurements

The results presented in the previous sections proved, that a thin interface layer between the Cu:TCNQ layer and the Al top electrode is dominating the properties of the standard memory cells. The applied voltage is impressed almost exclusively on the interface layer due to the much higher impedance of the interface layer. Additional TOF (time of flight) SIMS (secondary ion mass spectroscopy) measurements were performed on the reference samples with Al and Pt top electrodes in order to study the nature of the thin interface layer.

In general, TOF–SIMS measurements are used to analyze the composition of solid surfaces and thin films. This technique is based on the sputtering of the surface to be investigated with a focused primary ion beam. The ejected secondary ions are collected and analyzed using a mass spectrometer to determine the elemental, isotopic,

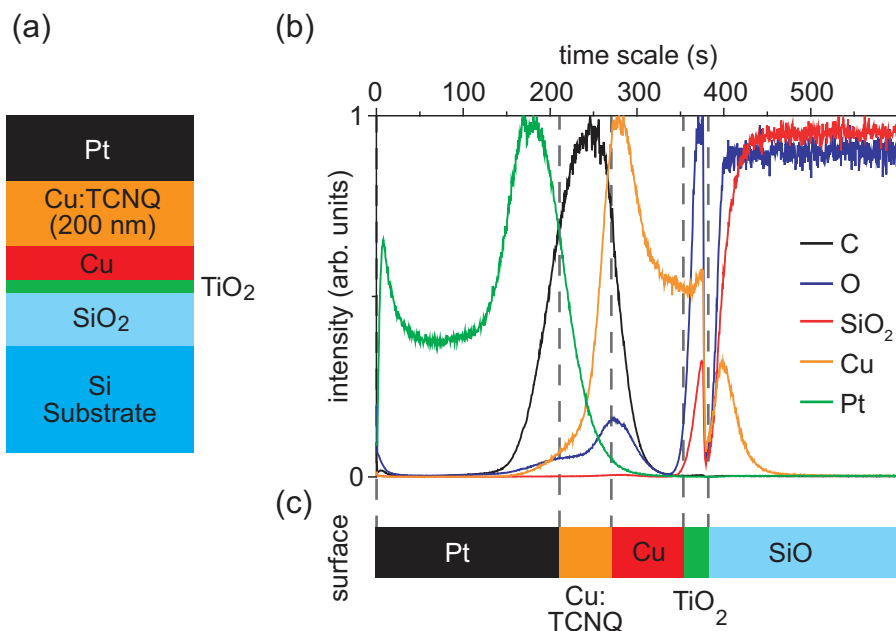


Figure 5.10: TOF-SIMS Measurement of Reference Device with Pt Top Electrode. (a) Device setup. (b) TOF-SIMS measurement. (c) Qualitative allocation of the data to the layer structure.

or molecular composition of the surface.

The results of a TOF-SIMS measurement on a reference sample with a continuous Pt top electrode is shown in Fig. 5.10. The setup of the device is displayed in Fig. 5.10 (a). The intensity of some selected elements/molecules is shown in arbitrary units over time in Fig. 5.10 (b). This graph does not allow for a quantitative interpretation regarding the thickness of the particular layers. However, the results can be qualitatively allocated to the corresponding layer in the sample structure as shown in Fig. 5.10 (c).

A comparison of this result with the TOF-SIMS measurement carried out on a reference device with a continuous Al top electrode (setup shown in Fig. 5.11 (a)) pinpoints interesting differences. In the case of the Pt top electrode, the intensity plot confirms the expected structures without distinctive features. The results of the measurements on the sample with Al top electrode (shown in Fig. 5.11 (b)) are more or less identical from the SiO₂ up to the Cu:TCNQ layer. However, interesting are the interfaces of the top electrode. The blue line counts the number of oxygen hits. In Fig. 5.11 (b), high amounts of oxygen are detected at both interfaces of the Al top electrode. A naturally formed aluminum oxide layer is expected to form on top of the Al due to the exposure to air. The similar oxygen peak at the interface to the Cu:TCNQ indicates the existence of a comparable oxide layer at this interface. The corresponding layer structure is graphically outlined in Fig. 5.11 (c).

The TOF-SIMS measurements confirm, that the existence of a thin oxide layer between the Cu:TCNQ and the top electrode is the difference between the reference samples with Al and Pt top electrodes and therefore responsible for the distinctive

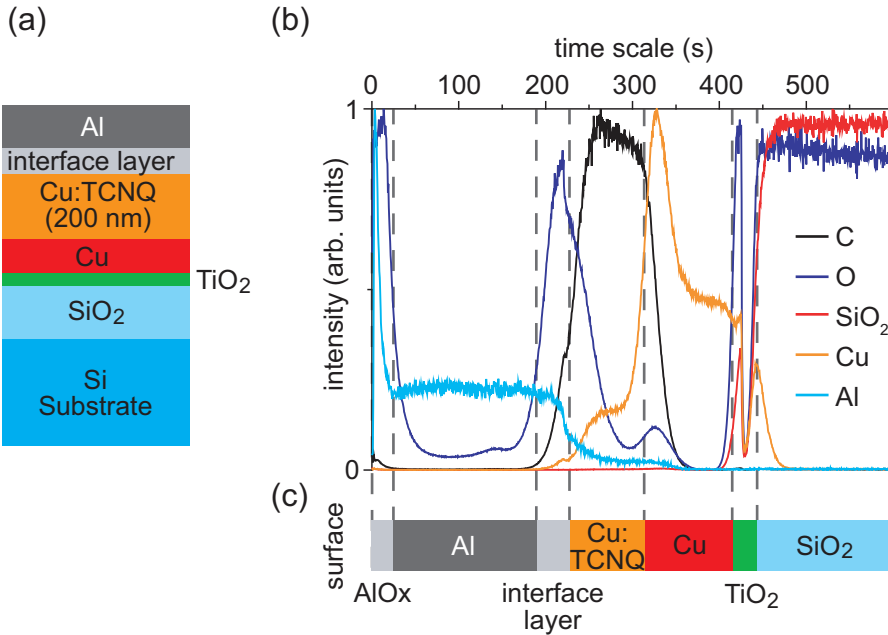


Figure 5.11: TOF-SIMS Measurement of Reference Device with Al Top Electrode. (a) Device setup. (b) TOF-SIMS measurement. (c) Qualitative allocation of the data to the layer structure.

different electrical characteristics described in section 5.1.

5.2 Control Experiments

To verify the assumption that the resistive switching occurs in a thin, interfacial Al oxide layer, comparison samples without Cu:TCNQ were fabricated. These devices consist of only a thin ≈ 4 nm aluminum oxide film between the electrodes. The device setup is shown in the inset of Fig. 5.12.

The aluminum bottom electrode was sputtered through a shadow mask on top of a continuous Pt layer. The surface of the aluminum was then oxidized under controlled conditions by UV treatment in an oxygen atmosphere (50 mbars). Finally the Cu top electrodes were sputtered. The whole deposition process was carried out in-situ in a cluster tool.

A typical resulting current-voltage characteristic is shown in Fig. 5.12. In this case, the thickness of the Al oxide was ≈ 4 nm, and the top electrode had a pad diameter of $150 \mu\text{m}$ ($A = 0.0177 \text{ mm}^2$). The resulting $I(V)$ characteristic is remarkably similar to the ones of Cu:TCNQ devices. This is evident when compared to the current-voltage characteristic measured on the reference sample with Al top electrodes, which is shown in Fig. 5.1. The polarity of the resistive switching is reversed due to the inverted electrode setup (BE: Al, TE: Cu). The resistance values for off- ($R_{\text{off}} = 10 \text{ M}\Omega$) and on-state ($R_{\text{off}} = 20 \text{ k}\Omega$) were in good agreement with the ones measured for the Cu:TCNQ

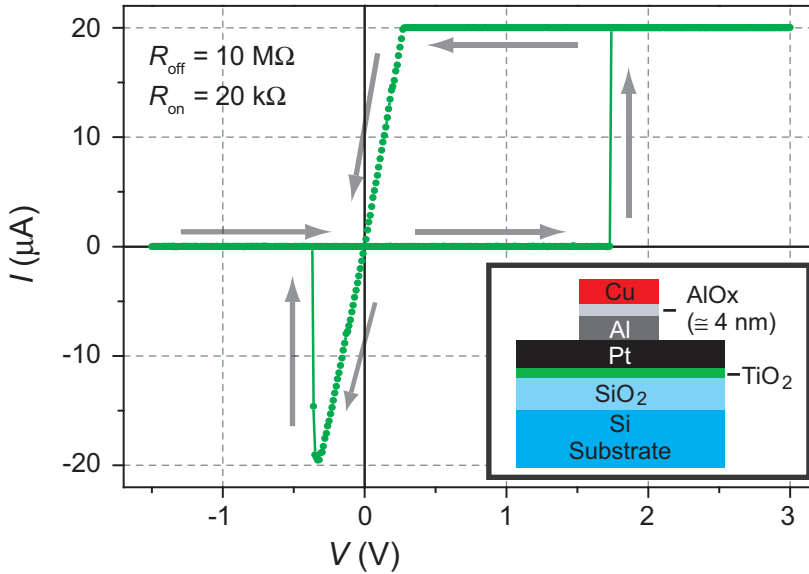


Figure 5.12: $I(V)$ plot of the comparison sample with AlOx layer (thickness $\approx 4 \text{ nm}$) with Cu top electrodes. The parameters for this quasi-static measurement were: nominal applied voltage cycle $0 \text{ V} \Rightarrow +3 \text{ V} \Rightarrow -1.5 \text{ V} \Rightarrow 0 \text{ V}$, voltage step width 20 mV , voltage step rate 10 Hz , current compliance $20 \mu\text{A}$, sample rate 10 Hz .

devices with Al top electrodes as reported in section 4.2.3. The switching threshold voltages were generally somewhat lower, especially for the switching to the off-state ($V_{th,on,off}$). This could be due to the previously mentioned (section 5.1.3) division of the applied voltage over the Cu:TCNQ part and the interface layer.

Additional electrical measurements confirmed the similarities between both types of devices. Impedance spectroscopic measurements displayed capacitance values of $C_{\text{AlOx}}(A = 0.0177 \text{ mm}^2) \approx 120 \text{ pF}$ compared to $\approx 130 \text{ pF}$ for the Cu:TCNQ devices with Al top electrodes as described in section 4.2.2. Furthermore, the measurements indicated that the off-state resistance decreases with increasing pad size, while the on-state seemed to be independent of the area. The switching threshold voltages displayed no pad size dependency. These results are consistent with the ones for the Cu:TCNQ devices with Al top electrodes as described in section 4.2.

Some pulse (endurance) measurements were also carried out on the comparison samples. It showed, that these devices displayed a lower switching stability (< 50 cycles) than the Cu:TCNQ memory cells. Furthermore the percentage of resistive switching cells per sample were considerably lower.

5.3 Summary

The measurements on devices with different electrode materials proved, that the interface to the Al top electrode dominates the behavior in the standard cells. Memory cells with Pt top electrodes displayed at least a 20 times better conductivity than ones

with Al electrodes. However, samples with Cu:TCNQ and Pt top electrodes also displayed some kind of resistive switching effect. This effect can be observed as a weak, time dependent hysteretic $I(V)$ behavior with distinctive different characteristics (also bipolar but with inverse polarity, much better conductivity in both states, less abrupt switching, much lower off/on ratio, shorter retention).

It is important to note, that the on-switching in standard cells occurs for a negative voltage polarity applied to the Al electrode in all cases. This is well known for resistively switching electrochemical metalization cells and reflects the drift of Cu ions through the amorphous aluminum oxide layer, the cathodic reduction, and growth of Cu filaments toward the anode [111–113]. Due to the presented results here, it is suggested, that in the standard Cu:TCNQ memory cells with Al top electrodes, the aluminum oxide represents the electrolyte which mediates a Cu ion based electrochemical switching [114]. This theory was later supported by different experiments carried out by Billen et al. [115].

In conclusion, the results of the conducted experiments allowed to discard many of the proposed switching mechanisms presented in section 2.3.4 for Cu:TCNQ devices with Al top electrodes. Furthermore, they confirmed earlier reports [81, 93] which stated the importance of the interface to the electrodes for the resistive switching effect. The model, which was previously proposed for some other resistive switching organic memory devices [64, 65], and states that a thin interfacial aluminum oxide layer at the Al electrode plays a decisive role, is confirmed for Cu:TCNQ cells. This theory is supplemented by additional experiments which indicate that the switching effect in Cu:TCNQ thin film devices could be a Cu ion based electrochemical effect, i.e., the devices could be described as electrochemical metalization cells, where the aluminum oxide represents the electrolyte. The Cu:TCNQ layer appears to be a suitable spacer, which possibly stabilizes the reversible switching by acting as a Cu ion buffer.

6 Conclusions

6.1 Summary

Recently, there has been a growing interest in alternative non-volatile memory technology concepts for massive data storage, which have the potential to eventually replace NOR and later NAND Flash in 32 nm technologies and below. The emerging NVRAM concepts have to be competitive regarding the performance characteristics (write/erase times, operating voltages, cycling endurance, etc.) and most importantly cost efficiency. This means, better scaling capabilities than Flash are imperative. In order to assess the potential of the various concepts, a sound understanding of the underlying mechanisms, prospects, and limitations are a necessity.

The main aim of this thesis has been the improvement of the physical understanding of the resistive switching effect in Cu:TCNQ thin films. An established and widely accepted theory to the switching mechanisms in Cu:TCNQ has still been missing, despite published work of several groups on this topic.

The standard deposition method for Cu:TCNQ thin films is a wet chemical process. However, this process results in a spontaneous growth of large crystallites, which is hard to control and difficult to implement for thin film devices. Therefore, the **design and construction of a high vacuum evaporation chamber for the thermal deposition of Cu:TCNQ thin films** was carried out. The system consists basically of two independent thermal evaporation sources, one for Cu and other electrode metals, and one for organic material (TCNQ). These sources were set up to be operated simultaneously or separately, controlled by a shutter system. The temperature control of the sources and the substrate is carried out semi-automatic via thermocouples which are connected to process controllers. These controllers in turn regulate the resistance heater power supplies. A control of the evaporation rates was made possible by the use of a QCM measuring unit.

On the basis of the constructed evaporation chamber, **two different deposition routes were developed and optimized**. The successive method is based on the evaporation of TCNQ on top of a Cu layer, and the execution of an annealing step in order to form the CT complex Cu:TCNQ. The resulting thin films displayed a very rough

Contents

6.1	Summary	111
6.2	Outlook	113

structure consisting of long columns oriented perpendicular to the substrate surface. The simultaneous method is based on the synchronous evaporation of TCNQ and Cu in the stoichiometric ratio. This process allows the usage of different bottom electrode materials and does not require an annealing step. The resulting thin films displayed a considerably more densely packed and uniform structure with a greatly reduced surface roughness.

Test structures for the electrical characterization were designed and fabricated. These devices consist of simple, capacitor like memory cells with a continuous bottom electrode, a continuous Cu:TCNQ layer, and structured, pad size top electrodes. Using the developed deposition processes, memory cells with areas between 0.7854 mm^2 and 0.0044 mm^2 , and Cu:TCNQ layer thicknesses between 400 nm and 70 nm were fabricated. Standard, reference cells were made with Cu bottom electrodes and Al top electrodes. Further experimental cells were fabricated using combinations of Al, Au, Cu, and Pt electrodes.

The **physical characterization** (spectroscopy, XRD, SEM) of the Cu:TCNQ thin films proved the formation of the CT-complex for both, the successive and the simultaneous, preparation methods. The **electrical characterization** of the fabricated reference memory cells confirmed a measurable resistive switching effect for both deposition routes. The reference devices exhibited bipolar switching, on-switching occurred by application of a negative voltage, while off-switching occurred by application of a positive voltage to the Al top electrode. The memory cells were initially in a high resistance state, and no forming step was necessary prior to the resistive switching. The memory cells exhibited non-linear $I(V)$ characteristics in off- and on-state. The current-temperature characteristics of the on- and off-state displayed a thermally activated behavior. It was shown, that the switching process in Cu:TCNQ thin films takes less than $2 \mu\text{s}$.

It was demonstrated, that the memory cells prepared by the successive method with a higher Cu:TCNQ surface roughness exhibit better switching characteristics than the smoother ones prepared by the simultaneous process. In detail they showed: lower switching thresholds, higher fraction of working memory cells, better cycling endurance, and better retention times.

The electrical characterization resulted in promising parameters for successive evaporated Cu:TCNQ devices. The switching threshold voltages could be reduced to mean values of $V_{th,off,on} = -2.4 \text{ V}$, and $V_{th,on,off} = +1.6 \text{ V}$. High off/on ratios were achieved with mean values of $R_{off} = 30 \text{ M}\Omega$, and $R_{on} = 70 \text{ k}\Omega$. Up to 10000 switching cycles could be performed on those simple pad size devices.

Valuable contributions regarding the physical origins of the **switching mechanism** could be extracted from the results of the electrical and physical characterization. It was shown, that the capacitance values were constant in off- and on-state ($C_{off} = C_{on}$), and too high for a simple metal/dielectric/metal system. Furthermore, the capacitance of the devices were independent of the Cu:TCNQ thickness. Therefore, the existence of a thin interface layer was assumed. Measurements on devices with different electrode materials proved this assumption. Memory cells with noble metal top electrodes displayed a distinctive different behavior with much lower resistance values and only a weak, time dependent hysteretic $I(V)$ behavior. It was shown, that the electrical characteristics of the reference cells were dominated by the interface layer to the Al top electrode. TOF-SIMS measurements confirmed the existence of an Al oxide

interface layer. The observed differences in the electrical characteristics of successive and simultaneous prepared memory cells are probably due to their different Cu:TCNQ roughness, which influences the growth of the Al oxide layer and its characteristics, and therefore the switching parameters.

The impedance spectroscopic measurements in off- and on-state could be fitted using an **equivalent circuit model**, which accounted for the interface layer. **Comparison samples** without a Cu:TCNQ layer (Al/AlO_x/Cu) were prepared and showed remarkably similar current voltage characteristics.

The measurements displayed, that the on-switching in all cases occurs for a negative voltage polarity applied to the Al electrode. This is well known for resistively switching **electrochemical metalization cells** and reflects the drift of Cu ions through the amorphous aluminum oxide layer, the cathodic reduction, and growth of Cu filaments toward the anode. Due to the here presented results it is suggested, that in the standard Cu:TCNQ memory cells with Al top electrodes, the aluminum oxide represents the electrolyte which mediates a Cu ion based electrochemical switching. The Cu:TCNQ layer appears to be a suitable spacer, which possibly stabilizes the reversible switching by acting as a Cu ion buffer.

6.2 Outlook

While this study presented a fundamental model regarding the underlying switching mechanisms in Cu:TCNQ thin film devices, and memory cells with promising electrical characteristics, there still remain open questions, especially concerning the embeddability in highly integrated memory applications. Further studies are necessary regarding the structuring of Cu:TCNQ and compatibility to lithographic processes. On the basis of such an improved process, smaller structures could be prepared. These are necessary, in order to reduce the device capacitance and therefore allow for an electrical characterization at higher frequencies. Furthermore, smaller memory cells would allow for a better evaluation of the scaling capabilities.

Appendices

List of Figures

1.1	Flow-Chart Displaying the Thesis Overview	4
2.1	Overview Memory Technologies	9
2.2	Principle Behavior of a Ferroelectric Capacitor	11
2.3	Schematic Mode of Operation of a FeFET	13
2.4	Schematic of a SONOS Memory Cell	14
2.5	Schematic of a Phase Change Memory Cell	16
2.6	Classification of Switching Characteristics	18
2.7	Filamentary Conduction in MIM Structures	19
2.8	Schematics of the Cation Movement in a PMC	21
2.9	Possible Configurations of the D-A Molecules in a CT Complex	24
2.10	Chemical Structure of the TCNQ Molecule	25
2.11	SEM Images of the Different Morphologies of Cu:TCNQ thin films	26
2.12	Schematic Drawing of the Orientation of TCNQ ⁻ in Cu:TCNQ	27
2.13	Views of Interpenetrating Networks in Cu:TCNQ Crystals	27
2.14	Conductivity in a CT Complex with Complete Charge Transfer	28
2.15	Conductivity in a CT Complex with Partial Charge Transfer	29
2.16	Schematic View of the Photoinduced Phase Transition in CT Complexes	31
3.1	Mean Free Path λ as Function of Pressure	36
3.2	Overview Setup Vacuum Chamber	38
3.3	Overview Vacuum Chamber Base Plate	39
3.4	Schematic Overview of the Interiors of the Vacuum Chamber	42
3.5	Control Elements of the Vacuum Chamber	46
3.6	Manual Shutter Controls	47
3.7	Control of the Cooling Water Flow	47
3.8	Schematic of the Measurement and Control Circuits of the System	49
3.9	Flow Chart for the Successive Evaporation Process	51
3.10	SEM Images of the Successive Annealing Series (0 s @ 125 °C)	54
3.11	SEM Images of the Successive Annealing Series (15 s @ 125 °C)	54
3.12	SEM Images of the Successive Annealing Series (30 s @ 125 °C)	55
3.13	SEM Images of the Successive Annealing Series (45 s @ 125 °C)	55
3.14	SEM Images of the Successive Annealing Series @ 100 °C and 150 °C	56
3.15	SEM Images of in-situ Annealed Samples	57
3.16	SEM Images of Successive Deposited Samples at Elevated Temperatures	57
3.17	Schematic of the Gas Phase Mixing During the Simultaneous Process	58
3.18	Flow Chart for the Simultaneous Evaporation Process	59
3.19	SEM Images of Simultaneous Deposited Samples	62
3.20	SEM Images of Thickness Series of Simultaneous Deposited Samples	63
3.21	Typical Device Setup for the Successive Evaporation Process	64
3.22	SEM Images of Al Top Electrodes on Cu:TCNQ	64

3.23	Typical Device Setup for the Simultaneous Evaporation Process	65
3.24	Top View of a Device with a Top Electrode Structured by a Shadow Mask	66
3.25	SEM Images of Wet-Chemical Etching of Cu:TCNQ	67
3.26	SEM Images of the Surface of Simultaneous Evaporated Cu:TCNQ	67
3.27	Crossbar Device Structure	68
4.1	UV-Vis Absorption Spectrum of Successive Deposited Cu:TCNQ	70
4.2	UV-Vis Absorption Spectrum of Simultaneous Deposited Cu:TCNQ	71
4.3	IR Reflectance Spectra of Cu:TCNQ Layers	72
4.4	XRD Measurements on Different Types of Samples	73
4.5	Exemplary Current-Voltage Characteristic Plotted over Time	75
4.6	Exemplary Linear and Logarithmic Current over Voltage Plots	75
4.7	$I(V)$ Plots for a 150 nm Successive Deposited Cu:TCNQ Layer	76
4.8	$I(V)$ Plots for a 200 nm Successive Deposited Cu:TCNQ Layer	77
4.9	Histogram of the Switching Thresholds for Successive Deposited Devices	78
4.10	$I(V)$ Plots for a 200 nm Successive Deposited Cu:TCNQ Layer	79
4.11	$I(V)$ Plots for a 150 nm Simultaneous Deposited Cu:TCNQ Layer	80
4.12	$I(V)$ Plots for a 100 nm Simultaneous Deposited Cu:TCNQ Layer	80
4.13	Unipolar Switching to a Metallic Like State	81
4.14	Exemplary Impedance Spectroscopy Measurement	83
4.15	Top Electrode Area Dependence of the Capacitance	83
4.16	Cu:TCNQ Thickness Dependence of the Capacitance	84
4.17	Exemplary Applied Voltage Signal for a Pulse Cycle	85
4.18	Pulse Measurement on a Successive Deposited Memory Cell	86
4.19	Histogram of the Off- and On-State Resistances	87
4.20	Plot of the Off- and On-State Resistance Values vs. Pad Size.	87
4.21	Pulse Measurement on a Simultaneous Deposited Memory Cell	88
4.22	$R(t)$ Plots of the Failure Types Occurring During Pulse Measurements	89
4.23	Retention Measurement on a Successive Deposited Device	90
4.24	Endurance Measurement on a Successive Deposited Device	90
4.25	Resistance States Dependence on the Write/Erase Pulse Width	91
4.26	Current Responses on Voltage Pulses	92
4.27	Temperature Dependencies of the Conductance States	93
5.1	$I(V)$ Plot of the Reference Device with Al Top Electrode	99
5.2	Conductance Process in the Off-State	100
5.3	$I(V)$ Plot of the Reference Device with Pt Top Electrode	101
5.4	Plot of $I(V)$ Subloops of the Reference Device with Pt Top Electrode	102
5.5	Pulse Measurement on a Reference Sample with Pt Top Electrodes	103
5.6	Equivalent Circuit for Reference Devices with Pt Top Electrodes	104
5.7	Equivalent Circuit for Reference Devices with Al Top Electrodes	105
5.8	Impedance Spectroscopy of Reference Devices with Al TE in Off-State	105
5.9	Impedance Spectroscopy of Reference Devices with Al TE in On-State	106
5.10	TOF-SIMS Measurement of Reference Device with Pt Top Electrode	107
5.11	TOF-SIMS Measurement of Reference Device with Al Top Electrode	108
5.12	$I(V)$ Plot of Comparison Sample with AlOx Layer	109

List of Tables

2.1	Projected Properties of Competing Memory Technologies	10
2.2	Projected Properties of Emerging Memory Technologies	17
2.3	Excerpt of Published Switching Parameters for Cu:TCNQ Devices . . .	30
3.1	Comparison of Deposition Methods for Cu:TCNQ	35
3.2	Occupation of Base Plate Ports	40
3.3	QCM Parameters for Cu and TCNQ	44
3.4	Annealing Series Parameters for Successive Deposited Cu:TCNQ . . .	53
3.5	Substrate Temperature Series for the Simultaneous Deposition	61
3.6	Pad Diameters and Areas of the Top Electrode	65
4.1	Temperature Coefficients of Different Metals	94
5.1	Electrical Parameters of the Investigated Electrode Setups	98
5.2	Dependence of R_{on} on the Write Pulse Width for Pt Top Electrodes . . .	102

Bibliography

- [1] G. E. Moore. Cramming more components onto integrated circuits. *Electronics*, 38, 1965.
- [2] G. E. Moore. No exponential is forever: but "Forever" can be delayed! [semiconductor industry]. In *Proceedings of IEEE International Solid-State Circuits Conference, San Francisco, CA, USA, 09/02/2003-13/02/2003*, volume 1, pages 20–3. Piscataway, NJ, USA: IEEE, 2003.
- [3] R. Waser. *Nanoelectronics and Information Technology*. Wiley - VCH, 2003.
- [4] F. Masuoka, M. Momodomi, Y. Iwata, and R. Shirota. New ultra high density EPROM and flash EEPROM with NAND structure cell. In *1987 International Electron Devices Meeting, IEDM. Technical Digest (Cat. No.87CH2515-5), Washington, DC, USA, 06/12/1987-09/12/1987*, pages 552–5. Toshiba Corp, Kawasaki, Japan, New York, NY, USA: IEEE, 1987.
- [5] L. Baldi and R. Bez. The scaling challenges of CMOS and the impact on high-density non-volatile memories. *Microsystem Technologies, Germany*, 13(2):133–8, 2007.
- [6] G. Snider, P. Kuekes, T. Hogg, and R. Stanley Williams. Nanoelectronic architectures. *Applied Physics A: Materials Science & Processing*, A80(6):1183–95, 2005.
- [7] R. Mueller, S. De Jonge, K. Myny, D. J. Wouters, J. Genoe, and P. Heremans. Organic CuTCNQ integrated in complementary metal oxide semiconductor. *Applied Physics Letters*, 89:223501, 2006.
- [8] J. F. Scott and C. A. Paz de Araujo. Ferroelectric memories. *Science, USA*, 246(4936):1400–5, 1989.
- [9] J. L. Moll and Y. Tarui. A new solid state memory resistor. *IEEE Trans. Electron. Devices*, 10(5):338, 1963.
- [10] L. J. Schwee, P. E. Hunter, K. A. Restorff, and M. T. Shephard. The concept and initial studies of a crosstie random access memory (CRAM). *Journal of Applied Physics*, 53(3):2762–2764, 1982.
- [11] S. Tiwari, F. Rana, H. Hanafi, A. Hartstein, E. F. Crabbe, and K. Chan. A silicon nanocrystals based memory. *Applied Physics Letters, USA*, 68(10):1377–9, 1996.
- [12] S. Lai and T. Lowrey. OUM - A 180 nm nonvolatile memory cell element technology for stand alone and embedded applications. In *International Electron Devices Meeting. Technical Digest, Washington, DC, USA, 02/12/2001-05/12/2001*, pages 36.5.1–4. Intel Corp, Santa Clara, CA, USA, Piscataway, NJ, USA: IEEE, 2001.

- [13] M. N. Kozicki, C. Gopalan, M. Balakrishnan, M. Park, and M. Mitkova. Non-volatile memory based on solid electrolytes. In *Proceedings. 2004 Non-Volatile Memory Technology Symposium, Orlando, FL, USA, 15/11/2004-17/11/2004*, pages 10–17. Center for Solid State Electron Res, Arizona State Univ, Tempe, AZ, USA, Piscataway, NJ, USA: IEEE, 2004.
- [14] R. S. Potember, T. O. Poehler, and D. O. Cowan. Electrical switching and memory phenomena in Cu-TCNQ thin films. *Applied Physics Letters, USA*, 34(6):405–7, 1979.
- [15] R. H. Dennard. Field-Effect Transistor Memory. *U.S. Patent*, (3387286), 1968.
- [16] K. E. Drangeid, R. F. Broom, w. g. Jutzi, T. O. Mohr, a. Moser, and G. Sasso. A memory-cell array with normally off-type Schottky-Barrier FET's. *IEEE Journal of Solid-State Circuits, USA*, SC-7(4):277–82, 1972.
- [17] S. Okhonin, M. Nagoga, J. M. Sallese, and P. Fazan. A capacitor-less 1T-DRAM cell. *IEEE Electron Device Letters, USA*, 23(2):85–7, 2002.
- [18] R. A. Haken, W. E. Feger, D. J. Coleman, and C. S. Wang. A SONOS/CMOS non-volatile RAM. In *Proceedings IEEE International Conference on Computer Design: VLSI in Computers (ICCD '83), Port Chester, NY, USA, 31/10/1983-03/11/1983*, pages 93–6. Texas Instruments Inc, Dallas, TX, USA, Silver Spring, MD, USA: IEEE Comput. Soc. Press, 1983.
- [19] B. Govoreanu, P. Blomme, M. Rosmeulen, J. Van-Houdt, and K. De-Meyer. VAR-IOT: a novel multilayer tunnel barrier concept for low-voltage nonvolatile memory devices. *IEEE Electron Device Letters, USA*, 24(2):99–101, 2003.
- [20] J. G. Simmons and R. R. Verderber. New thin-film resistive memory. *Radio and Electronic Engineer, UK*, 34:81–89, 1967.
- [21] A. Szymanski, D. C. Larson, and M. M. Labes. A temperature-independent conducting state in tetracene thin film. *Applied Physics Letters, USA*, 14(3):88–90, 1969.
- [22] J. Chen, M. A. Reed, A. M. Rawlett, and J. M. Tour. Large On-Off Ratios and Negative Differential Resistance in a Molecular Electronic Device. *Science*, 286:1550–1552, 1999.
- [23] Semiconductor Industry Association. International Technology Roadmap for Semiconductors 2007 Edition, 2007.
- [24] Jian-Gang-Zhu and J. Daughton. A novel low switching current MRAM design. In *Intermag Europe 2002 Digest of Technical Papers. 2002 IEEE International Magnetism Conference, Amsterdam, Netherlands, 28/04/2002-02/05/2002*, page BB1. DSSC, Carnegie Mellon Univ, Pittsburgh, PA, USA, Piscataway, NJ, USA: IEEE, 2002.
- [25] J. G. Deak. Spin injection in thermally assisted magnetic random access memory. *Journal of Applied Physics, USA*, 97(10):10E316–1–3, 2005.
- [26] G. Atwood and R. Bez. Current status of chalcogenide phase change memory. In *Device Research Conference, Santa Barbara, CA, USA, 20/06/2005-22/06/2005*, pages 1–5. Intel Corp, Santa Clara, CA, USA, Piscataway, NJ, USA: IEEE, 2005.

- [27] N. Yamada, E. Ohno, K. Nishiuchi, N. Akahira, and M. Takao. Rapid-phase transitions of GeTe-Sb₂Te₃ pseudobinary amorphous thin films for an optical disk memory. *Journal of Applied Physics, USA*, 69(5):2849–56, 1991.
- [28] T. W. Hickmott. Low-frequency negative resistance in thin anodic oxide films. *Journal of Applied Physics, USA*, 33:2669–2682, 1962.
- [29] H. Pagnia and N. Sotnik. Bistable switching in electroformed metal-insulator-metal devices. *Physica Status Solidi A, East Germany*, 108(1):11–65, 1988.
- [30] A. Asamitsu, Y. Tomioka, H. Kuwahara, and Y. Tokura. Current switching of resistive states in magnetoresistive manganites. *Nature*, 388(6637):50–2, 1997.
- [31] M. N. Kozicki, M. Yun, L. Hilt, and A. Singh. Applications of programmable resistance changes in metal-doped chalcogenides. In *Proceedings of Solid-State Ionic Devices, Seattle, WA, USA, 02/05/1999-07/05/1999*, pages 298–309. Center for Solid State Electron Res, Arizona State Univ, Tempe, AZ, USA, Pennington, NJ, USA: Electrochem. Soc, 1999.
- [32] A. Beck, J. G. Bednorz, C. Gerber, C. Rossel, and D. Widmer. Reproducible switching effect in thin oxide films for memory applications. *Applied Physics Letters, USA*, 77(1):139–41, 2000.
- [33] R. Waser and M. Aono. Nanoionics-based resistive switching memories. *Nature Materials*, 6:833–840, 2007.
- [34] F. A. Chudnovskii, L. L. Odyets, A. L. Pergament, and G. B. Stefanovich. Electroforming and switching in oxides of transition metals: the role of metal-insulator transition in the switching mechanism. *Journal of Solid State Chemistry, USA*, 122(1):95–9, 1996.
- [35] I. G. Baek, M. S. Lee, S. O. Park, H. S. Kim, U-In Chung, S. Seo, M. J. Lee, D. H. Seo, D. S. Suh, J. C. Park, I. K. Yoo, and J. T. Moon. Highly Scalable Non-volatile Resistive Memory using Simple Binary Oxide Driven by Asymmetric Unipolar Voltage Pulses. *IEDM Tech. Dig.*, pages 587 – 590, 2004.
- [36] J.G. Simmons and R.R. Verderber. New conduction and reversible memory phenomena in thin insulating films. *Proc. Roy. Soc. A*, 301:77–102, 1967.
- [37] A. Sawa, T. Fujii, M. Kawasaki, and Y. Tokura. Interface resistance switching at a few nanometer thick perovskite manganite active layers. *Applied Physics Letters, USA*, 88(23):232112–1–3, 2006.
- [38] G. I. Meijer, U. Staub, M. Janousch, S. L. Johnson, B. Delley, and T. Neisius. Valence states of Cr and the insulator-to-metal transition in Cr-doped SrTiO₃. *Phys. Rev. B*, 72:155102, 2005.
- [39] M. J. Rozenberg, I. H. Inoue, and M. J. Sanchez. Nonvolatile memory with multi-level switching: a basic model. *Physical Review Letters, USA*, 92(17):178302/1–4, 2004.
- [40] M. J. Rozenberg, I. H. Inoue, and M. J. Sanchez. Strong electron correlation effects in nonvolatile electronic memory devices. *Applied Physics Letters, USA*, 88(3):33510–1–3, 2006.

- [41] J. Maier. Nanoionics: ion transport and electrochemical storage in confined systems. *Nature Materials*, 4, 2005.
- [42] K. Terabe, T. Hasegawa, T. Nakayama, and M. Aono. Quantized conductance atomic switch. *Nature*, 433(6):47–50, 2005.
- [43] T. Baiatu, R. Waser, and K. H. Hardtl. DC electrical degradation of perovskite-type titanates. III. A model of the mechanism. *Journal of the American Ceramic Society, USA*, 73(6):1663–73, 1990.
- [44] J. C. Scott and L. D. Bozano. Nonvolatile Memory Elements Based on Organic Materials. *Advanced Materials*, 19(11):1452, 2007.
- [45] L. V. Gregor. Polymer dielectric films. *IBM Journal of Research and Development*, 12(2):140–62, 1968.
- [46] L. F. Pender and R. J. Fleming. Memory switching in glow discharge polymerized thin films. *Journal of Applied Physics, USA*, 46(8):3426–31, 1975.
- [47] H. K. Henisch and W. R. Smith. Switching in organic polymer films. *Applied Physics Letters*, 24(12):589–91, 1974.
- [48] H. S. Majumdar, A. Bandyopadhyay, A. Bolognesi, and A. J. Pal. Memory device applications of a conjugated polymer: Role of space charges. *Journal of Applied Physics*, 91(4):2433–7, 2002.
- [49] A. R. Elsharkawi and K. C. Kao. Switching and memory phenomena in anthracene thin films. *Journal of the Physics and Chemistry of Solids, UK*, 38(1):95–6, 1977.
- [50] D. Tondelier, K. Lmimouni, D. Vuillaume, C. Fery, and G. Haas. Metal/organic/metal bistable memory devices. *Applied Physics Letters, USA*, 85(23):5763–5, 2004.
- [51] A. K. Mahapatro, R. Agrawal, and S. Ghosh. Electric-field-induced conductance transition in 8-hydroxyquinoline aluminum (Alq3). *Journal of Applied Physics*, 96(6):3583–5, 2004.
- [52] A. Bandyopadhyay and A. J. Pal. Large conductance switching and memory effects in organic molecules for data-storage applications. *Applied Physics Letters, USA*, 82(8):1215–17, 2003.
- [53] C. P. Collier, G. Mattersteig, E. W. Wong, Yi-Luo, K. Berverly, J. Sampaio, F. M. Raymo, J. F. Stoddart, and J. R. Heath. A [2]catenane-based solid state electronically reconfigurable switch. *Science, USA*, 289(5482):1172–5, 2000.
- [54] M. Ouyang, S. M. Hou, H. F. Chen, K. Z. Wang, and Z. Q. Xue. A new organic-organic complex thin film with reproducible electrical bistability properties. *Physics Letters A*, 235(4):413–17, 1997.
- [55] Qianxi Lai, Zuhua Zhu, Yong Chen, S. Patil, and F. Wudl. Organic nonvolatile memory by dopant-configurable polymer. *Applied Physics Letters*, 88(13):133515–1–3, 2006.

- [56] Jianyong-Ouyang, Chih-Wei-Chu, C. R. Szmanda, Liping-Ma, and Yang-Yang. Programmable polymer thin film and non-volatile memory device. *Nature Materials, UK*, 3(12):918–22, 2004.
- [57] S. H. Kang, T. Crisp, I. Kymissis, and V. Bulovic. Memory effect from charge trapping in layered organic structures. *Applied Physics Letters*, 85(20):4666, 2004.
- [58] Jiangshan Chen and Dongge Ma. Performance improvement by charge trapping of doping fluorescent dyes in organic memory devices. *Journal of Applied Physics*, 100(3):34512–1–4, 2006.
- [59] E. I. Kamitsos, C. H. Tzimis, and W. M. Risen. Raman study of the mechanism of electrical switching in Cu TCNQ films. *Solid State Communications*, 42(8):561–5, 1982.
- [60] M. Lauters, B. McCarthy, D. Sarid, and G. E. Jabbour. Multilevel conductance switching in polymer films. *Applied Physics Letters, USA*, 89(1):13507–1–3, 2006.
- [61] L. D. Bozano, B. W. Kean, V. R. Deline, J. R. Salem, and J. C. Scott. Mechanism for bistability in organic memory elements. *Applied Physics Letters, USA*, 84(4):607–9, 2004.
- [62] Z. K. Keane, J. W. Ciszek, J. M. Tour, and D. Natelson. Three-Terminal Devices to Examine Single-Molecule Conductance Switching. *Nano Lett.*, 6:1518–1521, 2006.
- [63] Z. Li, I. Pobelov, B. Han, T. Wandlowski, A. Blaszczyk, and M. Mayor. Conductance of redox-active single molecular junctions: an electrochemical approach. *Nanotechnology, UK*, 18(4):1–8, 2007.
- [64] S. Karthaus, B. Lussem, M. Weides, M. Alba, A. Besmehn, R. Oligschlaeger, and R. Waser. Resistive switching of rose bengal devices: a molecular effect? *Journal of Applied Physics, USA*, 100(9):94504–1–6, 2006.
- [65] M. Colle, M. Buchel, and D. M. de Leeuw. Switching and filamentary conduction in non-volatile organic memories. *Organic Electronics, UK*, 7(5):305–12, 2006.
- [66] Jason J. Blackstock, William F. Stickle, Carrie L. Donley, Duncan R. Stewart, and R. Stanley Williams. Internal Structure of a Molecular Junction Device: Chemical Reduction of PtO₂ by Ti. *Journal of Physical Chemistry C*, 111:16–20, 2007.
- [67] M. Schwoerer and H. C. Wolf. *Organische Molekulare Festkoerper*. Wiley - VCH, 2005.
- [68] R. J. Warmack, T. A. Callcott, and H. C. Schweinler. Calculations of apparent conductivity for an anisotropic medium (TTF) (TCNQ). *Applied Physics Letters*, 24(12):635–7, 1974.
- [69] T. Linker and M. Schmittel. *Radikale und Radikationen in der Organischen Chemie*. Wiley - VCH, 1998.
- [70] L. R. Melby, R. J. Harder, W. R. Hertler, W. Mahler, R. E. Benson, and W. E. Mochel. Substituted Quinodimethans. II. Anion-radical Derivatives and Complexes of 7,7,8,8-Tetracyanoquinodimethan. *Journal of American Chemical Society*, 84:3374, 1962.

- [71] R. E. Long, R. A. Sparks, and K. N. Trueblood. The Crystal and Molecular Structure of 7,7,8,8-Tetraeyanoquinodimethane. *Acta Crystallographica*, 18:935, 1965.
- [72] T. L. Cairns, R. A. Carboni, D. D. Coffman, V. A. Engelhardt, R. E. Heckert, E. L. Little, E. G. McGeer, B.C. McKusick, W. J. Middleton, R. M. Scribner, C. W. Theobald, and H. E. Winberg. Cyanocarbon Chemistry. I. Preparation and Reactions of Tetracyanoethylene. *Journal of the American Chemical Society*, 80(11):2775–2778, 1958.
- [73] D. S. Acker and W. R. Hertler. Preparation and Chemistry of 7,7,8,8-Tetracyanoquinodimethane. *Journal of the American Chemical Society*, 84(17):3370–3374, 1962.
- [74] R. A. Heintz, H. Zhao, X. Ouyang, G. Grandinetti, J. Cowen, and K. R. Dunbar. New Insight into the Nature of Cu(TCNQ): Solution Routes to Two Distinct Polymorphs. *Inorg. Chem.*, 38(1):144–156, 1999.
- [75] R. Muller, De Jonge S, K. Myny, D. J. Wouters, J. Genoe, and P. Heremans. Organic CuTCNQ non-volatile memories for integration in the CMOS backend-of-line: Preparation from gas/solid reaction and downscaling to an area of 0.25μm². *Solid-State Electronics*, 50(4):601–5, 2006.
- [76] M. Hanack and G. Pawlowski. Organic conductors. *Die Naturwissenschaften*, 69(6):266–75, 1982.
- [77] R. Kato. Conductive Copper Salts of 2,5-Disubstituted N,N'-Dicyanobenzoquinonediimines (DCNQIs): Structural and Physical Properties. *Bulletin of the Chemical Society of Japan*, 73(3):515–534, 2000.
- [78] Liu-Shenggao, Liu-Yunqi, Wu-Peiji, Zhu-Daoben, Tian-He, and Chen-Kongchang. Characterisation and electrical property of molten-grown CuTCNQ film material. *Thin Solid Films, Switzerland*, 289(1-2):300–5, 1996.
- [79] Sun-Shuqing, Wu-Peiji, and Zhu-Daoben. The preparation, characterization of amorphous Cu-TCNQ film with a low degree of charge-transfer (DCT) and its electric switching properties. *Thin Solid Films, Switzerland*, 301(1-2):192–6, 1997.
- [80] C. Sato, S. Wakamatsu, K. Tadokoro, and K. Ishii. Polarized memory effect in the device including the organic charge-transfer complex, copper-tetracyanoquinodimethane. *Journal of Applied Physics, USA*, 68(12):6535–7, 1990.
- [81] T. Oyamada, H. Tanaka, K. Matsushige, H. Sasabe, and C. Adachi. Switching effect in Cu:TCNQ charge transfer-complex thin films by vacuum codeposition. *Applied Physics Letters, USA*, 83(6):1252–4, 2003.
- [82] K. Xiao, I.Â N. Ivanov, A.Â A. Poretzky, Z. Liu, and D.Â B. Geohegan. Directed Integration of Tetracyanoquinodimethane-Cu Organic Nanowires into Prefabricated Device Architectures. *Adv. Mater.*, 18(16):2184, 2006.
- [83] R. S. Potember, T. O. Poehler, and R. C. Benson. Optical switching in semiconductor organic thin films. *Applied Physics Letters, USA*, 41(6):548–50, 1982.

- [84] M. Matsumoto, Y. Nishio, H. Tachibana, T. Nakamura, Y. Kawabata, H. Samura, and T. Nagamura. Switching and Memory Phenomena of CuTCNQ Thin Films Triggered by a Stimulus with an STM Tip. *Chemistry Letters*, 20(6):1021, 1991.
- [85] J. B. Torrance, J. E. Vazquez, J. J. Mayerle, and V. Y. Lee. Discovery of a neutral-to-ionic phase transition in organic materials. *Physical Review Letters*, 46(4):253–7, 1981.
- [86] J. B. Torrance, A. Girlando, J. J. Mayerle, J. I. Crowley, V. Y. Lee, P. Batail, and S. J. LaPlaca. Anomalous nature of neutral-to-ionic phase transition in tetrathiafulvalene-chloranil. *Physical Review Letters*, 47(24):1747–50, 1981.
- [87] R. Collet, M. H. Lemee-Cailleau, Buron-Le Cointe M, H. Cailleau, M. Wulff, T. Luty, S. Y. Koshihara, M. Meyer, L. Toupet, P. Rabiller, and S. Techert. Laser-induced ferroelectric structural order in an organic charge-transfer crystal. *Science*, 300(5619):612–15, 2003.
- [88] S. Koshihara, Y. Takahashi, H. Sakai, Y. Tokura, and T. Luty. Photoinduced cooperative charge transfer in low-dimensional organic crystals. *Journal of Physical Chemistry B*, 103(14):2592–600, 1999.
- [89] Zhongze Gu, Haiming Wu, Yu Wie, and Juzheng Liu. Mechanism generating switching effects in copper-TCNQ and silver-TCNQ films. *J. Phys. Chem.*, 97(11):2543–2545, 1993.
- [90] T. Sakamoto, H. Sunamura, H. Kawaura, T. Hasegawa, T. Nakayama, and M. Aono. Nanometer-scale switches using copper sulfide. *Applied Physics Letters*, 82(18):3032–4, 2003.
- [91] Y. Iwasa, T. Koda, Y. Tokura, S. Koshihara, N. Iwasawa, and G. Saito. Switching effect in organic charge transfer complex crystals. *Applied Physics Letters*, 55(20):2111–13, 1989.
- [92] Y. Iwasa, T. Koda, S. Koshihara, Y. Tokura, N. Iwasawa, and G. Saito. Intrinsic negative-resistance effect in mixed-stack charge-transfer crystals. *Physical Review B (Condensed Matter)*, 39(14):10441–4, 1989.
- [93] J. J. Hoagland, X. D. Wang, and K. W. Hipps. Characterization of Cu-Cu-TCNQ-M Devices Using Scanning Electron Microscopy and Scanning Tunneling Microscopy. *Chemical Materials*, 5(1):54–60, 1993.
- [94] K. Jousten and M. Wutz. *Wutz Handbuch Vakuumtechnik*. Vieweg Verlag, Wiesbaden, 2006.
- [95] S. Schiller and U. Heisig. *Bedampfungstechnik - Verfahren, Einrichtungen, Anwendungen*. VEB Verlag Technik, Berlin, 1975.
- [96] J.M. Lafferty (ed). *Foundations of Vacuum Science and Technology*. John Wiley and Sons Inc., New York, 1998.
- [97] T. G. Beckwith, R. D. Marangoni, and J. H. Lienhard. *Measurement of Low Pressures*. Addison-Wesley, Reading, MA, 1993.

- [98] T. Kever, C. Nauenheim, U. Bottger, and R. Waser. Preparation and characterisation of amorphous Cu:7,7,8,8-Tetracyanoquinodimethane thin films with low surface roughness via thermal co-deposition. *Thin Solid Films, Switzerland*, 515(4):1893–6, 2006.
- [99] Y. Iida. Electronic Spectra of Crystalline TCNQ Anion Radical Salts. *Bulletin of the Chemical Society of Japan*, 42(1):71–75, 1969.
- [100] R. C. Hoffman and R. S. Potember. Organometallic materials for erasable optical storage. *Applied Optics, USA*, 28(7):1417–21, 1989.
- [101] D. A. Lowitz. Pople-like SCF-LCAO-MO treatment of 77', 88'-tetracyanoquinodimethan and its univalent anion. *Journal of Chemical Physics*, 46(12):4698–4717, 1967.
- [102] R. Bozio, I. Zanon, A. Girlando, and C. Pecile. Influence of the intermolecular charge transfer interaction on the solution and solid state infrared spectra of 7, 7, 8, 8-tetracyanoquinodimethane (TCNQ) alkaline salts. *Journal of the Chemical Society Faraday Transactions II, UK*, 74:235–48, 1978.
- [103] Liu Sheng-Gao, Liu Yun-Qi, and Zhu Dao-Ben. Amorphous semiconducting film containing nanometer particles of CuTCNQ: preparation, characterization and electrical switching property. *Thin Solid Films*, 280(1-2):271–7, 1996.
- [104] J. S. Chapell, A. N. Bloch, W. A. Bryden, M. Maxfield, T. O. Poehler, and D. O. Cowan. Degree of Charge Transfer in Organic Conductors by Infrared Absorption Spectroscopy. *Journal of American Chemical Society*, 103:2442, 1981.
- [105] S. M. Sze and Kwok K. Ng. *Physics Of Semiconductor Devices*. Wiley, 2007.
- [106] K. Gloos, P. J. Koppinen, and J. P. Pekola. Properties of Native Ultrathin Aluminium Oxide Tunnel Barriers. *Journal of Physics: Condensed Matter*, 15:1733–1746, 2003.
- [107] T. Kever, B. Klopstra, U. Boettger, and R. Waser. On the Existence of Two Different Resistive Switching Mechanisms in Metal Organic Charge Transfer Complex Thin Films. *IEEE NVMTS Proceedings 2006*, pages 116–119, 2006.
- [108] R. Sezi, A. Walter, R. Engl, A. Maltenberger, J. Schumann, M. Kund, and C. Dehm. Organic materials for high-density non-volatile memory applications. In *IEEE International Electron Devices Meeting 2003, Washington, DC, USA, 08/12/2003-10/12/2003*, pages 10.2.1–4. Infineon Technol AG, Erlangen, Germany, Pisacataway, NJ, USA: IEEE, 2003.
- [109] R. Muller, R. Naulaerts, J. Billen, J. Genoe, and P. Heremans. CuTCNQ resistive nonvolatile memories with a noble metal bottom electrode. *Applied Physics Letters, USA*, 90(6):63503/1–3, 2007.
- [110] H. Clausert and G. Wiesemann. *Grundgebiete der Elektrotechnik 1*. Oldenbourg Wissenschaftsverlag Muenchen, 1999.
- [111] S. Kaeriyama, T. Sakamoto, H. Sunamura, M. Mizuno, H. Kawaura, T. Hasegawa, K. Terabe, T. Nakayama, and M. Aono. A nonvolatile programmable solid-electrolyte nanometer switch. *IEEE Journal of Solid-State Circuits, USA*, 40(1):168–76, 2005.

- [112] M. N. Kozicki, C. Gopalan, M. Balakrishnan, and M. Mitkova. A low-power nonvolatile switching element based on copper-tungsten oxide solid electrolyte. *IEEE Transactions on Nanotechnology, USA*, 5(5):535–44, 2006.
- [113] S. Dietrich, M. Angerbauer, M. Ivanov, D. Gogl, H. Hoenigschmid, M. Kund, C. Liaw, M. Markert, R. Symanczyk, L. Altimime, S. Bournat, and G. Mueller. A nonvolatile 2-Mbit CBRAM memory core featuring advanced read and program control. *IEEE Journal of Solid-State Circuits, USA*, 42(4):839–45, 2007.
- [114] T. Kever, U. Boettger, C. Schindler, and R. Waser. On the origin of bistable resistive switching in metal organic charge transfer complex memory cells. *Applied Physics Letters, USA*, 91(8):083506/1–3, 2007.
- [115] J. Billen, S. Streudel, R. Mueller, J. Genoe, and P. Heremans. A comprehensive model for bipolar electrical switching of CuTCNQ memories. *Applied Physics Letters*, 91(263507), 2007.

Lebenslauf

Persönliche Daten

Name: Thorsten Kever
Geburtsdatum: 13.07.1977
Geburtsort: Erkelenz

Berufliche Tätigkeit

Seit 07/2008: Ingenieur im Bereich Sensorentwicklung,
Robert Bosch GmbH, Reutlingen
06/2003 - 06/2008: Wissenschaftlicher Mitarbeiter am Institut
für Werkstoffe der Elektrotechnik der RWTH Aachen

Studium

10/1997 - 04/2003: Studium der Elektrotechnik an der RWTH Aachen

Wehrdienst

07/1996 - 05/1997: Jagdbombergeschwader 31, Nörvenich

Schulbildung

08/1987 - 06/1996: Maximilian Kolbe Gymnasium Wegberg
08/1983 - 06/1987: Gemeinschaftgrundschule Wildenrath